

Deep Dynamic Stall

Investigating Pressure and PIV for Understanding
Deep Dynamic Stall Phenomena

Aerodynamics Master Thesis

Pepijn Slooter

Deep Dynamic Stall

Investigating Pressure and PIV for
Understanding Deep Dynamic Stall Phenomena

by

Pepijn Slooter

to obtain the degree of Master of Science
at the Delft University of Technology,
to be defended publicly on Thursday July 25, 2024 at 10:00 AM.

Student number: 4540581
Project duration: September 27, 2023 – July 25, 2024
Thesis committee: Prof. dr. ir. C.J. Simão Ferreira, TU Delft, Supervisor
Dr. D. Ragni, TU Delft, Chair
Dr. M. Li, TU Delft, Examiner
G. Xu TU Delft, Secondary Supervisor

Cover: AI-Generated
Style: TU Delft Report Style

An electronic version of this thesis is available at <http://repository.tudelft.nl/>.

Acknowledgements

I would like to express my sincere gratitude to Carlos Simão Ferreira and Guanqun Xu for their unwavering support, dedicated weekly supervision, and collaborative efforts on numerous projects. Their guidance and insightful input have greatly contributed to the progress and success of my work. Their enthusiastic support and invaluable feedback, generously shared every other week, have been instrumental in shaping the quality of my research. I am also deeply appreciative of Wei Yu, whose involvement in my thesis has been marked by her continuous support and the fresh perspectives she has provided during the initial phase and testing. Her insights have added a valuable layer to my work, and I am grateful for her contributions to the development of my research. Finally, I express my gratitude to Stefan Bernardy and Abhratej Sahoo for their consistent support throughout the testing campaign in the LTT. Without their assistance, the test results would not have been as favourable. I also appreciate the contributions of Andrea Sciacchitano, Martijn Looman and Emiel Langedijk.

Beyond my academic mentors, I owe a debt of gratitude to my friends and family, whose unwavering support has been a cornerstone throughout this academic journey. A special acknowledgement goes to my parents, sister, and partner, whose consistent assistance, attentive ears and unending support during every step of my academic career have been a source of strength from the outset of my studies. Without their support, I would not have reached the point I am at today.

*Pepijn Slooter
Delft, July 2024*

Abstract

Wind turbines play a crucial role in the worldwide effort to embrace sustainable energy, utilizing sophisticated aerodynamic principles to efficiently capture wind energy. A thorough comprehension of deep dynamic stall, a phenomenon that greatly impacts wind turbine performance, is essential for maximizing efficiency, maintaining structural integrity, and propelling the development of wind energy. This study presents an experimental exploration of deep dynamic stall phenomena through wind tunnel experiments carried out on a NACA643418 airfoil at TU Delft.

The study commences with the development of a comprehensive test matrix drawing from existing literature, with a focus on angles of attack of 40° , 50° , and 90° (degrees). Through precise experimentation, the research team meticulously measures and corrects for wind tunnel effects, uncovering crucial trends in lift and drag coefficients (C_l and C_d respectively). Significantly, the study identifies laminar separation bubbles and trailing edge separation as the main stall mode before the deep stall regime.

The analysis of static and dynamic pressure data offers valuable insights into the aerodynamic characteristics of the airfoil in deep stall conditions. Notably, significant variations in aerodynamic performance between the upstroke and downstroke are evident, particularly at high angles of attack surpassing 25° . For 40° and 50° angles, increased frequency and amplitude reduce the dominance of the shedding frequency, while it remains significant at 90° . Hysteresis plots show higher drag and lift coefficients during the downstroke, with these differences growing with increased frequency and amplitude. At a 90° angle, the coefficients exhibit linear behaviour, driven mainly by the shedding frequency rather than pitching motion.

The phase-averaged PIV images serve as a valuable complement to the pressure data, offering a visual confirmation of how flow dynamics impact aerodynamic performance in deep stall conditions. They show less reverse flow during the downstroke for 40° and 50° cases, which correlated with lower lift performance during the upstroke. The study concludes that deep stall conditions, characterized by angles of attack exceeding 25° , lead to significant airflow disruption, resulting in increased drag and a parabolic lift coefficient curve. The pitching frequency and amplitude significantly affect aerodynamic performance, particularly at high angles of attack, where vortex shedding becomes a dominant factor.

List of Figures

2.1	Airfoil illustration with important parameters indicated as from Anderson (2017).	5
2.2	Lift polar showing how the lift coefficient varies with the angle of attack for a cambered airfoil by Anderson (2017).	6
2.3	Investigating the performance of two DU airfoils across the entire 360° range of angles-of-attack by W. Timmer and Rooij (2001).	6
2.4	A visual representation showing the sequential stages of flow evolution within a dynamic stall hysteresis loop observed on a 2D oscillating airfoil from J. Gordon Leishman (2006).	8
2.5	Demonstration of replacing the finite wing with a bound vortex and a trailing free vortex by Anderson (2017).	10
2.6	Illustration of the elementary distribution within the DW model during separated flow by Zanon, Giannattasio, and C. J. Simão Ferreira (2013).	11
2.7	Configuration of the 2D 2 component PIV experimental setup, illustrating the tracer particles illuminated by the first light pulse at time t (depicted in black) and the subsequent light pulse at $t + \Delta t$ (depicted in red). Markus Raffel et al. (2007)	21
3.1	Visualization of the NACA643418 airfoil at a 0° angle of attack, highlighting the locations of pressure taps.	27
3.2	NACA643418 airfoil within the wind tunnel, depicted at a 50° angle of attack.	27
3.3	Comparison between connection tubes for pressure taps (a) and connectors for attaching pressure tubes to the pressure reading machine (b). Images provided by S. Bernardy.	28
3.4	Comparison between the schematic diagram (a) and the actual setup (b) of the actuator system. The schematic diagram illustrates the theoretical arrangement and components involved, while the photograph depicts the physical implementation of the system. Provided by S. Bernardy.	30
3.5	CAD image of the wind tunnel configuration featuring the NACA643418 airfoil at a 0° angle of attack, showcasing the blue-coloured test section. The PIV setup is shown alongside the test section with the Evergreen lasers, and sCMOS cameras positioned underneath the test section.	31
3.6	Schematic plot of the PIV measurement setup. The components of the measurement are: ①: incoming wind ②: test section ③: laser ④:illumination plane ⑤: airfoil model ⑥: camera ⑦: camera view.	32
3.7	Figures showing the upper and lower side of an airfoil with a calibration plate.	33
4.1	Comparison study of C_l values for different Reynolds numbers.	36
4.2	Comparison study of C_d values for different Reynolds numbers.	37
4.3	Single-sided FFT amplitude spectrum and real angle data for both the measured signal and a perfect sinusoidal signal at $\alpha_{\text{mean}} = 10^\circ$, $f_{\text{pitching}} = 1\text{Hz}$, and $A_{\text{pitching}} = 5^\circ$	38
4.4	Single-sided FFT amplitude spectrum and real angle data for both the measured signal and a perfect sinusoidal signal at $\alpha_{\text{mean}} = 40^\circ$, $f_{\text{pitching}} = 2\text{Hz}$, and $A_{\text{pitching}} = 5^\circ$	38
4.5	Single-sided FFT amplitude spectrum and real angle data for both the measured signal and a perfect sinusoidal signal at $\alpha_{\text{mean}} = 10^\circ$, $f_{\text{pitching}} = 3\text{Hz}$, and $A_{\text{pitching}} = 10^\circ$	39
4.6	Single-sided FFT amplitude spectrum and real angle data for both the measured signal and a perfect sinusoidal signal at $\alpha_{\text{mean}} = 40^\circ$, $f_{\text{pitching}} = 4\text{Hz}$, and $A_{\text{pitching}} = 5^\circ$	39
4.7	Comparison of uncorrected and corrected C_d values using combined Allen (0° to 20°) and Maskell (21° to 180°) wind tunnel corrections at different Reynolds numbers.	41
4.8	Comparison of corrected C_d values using combined Allen (0° to 20°) and Maskell (21° to 180°) wind tunnel corrections for different Reynolds numbers.	42
4.9	Comparison of uncorrected and corrected C_l values using combined Allen (0° to 20°) and Maskell (21° to 180°) wind tunnel corrections at different wind speeds.	43

4.10 Comparison of corrected C_l values using combined Allen (0 to 20°) and Maskell (21 to 180°) wind tunnel corrections for different Reynolds numbers.	44
4.11 Comparison of uncorrected and corrected C_p values using Maskell wind tunnel corrections for different deep stall angles of attack at $Re = 250k$	45
4.12 Comparison of uncorrected and corrected C_p values using Maskell wind tunnel corrections for different angles of attack at $Re = 250k$, showcasing the stall mode in static airfoil conditions.	46
4.13 Static averaged flow fields (U/U_∞) at various α for $Re = 250k$ with the black lines showing the average flow field function.	48
4.14 Instantaneous flow fields in a time series with vector arrows that display the relative magnitude and direction of the flow in both x- and y-direction and one standard deviation plot at $\alpha = 40^\circ$ and $Re = 250k$	50
4.15 Instantaneous flow fields in a time series with vector arrows that display the relative magnitude and direction of the flow in both x- and y-direction and one standard deviation plot at $\alpha = 50^\circ$ and $Re = 250k$	51
4.16 Instantaneous flow fields in a time series with vector arrows that display the relative magnitude and direction of the flow in both x- and y-direction and one standard deviation plot at $\alpha = 90^\circ$ and $Re = 250k$	52
4.17 Instantaneous vorticity field (ω/U_∞) with vector arrows that display the relative magnitude and direction of the flow in both x- and y-direction at $\alpha = 40^\circ$ and $Re = 250k$	53
4.18 Instantaneous vorticity field (ω/U_∞) with vector arrows that display the relative magnitude and direction of the flow in both x- and y-direction at $\alpha = 50^\circ$ and $Re = 250k$	54
4.19 Instantaneous vorticity field (ω/U_∞) with vector arrows that display the relative magnitude and direction of the flow in both x- and y-direction at $\alpha = 90^\circ$ and $Re = 250k$	55
4.20 Comparison of C_l and C_d for different amount of data acquisition cycles.	56
4.21 Comparison of the percentage variability of C_l and C_d for different amount of data acquisition cycles.	57
4.22 Amplitude factor response dynamic pressure for the upper and lower side of the airfoil.	58
4.23 Phase response dynamic pressure for the upper and lower side of the airfoil.	58
4.24 Single-sided amplitude plot for the original signal and the dynamic response corrected signal for $\alpha_{mean} = 40^\circ$ at $f_{pitching} = 2\text{Hz}$	59
4.25 Single-sided amplitude plot for the original signal and the dynamic response corrected signal for $\alpha_{mean} = 40^\circ$ at $f_{pitching} = 3\text{Hz}$	60
4.26 Single-sided amplitude plot for the original signal and the dynamic response corrected signal for $\alpha_{mean} = 50^\circ$ at $f_{pitching} = 2\text{Hz}$	60
4.27 Single-sided amplitude plot for the original signal and the dynamic response corrected signal for $\alpha_{mean} = 50^\circ$ at $f_{pitching} = 3\text{Hz}$	61
4.28 Single-sided amplitude plot for the original signal and the dynamic response corrected signal for $\alpha_{mean} = 90^\circ$ at $f_{pitching} = 2\text{Hz}$	62
4.29 Single-sided amplitude plot for the original signal and the dynamic response corrected signal for $\alpha_{mean} = 90^\circ$ at $f_{pitching} = 3\text{Hz}$	62
4.30 Comparison of $C_{d_{pressure}}$ for unsteady cases at $\alpha_{mean} = 40^\circ$ and $Re = 250k$. The black line represents the mean value, with the solid line representing the upstroke motion, the dashed line representing the downstroke motion and the blue line the values of static measurements.	63
4.31 Comparison of $C_{d_{pressure}}$ for unsteady cases at $\alpha_{mean} = 50^\circ$ and $Re = 250k$. The black line represents the mean value, with the solid line representing the upstroke motion, the dashed line representing the downstroke motion and the blue line the values of static measurements.	65
4.32 Comparison of $C_{d_{pressure}}$ for unsteady cases at $\alpha_{mean} = 90^\circ$ and $Re = 250k$. The black line represents the mean value, with the solid line representing the upstroke motion, the dashed line representing the downstroke motion and the blue line the values of static measurements.	66
4.33 Comparison of $\Delta C_{d_{pressure}}$ at different pitching frequencies. Where the blue lines represent the $A_{amplitude} = 5^\circ$ cases, the red lines the $A_{amplitude} = 10^\circ$ and the green lines the $A_{amplitude} = 15^\circ$	68

4.34 Comparison of C_l for unsteady cases at $\alpha_{mean} = 40^\circ$ and $Re = 250k$. The black line represents the mean value, with the solid line representing the upstroke motion, the dashed line representing the downstroke motion and the blue line the values of static measurements.	70
4.35 Comparison of C_l for unsteady cases at $\alpha_{mean} = 50^\circ$ and $Re = 250k$. The black line represents the mean value, with the solid line representing the upstroke motion, the dashed line representing the downstroke motion and the blue line the values of static measurements.	72
4.36 Comparison of C_l for unsteady cases at $\alpha_{mean} = 90^\circ$ and $Re = 250k$. The black line represents the mean value, with the solid line representing the upstroke motion, the dashed line representing the downstroke motion and the blue line the values of static measurements.	74
4.37 Comparison of ΔC_l at different pitching frequencies. Where the blue lines represent the $A_{amplitude} = 5^\circ$ cases, the red lines the $A_{amplitude} = 10^\circ$ and the green lines the $A_{amplitude} = 15^\circ$	76
4.38 Phase locked averaged flow fields (U/U_∞) for dynamic condition with $\alpha_{mean} = 40^\circ$, $f_{pitching} = 2\text{Hz}$ and $A_{pitching} = 15^\circ$	79
4.39 Phase locked averaged flow fields (U/U_∞) for dynamic condition with $\alpha_{mean} = 40^\circ$, $f_{pitching} = 3\text{Hz}$, and $A_{pitching} = 10^\circ$	81
4.40 Phase locked averaged flow fields (U/U_∞) for dynamic condition with $\alpha_{mean} = 50^\circ$, $f_{pitching} = 2\text{Hz}$ and $A_{pitching} = 15^\circ$	83
4.41 Phase locked averaged flow fields (U/U_∞) for dynamic condition with $\alpha_{mean} = 50^\circ$, $f_{pitching} = 3\text{Hz}$, and $A_{pitching} = 10^\circ$	85
4.43 Phase locked averaged flow fields (U/U_∞) for dynamic condition with $\alpha_{mean} = 90^\circ$, $f_{pitching} = 2\text{Hz}$ and $A_{pitching} = 15^\circ$	87
4.44 Phase locked averaged flow fields (U/U_∞) for dynamic condition with $\alpha_{mean} = 90^\circ$, $f_{pitching} = 3\text{Hz}$, and $A_{pitching} = 10^\circ$	89
A.1 Instantaneous vorticity field (ω/U_∞) with vector arrows that display the relative magnitude and direction of the flow in both x- and y-direction at $\alpha = 40^\circ$ and $Re = 250k$	97
A.2 Instantaneous flow field (U/U_∞) showing one full pitch cycle for the dynamic case at $\alpha_{mean} = 40^\circ$, $f_{pitching} = 1\text{Hz}$, $A_{pitching} = 15^\circ$ and $Re = 250k$	99
C.1 Proposed AI assisted workflow for literature studies.	106

List of Tables

3.1	Dimensions of Pressure Measurements Components.	28
3.2	A detailed presentation of configurations encompassing the dataset's various angles, amplitudes, and pitching frequencies.	29
3.3	Estimated number of vortex shed cycles captured within 5 seconds for varying Strouhal numbers (St) and wind speeds, demonstrating the sufficiency of acquisition time for static cases in LabVIEW.	29
3.4	Induced frequency values for different frequency cases.	30
3.5	Comprehensive list of components used in the experimental setup.	34
4.1	Performance metrics of the actuator in controlling pitching mechanism.	40
4.2	Measured dimensions of the pressure gauges tubes used during dynamic testing.	58

Nomenclature

Abbreviations

Abbreviation	Definition
2D	Two dimensional
3D	Three dimensional
AoA	Angle of Attack
ARE	Average Relative Error
B-L	Beddoes-Lieshman
CFD	Computational Fluid Dynamics
CMOS	Complementary Metal-Oxide-Semiconductor
DDES	Delayed Detached Eddy Simulation
DOF	Degree of Freedom
DS	Dynamic Stall
DW	Double Wake
EU	European Union
LEB	Leading Edge Bubble
LES	Large Eddy Simulations
LEV	Leading Edge Vortex
LSB	Leading-Edge Separation Bubble
NACA	National Advisory Committee for Aeronautics
ONERA	National Office for Aerospace Studies and Research
PIV	Particle Image Velocimetry
PSD	Power Spectral Density
RANS	Reynolds-Averaged Navier-Stokes
SA	Spalart-Allmaras
SST	Shear Stress Transport
TSR	Tip Speed Ratio
VAWTs	Vertical Axis Wind Turbines

Symbols

Symbol	Definition	Unit
$A_{pitching}$	Pitching Amplitude	[°]
C_d	Drag Coefficient	[-]
$C_{d_{pressure}}/C_{d_p}$	Drag Coefficient Calculated from the Pressure Distribution	[-]
C_{DM}	Corrected Drag Coefficient with Wake Distortion	[-]
$C_{D\infty}$	Corrected Drag Coefficient without Distortion	[-]
C_l	Lift Coefficient	[-]
$C'_{dynamic}$	Dynamic Lift Coefficient	[-]
$C'_{l_{max}}$	Maximum Lift Coefficient	[-]
$C'_{l_{pot}}$	Potential Lift Coefficient	[-]
$C'_{l_{steady}}$	Steady Lift Coefficient	[-]
C_M	Moment Coefficient	[-]
C_p	Pressure Coefficient	[-]
$C'_{N_{inv}}$	Normal Force Coefficient for the Inverted Airfoil	[-]

Symbol	Definition	Unit
$C_{L_{inv}}$	Lift Coefficient for the Inverted Airfoil	[-]
$C_{N,n}^f$	Trailing Edge Separation-Induced Unsteady Normal Force Coefficient	[-]
$C_{N,n}$	Total Unsteady Normal Force Coefficient	[-]
ΔC_D	Difference Between Corrected Drag Coefficients	[-]
ΔC_{l_1}	Incremental Change in Steady Lift from the Linear Part of the Model	[-]
ΔC_{l_2}	Variation in Lift Induced by the Non-linear Part of the Model	[-]
$\Delta C_{l_{pot}}$	Incremental Change in Potential Lift	[-]
Δt	Time Window	[s]
Δx	Displacement in the x-Direction	[m]
Δy	Displacement in the y-Direction	[m]
f	Shedding Frequency	[Hz]
$f_{pitching}$	Pitching Frequency of the Airfoil	[Hz]
ft_1	External Forcing as a Non-dimensional Derivative of $\Delta C_{l_{pot}}$	[-]
ft_2	Additional Forcing Term in the Non-linear Model	[-]
k	Reduced Frequency	[-]
k^2	Iteratively Derived Parameter for Blockage Factor	[-]
L	Lift Force	[N]
L'	Lift per Unit Span	[N/m]
M	Mach Number	[-]
M_e	Mach Number at the Edge of the Boundary Layer	[-]
p	Pressure	[Pa]
q	Dynamic Pressure	[Pa]
Re	Reynolds Number	[-]
s	Curvilinear Coordinate Along the Body Surface	[m]
S	Airfoil Area	[m ²]
S_t	Strouhal Number	[-]
T_1	Non-circulatory Time Constant	[s]
T_p	Time Constant for Pressure Lag	[s]
T_f	Time Constant for Effective Separation Point Lag	[s]
T_v	Vortex Decay Constant	[s]
T_{vt}	Non-dimensional Time Taken by the Vortex to Traverse the Chord	[-]
u	Velocity component in the x-direction	[m/s]
U_∞/V_∞	Velocity of the Free Stream	[m/s]
v	Velocity component in the y-direction	[m/s]
\vec{v}_i	Induced Velocity at a Point in Space due to a Vortex Filament	[m/s]
t	Thickness	[m]
t/c	Thickness-to-Chord Ratio of the Airfoil	[-]
$\alpha_{f,n}$	Effective Angle of Attack for Trailing Edge Separation	[degrees]
α_0	Zero lift angle of attack	[degrees]
β	Velocity Ratio	[-]
δ	Logarithmic Decrement	[-]
δ^*	Displacement Thickness	[m]
δ^{**}	Density Thickness	[m]
Γ	Circulation	[m ² /s]
μ	Dynamic Viscosity of Air	[N s/m ²]
μ_∞	Dynamic Viscosity of the Free Stream	[N s/m ²]
∇	Divergence Operator	[-]

Symbol	Definition	Unit
π	Number of Pi	[-]
ρ	Air Density	[kg/m ³]
ρ_∞	Density of the Free Stream	[kg/m ³]
σ	Flow Stagnation Parameter	[-]
τ	Time Constant	[s]
$\tau_{v,n}$	Vortex Time Parameter	[-]
θ	Momentum Thickness/ Blockage Factor for Bluff- Body Flow	[m]/ [-]
θ^*	Kinetic Energy Thickness	[m]
$\vec{\omega}$	Angular Velocity of a Fluid Element	[rad/s]
$\vec{\zeta}$	Vorticity	[1/s]
$\hat{\zeta}$	Damping Ratio	[-]

Contents

Acknowledgements	i
Abstract	ii
List of Figures	v
List of Tables	vi
Nomenclature	vii
1 Introduction	1
1.1 Wind Turbines and Load Cases	1
1.2 Relevance of The Research	2
1.3 Research Questions	2
2 Literature Review	4
2.1 Airfoil Aerodynamics	4
2.1.1 Static Aerodynamics	4
2.1.2 Deep Dynamic Stall	6
2.1.3 Vortex Shedding	7
2.1.4 Dynamic Inflow Conditions	9
2.2 Airfoil Aerodynamic Models	9
2.2.1 Vortex Wake Model	9
2.2.2 Double Panel Wake Model	10
2.2.3 CFD Modelling	12
2.3 Dynamic Stall Models	13
2.3.1 Snel's Model	13
2.3.2 Onera Model	15
2.3.3 Beddoes-Leishman Model	16
2.3.4 Dynamic Model Comparison	19
2.4 Experimental Methods	19
2.4.1 Pressure Measurements	19
2.4.2 Particle Image Velocimetry	20
2.4.3 Wind Tunnel Corrections	21
2.4.4 Reynolds Number	23
2.5 Computation Fluid Dynamics	24
3 Methods	26
3.1 Experiment Description	26
3.2 PIV Setup and Calibration	30
3.3 Component list	33
4 Results and Discussion	35
4.1 Reynolds Number Study	35
4.2 Actuator	37
4.3 Static Cases	40
4.3.1 Drag Coefficient	40
4.3.2 Lift Coefficient	42
4.3.3 Pressure Coefficient	44
4.3.4 PIV	46
4.4 Dynamic Cases	55
4.4.1 Cycle Convergence Study	55
4.4.2 Dynamic Pressure Response	57

4.4.3 Drag Coefficient	62
4.4.4 Lift Coefficient	69
4.4.5 PIV	77
5 Conclusion And Recommendations	90
5.1 Conclusion	90
5.2 Recommendations and Future Work	91
A Additional Flow Field Images	93
A.1 Instantaneous Vorticity Fields at $\alpha = 40^\circ$ and $Re = 250k$	94
A.2 Dynamic Case One Cycle Instantaneous Flow Fields	98
B Submitted Abstract Paper	100
C AI Assisted Literature Study Journal	104
Bibliography	107

1

Introduction

This chapter lays the foundation for comprehending the research on dynamic stall models applied to airfoils in deep stall conditions. It delves into the background of wind turbines, elucidating their operation, load cases, and the significance of the research in this domain.

1.1. Wind Turbines and Load Cases

Wind turbines play a pivotal role in the global pursuit of sustainable power generation, relying on intricate aerodynamic principles to convert kinetic energy from the wind into electrical power. A deeper understanding of these principles is crucial for optimizing efficiency, ensuring structural integrity, and advancing the field of wind energy.

At the core of wind turbine operation is the conversion of kinetic energy into electricity through the interaction between rotating blades and oncoming wind. As wind flows over the blades, it imparts aerodynamic forces, inducing rotation and driving the generator. Maximizing energy capture and enhancing overall performance necessitate a profound comprehension of the aerodynamics involved.

Aerodynamic load cases represent the forces and pressures exerted on wind turbine components during operation. Steady wind conditions generate constant aerodynamic loads on turbine blades, while turbulent winds introduce fluctuations and structural stability challenges. Dynamic stall events, occurring during rapid changes in wind conditions, pose unique challenges and are integral to wind turbine design. Dynamic stall, a critical aspect of wind turbine aerodynamics, occurs when the angle of attack changes rapidly, leading to unsteady forces. Understanding and mitigating dynamic stalls are essential for optimizing blade design and performance across diverse operational scenarios. Advanced modelling and simulation techniques are employed to predict and analyze these loads, ensuring that components endure various operating conditions throughout their lifespan.

Modern wind turbines operate under varying conditions, including routine operation, start-up, shut-down, and emergency scenarios. Each scenario presents unique challenges, requiring a detailed understanding of blade aerodynamics. The adaptability of wind turbines to different wind conditions is crucial, considering deployment in diverse geographic locations with varying wind speeds and atmospheric conditions. A flexible and adaptive aerodynamic design ensures optimal operation, contributing to a reliable and efficient energy generation process.

The current trend in wind turbine development underscores the importance of adaptability. Wind turbines must operate optimally across a range of environmental scenarios, contributing to reliable and efficient energy generation. This adaptability addresses challenges such as dynamic stall, optimizing designs for varying wind conditions, and contributes to the continual evolution of the wind energy field.

In summary, wind turbines are central to the global transition towards sustainable energy. Their nuanced aerodynamic operation and the diverse load cases they endure demand continual advancements in research and technology. By addressing challenges like dynamic stall and optimizing designs for varying wind conditions, the field of wind energy evolves, contributing to more efficient, reliable, and widespread adoption of this renewable energy source.

1.2. Relevance of The Research

The investigation into deep dynamic stall holds paramount significance in the context of wind turbines and contributes substantially to our broader understanding of aerodynamics. This exploration is critical for optimizing wind turbine efficiency, ensuring structural integrity, and advancing the comprehension of complex aerodynamic phenomena.

Dynamic stall, characterized by unsteady aerodynamic loads on wind turbine blades, is a phenomenon that significantly influences the performance of these renewable energy systems. Deep dynamic stall, in particular, refers to the occurrence of dynamic stall at high angles of attack, often associated with sudden changes in wind speed or turbulent conditions. Understanding and modeling deep dynamic stall are crucial for predicting and mitigating its effects on wind turbines.

One key relevance lies in the optimization of wind turbine design. The accurate prediction of unsteady aerodynamic loads during deep dynamic stall conditions is essential for designing blades that can withstand such challenges. By delving into the intricacies of deep dynamic stall, researchers and engineers can develop robust models that improve the aerodynamic performance of wind turbines. This optimization not only enhances energy capture but also contributes to the broader goal of making wind energy more cost-effective and sustainable.

Moreover, the research on deep dynamic stall is instrumental in ensuring the structural integrity and safety of wind turbines. The unsteady aerodynamic forces generated during deep dynamic stall conditions can induce significant fatigue and structural damage to turbine blades. A comprehensive understanding of deep dynamic stall enables the development of predictive models, allowing operators to implement maintenance strategies that prevent structural failures and enhance the long-term reliability of wind turbines.

In addition to its immediate applications in wind turbine technology, the study of deep dynamic stall contributes to the broader understanding of aerodynamics. Despite considerable advancements, dynamic stall remains a complex and challenging phenomenon that requires continuous investigation. Deepening our understanding of this aspect of aerodynamics provides valuable insights into the underlying physics and mechanisms at play. This, in turn, has broader implications for aerodynamic research across various applications beyond wind energy, potentially influencing fields such as aviation and transportation.

The global significance of renewable energy, particularly wind power, further underscores the relevance of deep dynamic stall research. As wind turbines are deployed in diverse geographic locations with varying wind conditions, a nuanced understanding of deep dynamic stall becomes imperative. Accurate predictions of aerodynamic loads under different scenarios are essential for ensuring the reliable and efficient operation of wind turbines across a spectrum of environmental conditions.

In conclusion, the research on deep dynamic stall is highly relevant for the optimization of wind turbine design and contributes significantly to our broader understanding of aerodynamics. By addressing challenges associated with dynamic stall, particularly at high angles of attack, researchers can enhance the efficiency and reliability of wind turbines. Furthermore, the insights gained from studying deep dynamic stall have implications beyond wind energy, impacting our understanding of aerodynamics across diverse applications. As we continue to advance in the pursuit of sustainable energy solutions, the exploration of deep dynamic stall remains a crucial avenue for improving the performance and longevity of wind turbines.

1.3. Research Questions

This research delves into the intricate realm of dynamic stall conditions, specifically focusing on the extreme scenario of very deep stalls where the angle of attack exceeds 25° . The investigation addresses critical aspects of aerodynamics by exploring the complex flow fields, variations in forces and moments on airfoil surfaces, and assessing the efficacy of current engineering and vortex models in predicting behaviour under deep dynamic stall. Recognizing the limitations of existing models, this study endeavours to pave the way for advancements in understanding and accurately representing deep stall phenomena. The ensuing research questions and hypotheses form the foundation for a comprehensive exploration of this challenging aerodynamic domain.

Flow Field in Deep Stall Conditions

Research Question: What does the flow field look like when the airfoil experiences very deep stall conditions with an angle of attack exceeding 25° ?

Hypothesis: In extreme stall conditions, turbulent and separated flow regions dominate, significantly increasing vortices, vortex shedding and breaking laminar aerodynamic patterns.

Forces and Moments in Deep Stall

Research Question: In the context of deep stall conditions, how do the forces and moments acting on the airfoil surface differ from those observed in light stall and static stall conditions?

Hypothesis: Forces and moments in deep stall exhibit erratic behaviour, characterised by historic variations and significantly heightened magnitudes, distinct from the more stable conditions observed in light and static stalls.

Effect of Pitching Frequency and Amplitude on the Flow in Deep Stall

Research Question: How do pitching frequency and amplitude affect the disparity between upstroke and downstroke values of drag and lift coefficients at different angles of attack, and what underlying aerodynamic mechanisms contribute to these variations?

Hypothesis: Higher pitching frequencies and larger amplitudes will increase the disparity between upstroke and downstroke values of drag and lift coefficients. This effect will be more pronounced at higher angles of attack due to the increased influence of unsteady aerodynamic phenomena such as vortex shedding and dynamic stall, which are expected to cause more significant deviations from static aerodynamic behaviour.

Vortex Shedding Behaviour in deep Dynamic Stall

Research Question: How do vortex shedding patterns change with different angles of attack during dynamic pitching, and what are the implications of these changes for the stability and control of the airfoil in unsteady aerodynamic conditions?

Hypothesis: At higher angles of attack during dynamic pitching, vortex-shedding patterns will become more irregular and chaotic. This irregularity will result in increased aerodynamic drag and decreased lift stability. As the angle of attack surpasses a certain threshold, the periodic vortex structures observed at lower angles will break down. This breakdown leads to more turbulent and erratic flow patterns. Consequently, the aerodynamic forces on the airfoil will fluctuate more significantly. The lift coefficient will show greater instability, with decreased mean values due to enhanced flow separation. The drag coefficient will increase as the chaotic vortex structures create more extensive wake turbulence. At lower angles, vortex shedding will be more organized, producing stable aerodynamic forces. However, at higher angles, the shedding frequency will become less distinct and more irregular. This transition to chaotic vortex shedding will negatively impact the airfoil's aerodynamic performance.

2

Literature Review

The Literature Review chapter serves as a panoramic exploration into the dynamic landscape of wind turbine aerodynamics, focusing on the intricate realm of deep dynamic stall. In this chapter, the latest advancements and foundational theories that underpin our understanding of unsteady aerodynamic environments are surveyed. From dynamic stall models to experimental analyses, a journey through the rich tapestry of research, scrutinizing diverse methodologies and illuminating critical insights will be given. By synthesizing the current knowledge base, this chapter sets the stage for the subsequent discussions, offering a comprehensive overview and establishing the context necessary to appreciate the nuances and challenges embedded in the exploration of deep dynamic stall in wind turbines.

2.1. Airfoil Aerodynamics

This section explores well-documented events and outcomes linked to relevant airfoils aerodynamics. Usually seen as a 2D occurrence, these effects are vital in standard wind turbine models. The discussion covers a broad overview of static airfoil aerodynamics, dynamic stall behavior, a detailed exploration of related phenomena, and a separate examination of vorticity shedding and its influence on airfoil loading, an aspect commonly left out of traditional dynamic stall models. The section wraps up with relevant observations.

2.1.1. Static Aerodynamics

Airfoils, the streamlined shapes fundamental to the performance of wings, propellers, and various aerodynamic surfaces, serve as the backbone of aviation and wind energy systems. To comprehend their functionality, it is imperative to delve into the diverse parameters governing their behavior as described by the book from Anderson (2017). The fundamental characteristic parameters of an airfoil are depicted in Figure 2.1 and include:

1. Chord Length (c): This is the straight-line distance between the leading and trailing edges of the airfoil. It serves as a crucial geometric parameter influencing lift and drag.
2. Thickness (t): Representing the maximum distance from the chord line to the upper or lower surface of the airfoil, thickness plays a pivotal role in determining the aerodynamic performance and structural considerations of the airfoil.
3. Angle of Attack (α): The angle formed between the chord line of the airfoil and the oncoming freestream flow. This parameter significantly affects lift and drag forces.
4. Mean Camber Line: An imaginary line that connects the midpoints of the upper and lower surfaces of the airfoil, providing a baseline for understanding the airfoil's curvature.
5. Maximum Camber: This refers to the maximum distance between the mean camber line and the chord line of the airfoil, influencing the overall shape and lift characteristics.
6. Camber Ratio: Calculated by dividing the maximum camber by the chord length, the camber ratio quantifies the curvature of the airfoil.
7. Aspect Ratio: Calculated as the ratio of wingspan to chord length, aspect ratio influences the lift-induced drag and overall aerodynamic efficiency.

8. **Leading Edge and Trailing Edge:** The leading edge represents the foremost edge of the airfoil, facing the oncoming airflow. It plays a vital role in initiating the airflow around the airfoil. On the other hand, the trailing edge is the rear edge of the airfoil. It marks the endpoint of the airflow over the airfoil and is crucial for minimizing turbulence and drag.

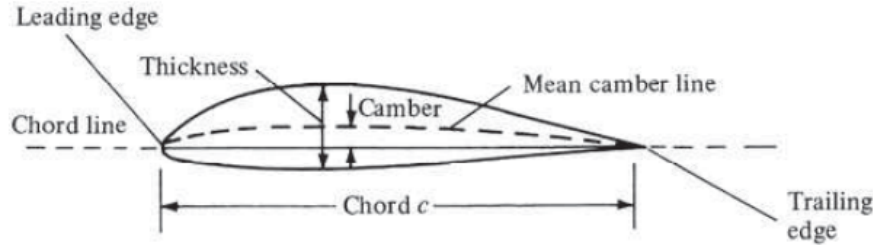


Figure 2.1: Airfoil illustration with important parameters indicated as from Anderson (2017).

The lift coefficient (C_l) is a dimensionless parameter crucial for understanding an airfoil's lift-generating capabilities. It is calculated by dividing the lift force (L) by the product of air density (ρ), the square of airspeed (V^2), and airfoil area (S). A higher lift coefficient signifies a greater lift force, a critical factor for aircraft needing to carry heavy loads or attain high speeds.

$$C_l = \frac{L}{\frac{1}{2}\rho V^2 S} \quad (2.1)$$

The drag coefficient (C_d) measures the airfoil's resistance to the flow of air. It is determined by dividing the drag force (D) by the product of air density (ρ), the square of airspeed (V^2), and airfoil area (S). A lower C_d indicates reduced drag force, crucial for optimizing the efficiency of aircraft, particularly in terms of fuel consumption.

$$C_d = \frac{D}{\frac{1}{2}\rho V^2 S} \quad (2.2)$$

The pressure coefficient (C_p) is a dimensionless parameter providing insights into the local pressure distribution around an airfoil. It is defined as the difference between local pressure (p) and freestream pressure (p_o), normalized by dynamic pressure ($\frac{1}{2}\rho V^2$). Understanding C_p aids in visualizing the airfoil's pressure distribution, offering valuable information about airflow patterns.

$$C_p = \frac{p - p_o}{\frac{1}{2}\rho V^2} \quad (2.3)$$

Stall is a critical aerodynamic occurrence linked to the variation of the lift coefficient (C_l) with the angle of attack (α). At low-to-moderate angles, C_l increases linearly with α , represented by the lift slope (a_0). In this range, smooth and attached airflow characterizes stable conditions. As α increases, flow separation from the airfoil's upper surface occurs, forming a wake of stagnant air. This separated flow, induced by viscous effects, leads to reversed flow and recirculation. The consequence at high α is a significant drop in lift and a simultaneous increase in drag, marking the onset of stall. The maximum lift coefficient ($C_{l,max}$) just before stall is crucial, determining the stalling speed of an airfoil. Higher $C_{l,max}$ values correspond to lower stalling speeds, impacting airfoil performance. This phenomenon can be seen as shown in Figure 2.2.

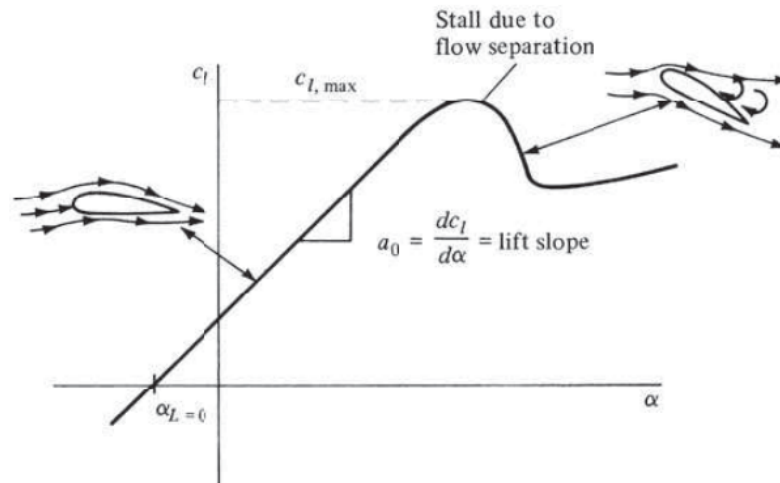


Figure 2.2: Lift polar showing how the lift coefficient varies with the angle of attack for a cambered airfoil by Anderson (2017).

In typical airfoil lift and drag polars, the angle of attack range is limited to approximately 0° to a few degrees beyond the angle of maximum lift coefficient. This restriction aligns with conventional aircraft theory, as they generally operate within this range of angles. However, as discussed in the context chapter, it's crucial to note that wind turbines, due to their specific placements, may encounter higher angles of attack. The study conducted by W. Timmer and Rooij (2001) addresses this by investigating the 360° lift and drag polars, depicted in Figure 2.3, for two distinct DU airfoils, providing valuable insights into situations involving elevated angles of attack.

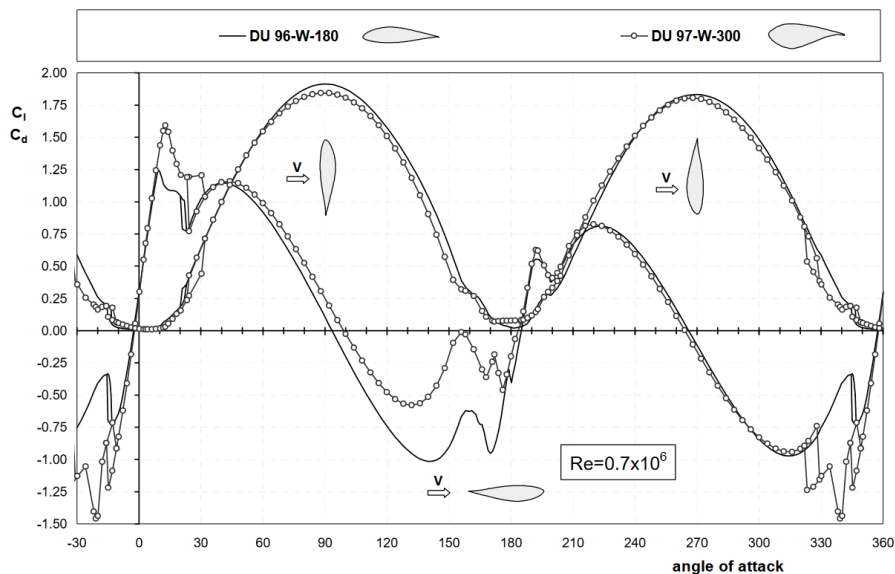


Figure 2.3: Investigating the performance of two DU airfoils across the entire 360° range of angles-of-attack by W. Timmer and Rooij (2001).

2.1.2. Deep Dynamic Stall

Deep Dynamic stall is a complex and critical aerodynamic phenomenon that occurs when an airfoil undergoes rapid and transient motion, resulting in a breakdown of the flow and a substantial reduction in lift. This phenomenon has significant implications for the performance and stability of various applications, including wind turbines and rotorcraft, McCroskey (1981). To comprehend deep dynamic stall, it is essential to delve into the intricacies of dynamic stall, examining key factors such as angle of attack (α), leading-edge vortex (LEV), aerodynamic damping, and the different flow stages.

The angle of Attack (α) plays a pivotal role in dynamic stall. Defined as the angle between the chord line of the airfoil and the direction of incoming flow, α determines the flow behaviour around the airfoil. When the α exceeds the static stall limit, dynamic stall is triggered, leading to a sudden increase in drag and a decrease in lift, McCroskey (1981). It is noteworthy that the α at which dynamic stall occurs surpasses that of static stall.

The formation of the Leading Edge Vortex (LEV) is a hallmark characteristic of dynamic stall. The LEV is a vortex that materializes near the leading edge of the airfoil during stall conditions. Generated by the separation of the boundary layer, the LEV plays a crucial role in delaying the onset of stall and augmenting lift, Corke and Thomas (2015). Understanding the intricacies of LEV formation is essential for predicting and mitigating the effects of dynamic stall.

Aerodynamic damping is another critical aspect influencing the behaviour of an airfoil during dynamic stall. It refers to the airfoil's ability to dampen vibrations caused by dynamic stall, and negative aerodynamic damping can lead to undesirable consequences, including limit-cycle oscillations and structural failure, Corke and Thomas (2015). Exploring the interaction between the airfoil and the flow field provides insights into the mechanisms governing aerodynamic damping and its role in dynamic stall.

Deep dynamic stall can be delineated into distinct flow stages, each characterized by specific flow behaviours. The pre-stall stage marks the initial phase, followed by the stall onset, fully stalled, and post-stall stages. Each stage is associated with unique phenomena, such as the development of the LEV, separation of the boundary layer, and shedding of vortices, R. Gupta and Ansell (2018) and Carr, Mcalister, and McCroskey (1977). An in-depth understanding of these stages is crucial for predicting the aerodynamic performance of airfoils during dynamic stall events and depicted in Figure 2.4.

Light dynamic stall represents the early stages of dynamic stall, where flow separation is limited, and the airfoil experiences small fluctuations in lift and drag. It is distinguished by the presence of a weak LEV and a gradual increase in drag Mallik and Raveh (2020). This phase is influenced by factors such as airfoil geometry, thickness, reduced frequency, and 3D effects, contributing to the overall complexity of dynamic stall.

Deep dynamic stall, in contrast, signifies the fully developed stage of dynamic stall. Here, flow separation becomes extensive, and the airfoil experiences significant fluctuations in lift and drag. This stage is characterized by the formation of a strong LEV, a substantial increase in drag, and a delayed reattachment of the flow, Mallik and Raveh (2020). The onset of moment stall, driven by the convecting vortex and the negative moment it induces, further distinguishes deep dynamic stall from its lighter counterpart.

2.1.3. Vortex Shedding

Vortex shedding is a phenomenon that occurs when a fluid flows past a bluff body, such as an airfoil or a cylinder, causing alternating vortices to form and detach from the body. These vortices are shed into the wake of the body and create a periodic pattern of flow structures. Vortex shedding is a complex process influenced by various factors, and understanding its characteristics is crucial in many engineering applications.

One important parameter associated with vortex shedding is the Strouhal number. The Strouhal number represents the ratio of the shedding frequency to the product of the characteristic length and the fluid velocity. It is a dimensionless quantity that characterizes the shedding frequency and provides insights into the dynamics of the vortices. According to Zhou, Dowell, and Feng (2019), the Strouhal number, given in Equation 2.4, is a fundamental parameter in the study of vortex shedding and is often used to predict the shedding frequency and its dependence on flow conditions. It is defined as shedding frequency (f) times the characteristic length (L) divided by the freestream velocity (V). The research provides valuable insights into how wind tunnel characteristics correlate with the Strouhal number. Additionally, A. Zanotti et al. (2014) delves into the influence of dynamic incoming flow conditions on the characteristic vortex shedding.

$$S_t = \frac{f \cdot L}{V} \quad (2.4)$$

In certain cases, vortex shedding can be self-induced, meaning that the flow itself triggers the shedding of vortices. Self-induced vortex shedding occurs when the flow separates from the body, leading to the formation of a leading-edge vortex (LEV) and subsequent shedding of vortices downstream. This

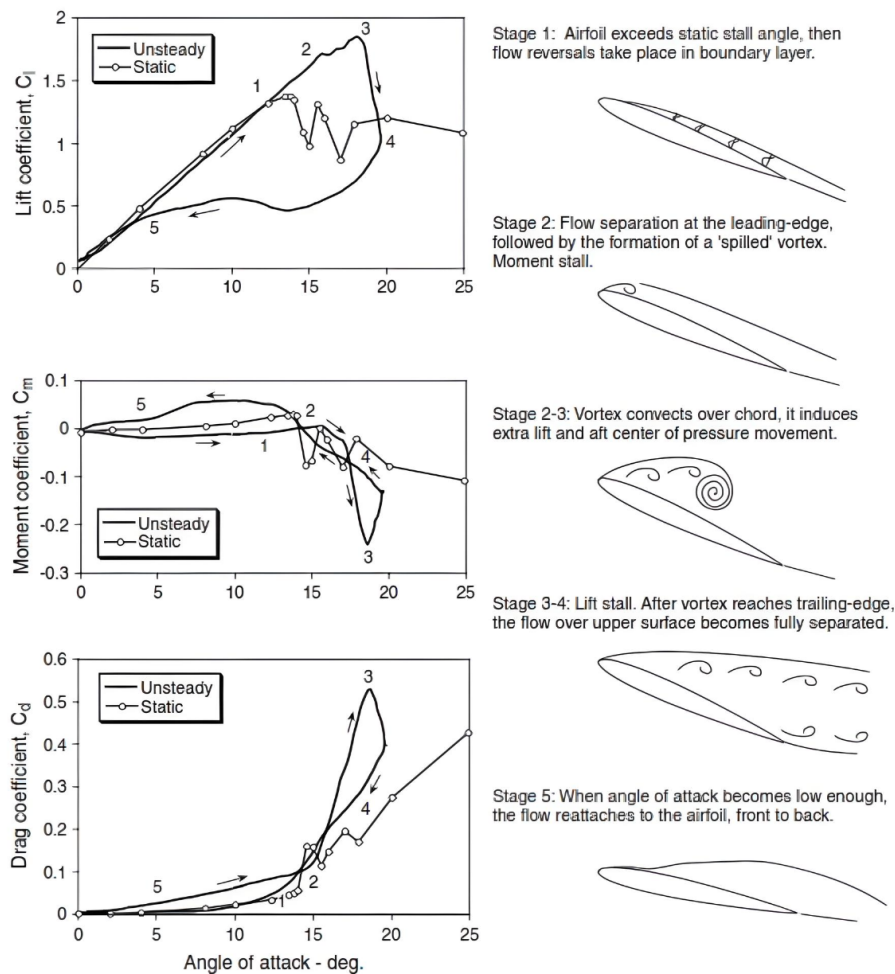


Figure 2.4: A visual representation showing the sequential stages of flow evolution within a dynamic stall hysteresis loop observed on a 2D oscillating airfoil from J. Gordon Leishman (2006).

phenomenon is particularly relevant in the context of dynamic stall, where the pitching motion of an airfoil induces unsteady flow conditions and the formation of vortices. Geissler and Haselmeyer (2006) investigated the onset procedure of dynamic stall and identified different flow phenomena triggering the dynamic stall process, including the self-induced shedding of vortices.

Vortex shedding also occurs under unsteady aerodynamic conditions, where the flow around the body is characterized by time-varying velocities and pressures. These unsteady conditions are often encountered in various engineering applications, including wind turbines, aircraft wings, and bridges. The study of vortex shedding provides insights into the unsteady flow behaviour and the interaction between the body and the surrounding fluid, Zhu, Wang, et al. (2020).

Vortex shedding is accompanied by unsteady pressure fluctuations, shear layer instabilities, and blade stability. The shedding of vortices creates unsteady flow patterns, resulting in fluctuations in the pressure distribution around the body. These unsteady pressure fluctuations can have significant effects on the aerodynamic performance and structural integrity of the body. M. Raffel, Kompenhans, and Wernert (1995) studied the unsteady flow velocity field above an airfoil pitching under deep dynamic stall conditions and measured the flow velocity field using particle image velocimetry (PIV). Their measurements provided insights into the dynamic stall process, including the formation and development of vortex structures and flow separation.

Shear layer instabilities play a crucial role in vortex shedding. The shear layer, formed at the separation point between the body and the wake, is susceptible to instabilities that contribute to the shedding of vortices. These instabilities can lead to the formation and growth of vortices, which eventually detach from the body and form the characteristic shedding pattern. The study by Alex Zanotti and Gibertini

(2013) also shows the modelling of dynamic loads on oscillating airfoils and emphasizes the importance of dynamic stall vortices in understanding the unsteady behaviour of the flow.

Blade stability is another important aspect related to vortex shedding, especially in the context of wind turbines. The interaction between the shedding vortices and the blades can lead to aerodynamic instabilities and affect the overall stability of the turbine. Understanding the dynamics of vortex shedding and its impact on blade stability is crucial for optimizing wind turbine design and performance. Elgammi and Sant (2016) combined unsteady blade pressure measurements with a free-wake vortex model to investigate the cycle-to-cycle variations in wind turbine aerodynamic blade loads in yaw conditions. Their study provides insights into the influence of rotor self-induced aerodynamic load fluctuations on the unsteady variations in blade loads.

2.1.4. Dynamic Inflow Conditions

The study of dynamic inflow conditions is crucial for unravelling the complexities of dynamic stall, a phenomenon significant in applications like wind turbines and rotorcraft. In this context, their theory underscores the importance of parameters such as reduced frequency, denoted by k , which characterises the rapidity of motion relative to the fluid.

Reduced frequency, defined as the ratio of the oscillation frequency to the fluid flow velocity over the chord length of the airfoil, is a key indicator of dynamic inflow conditions. The definition of the reduced frequency is given in Equation 2.5 and captures this dimensionless parameter, crucial for understanding the airfoil's motion relative to the fluid and its role in dynamic stall behaviours. It provides insights into the unsteadiness in aerodynamic responses, emphasizing that higher reduced frequencies are associated with highly unsteady behaviours. This understanding is crucial for optimizing aerodynamic performance, especially in scenarios where controlled aerodynamic forces play a pivotal role.

$$k = \frac{\pi \cdot f \cdot c}{V} \quad (2.5)$$

Studies by Zhu, Qiu, and Wang (2021) delve into the role of reduced frequency in dynamic stall, revealing its intricate relationship with dynamic inflow conditions. Their study showed a high reduced frequency results in heightened unsteadiness in aerodynamic responses. This increase in reduced frequency contributes to the postponement of dynamic stall onset and the enhancement of the maximum lift coefficient ($C_{l,max}$). Moreover, the impacts of the reduced frequency are particularly significant on the intensity of aerodynamic hysteresis. The practical implications of a delayed onset at higher reduced frequencies are particularly relevant in applications like wind turbines, where controlled aerodynamic forces are essential for efficient power generation.

The interaction between reduced frequency and other parameters, such as angle of attack, holds a critical role in deciphering dynamic stall. Accurate modeling and prediction of these factors become paramount, highlighting the importance of a comprehensive understanding of dynamic inflow conditions for effective design and operation in applications like wind energy systems.

2.2. Airfoil Aerodynamic Models

This chapter explores diverse aerodynamic models, including the vortex wake model, double panel model, and Computational Fluid Dynamics (CFD). Delving into their mechanisms, These models will be analyzed to enhance our understanding of aerodynamics and contribute to advancements in engineering applications.

2.2.1. Vortex Wake Model

Vortex wake models, integral to understanding intricate flow patterns, particularly in the context of wind turbine blades, are grounded in potential flow theory. These models explained fully by Anderson (2017) leverage a linearized potential flow solution, focusing on irrotational flow, to calculate velocities and pressures throughout the domain via the amalgamation of elementary flow solutions. The bedrock of these models heavily leans on the Biot-Savart law. According to this law, the induced velocity (v_i) at a specific point (P) in space, arising from a vortex filament with strength (ζ), is determined through the circulation (Γ), Equation 2.6. Circulation is defined either as a line integral encircling a closed curve (C) in a velocity field or, as per Stokes' theorem, as the surface integral of vorticity normal to the enclosed

surface, Equation 2.7. The vorticity is then a measure of flow rotation, defined as twice the angular velocity of a fluid element or the curl of the velocity field, Equation 2.8.

$$\vec{v}_i = \frac{\Gamma}{4\pi} \int \frac{d\vec{l}(\vec{r}_0 - \vec{r}_1)}{|\vec{r}_0 - \vec{r}_1|^3} \quad (2.6)$$

$$\oint \vec{v} \cdot d\vec{l} = \int_S \vec{\zeta} \cdot \vec{n} dS \quad (2.7)$$

$$\vec{\zeta} = 2\vec{\omega} = \nabla \cdot \vec{v} \quad (2.8)$$

Vorticity, signifying flow rotation, is articulated as twice the angular velocity (ω) of a fluid element or the curl of the velocity field. In the realm of vortex wake models for wind turbine blades, the lifting line or surface emulates the bound vorticity on the blade. Discretized into vortex line filaments, these filaments, adhering to Helmholtz's theorem, configure closed loops with unchanging strength as shown in Figure 2.5. The trailing and shed vorticity, equal in strength, collectively emulate the blade's wake. Biot-Savart law is instrumental in calculating the induced velocity at the blade, considering all vortex filaments, facilitating the determination of the angle of attack (α) at the blade sections. The α , in turn, is utilized to derive lift and drag coefficients from the static airfoil polar. The lift, consequently, aids in determining the bound circulation on a blade section in alignment with the Kutta–Joukowski theorem.

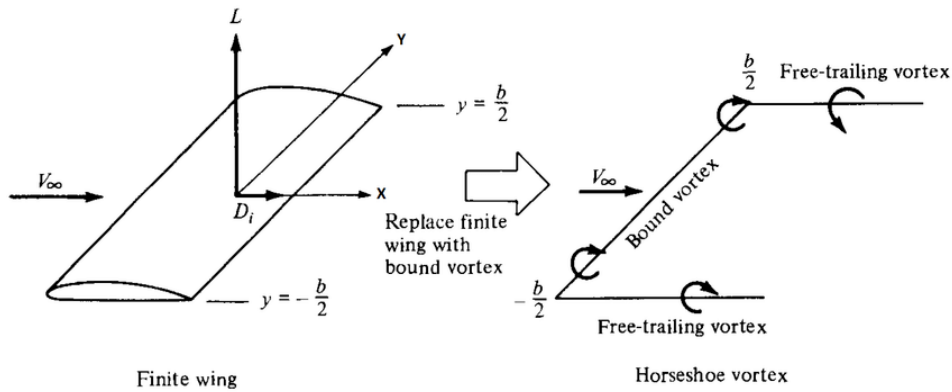


Figure 2.5: Demonstration of replacing the finite wing with a bound vortex and a trailing free vortex by Anderson (2017).

Expressed as $L' = \rho V \Gamma$, where ρ signifies air density, V denotes the incoming flow velocity, and Γ represents circulation, the lift per unit span (L') at a specific blade section is a pivotal parameter in the iterative process. This process involves comparing the newly calculated circulation value with the initial guess to attain a converged solution.

Vortex wake models are broadly categorized into two types: frozen wake models and free wake models. In frozen wake models, the wake geometry is predetermined based on rotor geometry and undisturbed flow, resulting in an unaltered wake. Conversely, free wake models consider the induction on the wake due to bound circulation on the blade and wake self-induction, leading to wake deformation. The latter, while offering enhanced accuracy, demands a higher computational time compared to the former.

2.2.2. Double Panel Wake Model

Zanon, Giannattasio, and C. J. Simão Ferreira (2013) elaborated the unsteady double wake viscous-inviscid vortex model for VAWTs, with a focus on dynamic stall modelling. The model combines inviscid and viscous effects, solving potential flow and integral boundary layer equations simultaneously through a semi-inverse iterative approach. Utilizing the "double wake" concept, vortex sheets are shed at both the trailing edge and separation location. Furthermore, the theory by Zanon, Giannattasio, and C. J. Simão Ferreira (2013) shows that Prandtl's boundary layer theory distinguishes regions with significant and negligible viscosity, resulting in the reduction of Navier-Stokes equations to Euler equations in the outer flow region.

$$\rho \left(\frac{\partial \vec{u}}{\partial t} + \vec{u} \cdot \nabla \vec{u} \right) = -\nabla p \quad (2.9)$$

In contrast, the boundary layer experiences non-negligible viscous effects, simplifying Navier-Stokes equations to boundary layer equations.

$$\rho \left(\frac{\partial \vec{u}_s}{\partial t} + u_s \frac{\partial u_s}{\partial s} + u_n \frac{\partial u_s}{\partial n} \right) = -\frac{\partial p}{\partial s} + \mu \frac{\partial^2 u_n}{\partial n^2}; \quad 0 = -\frac{\partial p}{\partial n} \quad (2.10)$$

The curvilinear coordinate along the body surface is represented by s , and its normal vector is represented by n . The boundary layer enforces the continuity equation.

$$\nabla \cdot \vec{u} = 0 \quad (2.11)$$

A vortex panel method, including a secondary wake, addresses inviscid flow with assumptions of incompressibility, irrotationality, and inviscidity in the outer region. Solutions are obtained through the distribution of elementary solutions on body surfaces using Green's identity, shown in Figure 2.6.

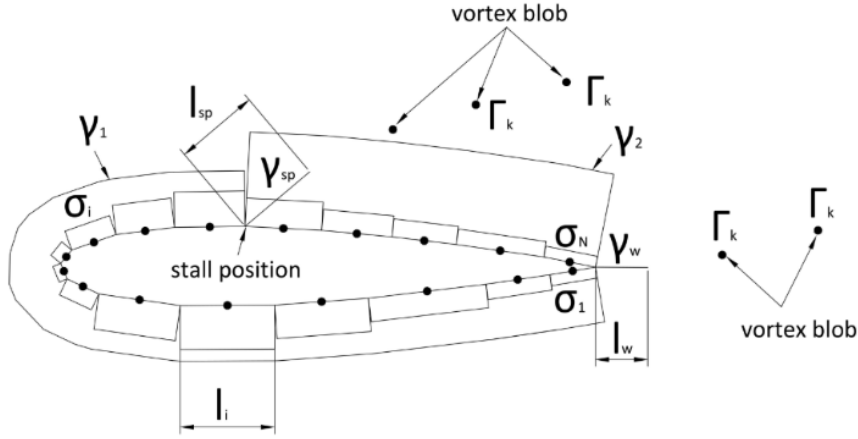


Figure 2.6: Illustration of the elementary distribution within the DW model during separated flow by Zanon, Giannattasio, and C. J. Simão Ferreira (2013).

Drela and Giles (1987)'s integral boundary approach computes boundary layer flow for steady conditions, providing relations derived from mass and momentum conservation laws. These relations include momentum and kinetic energy shape parameter equations, integral equations governing thicknesses, and dissipation coefficients. Accommodating laminar and turbulent boundary layers, the method is reliable and versatile, notably in the widely-used XFOIL vortex panel model.

$$\frac{\partial(\rho u_s)}{\partial s} + \frac{\partial(\rho u_n)}{\partial n} = 0; \quad \rho u_s \frac{\partial u_s}{\partial s} + \rho u_n \frac{\partial u_n}{\partial n} = \rho_e u_e \frac{\partial u_w}{\partial s} + \frac{\partial \tau}{\partial n} \quad (2.12)$$

The symbols s and n have the same meaning as in Equation 2.10, while e represents the edge of the boundary layer. τ denotes the sum of total shearing and shear stress. The first relation proposed by Drela can be derived by integrating the momentum equation across the boundary layer.

$$\frac{s}{\theta} \frac{d\theta}{ds} = \frac{s}{\theta} \frac{C_f}{2} - \left(\frac{\delta^*}{\theta} + 2 - M_e^2 \right) \frac{s}{u_e} \frac{du_e}{ds} \quad (2.13)$$

The kinetic energy integral equation constitutes the second relation. It arises by multiplying the momentum by velocity, yielding a kinetic energy equation. Integration across the boundary layer follows, leading to:

$$\frac{s}{\theta^*} \frac{d\theta^*}{ds} = \frac{s}{\theta^*} 2C_D - \left(\frac{2\delta^{**}}{\theta^*} + 3 - M_e^2 \right) \frac{s}{u_e} \frac{du_e}{ds} \quad (2.14)$$

with

$$\begin{aligned}
 \text{Momentum thickness:} & \quad \theta = \int_0^{\infty} \left(1 - \frac{u_s}{u_e}\right) \frac{\rho u_s}{\rho_e u_e} dn \\
 \text{Displacement thickness:} & \quad \delta^* = \int_0^{\infty} \left(1 - \frac{\rho u_s}{\rho_e u_e}\right) dn \\
 \text{Skin friction:} & \quad C_f = \frac{2}{\rho_e u_e^2} \tau_w \\
 \text{Mach number:} & \quad M_e \\
 \text{Kinetic energy thickness:} & \quad \theta^* = \int_0^{\infty} \left(1 - \left(\frac{u_s}{u_e}\right)^2\right) \frac{\rho u_s}{\rho_e u_e} dn \\
 \text{Density thickness:} & \quad \delta^{**} = \int_0^{\infty} \left(1 - \frac{\rho}{\rho_e}\right) \frac{u_s}{u_e} dn \\
 \text{Dissipation coefficient:} & \quad C_D = \frac{1}{\rho_e (u_e)^3} \int_0^{\infty} \tau \frac{\partial u_s}{\partial n} dn
 \end{aligned}$$

The elaboration by YU et al. (2023) further explains that the viscous-inviscid model operates under the quasi-steady flow approximation for the boundary layer, suitable for slower aerofoil motion ($k < 0.15$). Post-separation solutions in inviscid and viscous regions are integrated with the introduction of a transpiration velocity coupling term, capturing changes in outer flow due to airfoil presence. The baseline model's validation encompasses clean airfoils in steady conditions and dynamic stall scenarios. For a comprehensive understanding of the baseline double wake model's development and validation, the original work by Zanon, Giannattasio, and C. J. Simão Ferreira (2013) must be consulted.

2.2.3. CFD Modelling

Computational Fluid Dynamics (CFD) has emerged as a powerful tool in the field of aerodynamics, providing researchers with a virtual arena for in-depth investigations into complex flow phenomena. One prominent turbulence model, the Spalart-Allmaras (SA) model, has gained attention for its efficiency and accuracy in predicting separated flows, making it particularly well-suited for simulating static deep stall conditions.

The Spalart-Allmaras turbulence model takes centre stage in simulating static conditions at these critical angles. Its one-equation formulation proves advantageous in capturing the complexities of separated flows, demonstrating promising results in static deep stall scenarios. The SA Coder AFT model, a variant of the SA model, has been extensively employed in dynamic stall predictions, showcasing its versatility across different airfoil geometries and Reynolds numbers.

Studies comparing the SA Coder AFT model with other turbulence models, such as the k-omega SST and MPANS models, highlight its effectiveness in predicting the head-flow discharge relation with good agreement against experimental data. The model exhibits a deviation of less than 3% in the head coefficient, emphasizing its capability to capture the essential flow features during dynamic stall. Notably, the SA Coder AFT model's performance aligns closely with results obtained from Large Eddy Simulations (LES), showcasing its reliability in predicting aerodynamic loads.

In-depth analyses focusing on specific angles of attack reveal the SA model's robustness in capturing static conditions. For angles of 40° and 50° s, the SA model effectively predicts the onset of dynamic stall vortex, providing valuable insights into the aerodynamic behaviour during oscillatory motion. Its ability to capture the formation and collapse of the leading-edge separation bubble (LSB) and subsequent development of the dynamic stall vortex (DSV) further solidifies its position as a promising turbulence model for static deep stall simulations.

However, it is crucial to acknowledge the SA model's limitations. Sensitivity to the choice of wall functions and near-wall treatment poses a challenge, impacting the accuracy of flow physics near the wall. Additionally, being a one-equation turbulence model, the SA model may not capture all the complexities of turbulent flow accurately. These limitations underscore the need for ongoing research to explore the model's performance in various scenarios and to validate predictions against more experimental data.

Integrating insights from studies by Geissler and Haselmeyer (2006), Bather and Lee (2022), Huang et al. (2021), Yang et al. (2019), and Srinivasan, Ekaterinaris, and McCroskey (1995), it becomes ev-

ident that the SA turbulence model is just one piece of the puzzle in the broader landscape of CFD simulations for static deep stall. Each turbulence model brings its strengths and limitations, necessitating a thoughtful consideration of the specific requirements of the simulation.

The SA Coder AFT model's conjunction with the Delayed Detached Eddy Simulation (DDES) approach, combining the advantages of Reynolds-Averaged Navier-Stokes (RANS) and LES methods, provides a more detailed analysis of flow features associated with dynamic stall. This innovative approach allows for a comprehensive exploration of the aerodynamic behaviour at a reasonable computational cost, showcasing the adaptability of the SA model in different simulation methodologies.

Adding to the wealth of research, The study from Huang et al. (2021) emphasizes the SA model's capability to predict aerodynamic loads during dynamic stall accurately. By capturing the oscillations around the region of the LSB and the propagation of the DSV, the SA Coder AFT model demonstrates its potential to understand the intricate details of flow dynamics during dynamic stall phenomena. The early onset of lift stall and slight underprediction of peak lift coefficient compared to LES results suggest areas for further refinement.

The work from Geissler and Haselmeyer (2006) reinforces the promising results of the SA model in predicting the head-flow discharge relation with less than 3% deviation from experimental values. This consistency across various operation conditions emphasizes the model's effectiveness in capturing the complex flow physics associated with static deep stall.

The addition of the insights of Yang et al. (2019) further solidifies the SA model's standing in CFD simulations for static deep stall. By predicting the dynamic loads of airfoils during deep stall with promising results, the SA model showcases its applicability across different airfoil geometries. The study's emphasis on the need for further research to compare the SA model's performance with other turbulence models and validate predictions against experimental data underscores the ongoing efforts in refining and advancing CFD methodologies.

The contribution of Srinivasan, Ekaterinaris, and McCroskey (1995) delves into the SA model's wide-spread use in dynamic stall predictions. The study's findings, emphasizing the model's success in predicting head-flow discharge relations and investigating the effect of airfoil thickness on the onset of dynamic stall, further contribute to the comprehensive understanding of the SA model's capabilities.

In conclusion, the Spalart-Allmaras turbulence model emerges as a valuable asset in the arsenal of CFD simulations, particularly for static deep stall scenarios. Its efficiency, accuracy, and versatility make it a preferred choice for capturing the complex flow physics associated with separated flows. However, researchers acknowledge its limitations and advocate for ongoing research to refine its performance, compare it with other turbulence models, and validate predictions against a broader range of experimental data. As CFD continues to evolve, the Spalart-Allmaras model remains a cornerstone, contributing to a deeper understanding of aerodynamic phenomena and pushing the boundaries of virtual experimentation.

2.3. Dynamic Stall Models

In this section, the three prominent dynamic stall models—Snel's Model, Onera Model, and Beddoes-Leishman Model are delved into. Anchored in steady airfoil polars, their efficacy hinges on the accuracy of this data. Each model, however, grapples with unique limitations. The ONERA model, dependent on a linearization assumption for small angle-of-attack changes, may not accurately represent wind turbine behavior in yaw conditions. Snel's model leans heavily on mathematical modeling to replicate lift hysteresis around a steady polar, offering limited insight into flow physics. Acknowledging these intricacies is pivotal for comprehending the nuanced applications and constraints of each dynamic stall model.

2.3.1. Snel's Model

In response to the need for replicating the effects of periodic vortex shedding in the deep stall regime, the Snel dynamic stall model was conceived by Truong (1993). Unlike the conventional models, this approach requires minimal parameter tuning, relying extensively on mathematical reasoning to emulate dynamic stall effects. The model comprises two essential components: a linear part described by a first-order ordinary differential equation and a non-linear part governed by a second-order non-linear differential equation. The total dynamic lift is expressed as the sum of the steady lift and the changes

introduced by both components:

$$C_{l_{dynamic}} = C_{l_{steady}} + \Delta C_{l_1} + \Delta C_{l_2} \quad (2.15)$$

Here, the incremental change in steady lift (ΔC_{l_1}) emanates from the linear part of the model, converging to zero in the absence of forced excitation. Conversely, ΔC_{l_2} represents the variation in lift induced by the non-linear part, tapering to zero solely within the attached flow regime of the lift curve. In the stall regime, ΔC_{l_2} introduces high-frequency fluctuations to the steady lift.

Moving to the specifics of the conventional linear model, it is encapsulated by the following differential equation:

$$\tau \frac{d\Delta C_{l_1}}{dt} + cf_{10}\Delta C_{l_1} = ft_1 \quad (2.16)$$

Here, τ denotes the time constant, representing the time taken by the flow to traverse one semi-chord ($\tau = \frac{c}{2U}$). The time-dependent coefficients ft_1 and cf_{10} are elucidated, with ft_1 , given in Equation 2.17, embodying the external forcing as a non-dimensional derivative of $\Delta C_{l_{pot}}$. Additionally, $\Delta C_{l_{pot}}$ is defined as given in Equation 2.18, and cf_{10} manifests the stiffness of the restoring behaviour, given in Equation 2.19. In this mathematical expression, the parameter E assumes a value of 80 during the upstroke and 60 during the downstroke, reflecting an anticipation of heightened stiffness in the downward stroke, Holierhoek et al. (2013).

$$ft_1 = \tau \frac{d\Delta C_{l_{pot}}}{dt} \quad (2.17)$$

$$\Delta C_{l_{pot}} = 2\pi \sin(\alpha - \alpha_0) - C_{l_{steady}} \quad (2.18)$$

$$cf_{10} = \frac{1 + 0.5\Delta C_{L_{pot}}}{8(1 + E\tau(d\alpha/dt))} \quad (2.19)$$

Transitioning to the non-linear segment, governed by a second-order non-linear differential equation, complexities are introduced through contributions from ΔC_{l_2} in the coefficients cf_{20} and cf_{21} , representing stiffness and damping coefficients, respectively:

$$\tau^2 \frac{d^2\Delta C_{l_2}}{dt^2} + cf_{21} \frac{d\Delta C_{l_2}}{dt} + cf_{20}\Delta C_{l_2} = ft_2 \quad (2.20)$$

The intricate nature of this non-linear equation becomes evident in the formulations for cf_{20} , Equation 2.21, and cf_{21} , Equation 2.22, shedding light on the complex interplay of factors influencing dynamic stall behaviour.

$$cf_{20} = k_s^2 \left[1 + 3(\Delta C_{l_2}^2) \right] \left[1 + 3 \left(\frac{d\alpha}{dt} \right)^2 \right] \quad (2.21)$$

$$cf_{21} = \begin{cases} 60\tau k_s [-0.01(\Delta C_{l_{pot}} - 0.5) + 2(\Delta C_{l_2})^2] & \text{if } \frac{d\alpha}{dt} \geq 0 \\ 2\tau k_s & \text{if } \frac{d\alpha}{dt} \leq 0 \end{cases} \quad (2.22)$$

The inclusion of forcing through ft_2 further enriches the model's capability to account for external influences:

$$ft_2 = 0.1k_s \left(-0.15\Delta C_{L_{pot}} - 0.05 \frac{d\Delta C_{l_{pot}}}{dt} \right) \quad (2.23)$$

The Snel dynamic stall model, originating from Truong's formulation, utilizes these differential equations to capture both lower and higher-order effects during dynamic stall. This model is distinguished by its minimal reliance on airfoil-specific parameters, ensuring ease of implementation while encompassing higher-order dynamics essential for considering vortex shedding in this research.

The model has recently refined, as detailed in Adema, Kloosterman, and Schepers (2020) research. A notable advancement entails the transition from utilizing lift coefficients to normal force coefficients

within the equations. This adjustment, coupled with the adoption of a specific normal force coefficient curve as opposed to the conventional 2π value for attached flow, has significantly enhanced the model's predictive accuracy.

Further adjustments have been made to specific model parameters. The k_s value, for instance, is now contingent on projected values, establishing a direct correlation between shedding frequency and the angle of attack. Additionally, fine-tuning of the first-order parameter, as expressed in Equation 2.24, reflects a nuanced optimization process.

$$cf_{10} = \begin{cases} \frac{1+0.2\Delta C_{L_{inv}}}{8(1+60\tau(d\alpha/dt))} & \text{if } \frac{d\alpha}{dt} C_{N_{inv}} \leq 0 \\ \frac{1+0.2\Delta C_{L_{inv}}}{8(1+80\tau(d\alpha/dt))} & \text{if } \frac{d\alpha}{dt} C_{N_{inv}} > 0 \end{cases} \quad (2.24)$$

The fine-tuning process extends to the second-order parameters, as evidenced by the comparison between the expressions provided in Equation 2.39, Equation 2.41, and Equation 2.38 against their earlier counterparts, namely Equation 2.35, Equation 2.37, and Equation 2.36. This meticulous examination delves into the nuanced adjustments made to the values of specific parameters embedded within the coefficients. The overarching objective behind these refinements is to elevate the overall performance of the model, a goal rooted in empirical insights derived from wind tunnel experiments involving pitching airfoils.

$$cf_{20} = 10(k_s \sin(\alpha))^2 \left[1 + 3(\Delta C_{l_2}^2) \right] \left[1 + 280^2 \tau^2 \left(\frac{d\alpha}{dt} \right)^2 \right] \quad (2.25)$$

$$cf_{21} = \begin{cases} 60\tau k_s [-0.01(\Delta C_{l_{pot}} - 0.5) + 2(\Delta C_{l_2})^2] & \text{if } \frac{d\alpha}{dt} \geq 0 \\ 60\tau k_s [-0.01(\Delta C_{l_{pot}} - 0.5) + 14(\Delta C_{l_2})^2] & \text{if } \frac{d\alpha}{dt} \leq 0 \end{cases} \quad (2.26)$$

$$ft_2 = 0.01k_s \left(-0.04\Delta C_{L_{pot}} + 1.5 \frac{d\Delta C_{l_{pot}}}{dt} \right) \quad (2.27)$$

A notable aspect of these adaptations is the increased integration of the parameter τ in the second-order equation, strategically applied to reduce dependence on velocity. These refinements draw inspiration from empirical insights obtained through wind tunnel experiments involving pitching airfoils, contributing to a more resilient model performance.

2.3.2. Onera Model

The ONERA Model, initially developed in the early 1980s by Tran and Petot (1980), underwent modifications by Peters (1985) to accommodate large angles of attack and reversed flow. A plunging degree of freedom was introduced as a forcing input, enhancing stability. The model focuses on the dynamic lift coefficient, later improved to include dynamic drag and moment.

The model comprises a 1st order linear differential equation modelling the attached flow region of the lift curve and a 2nd order non-linear differential equation modelling the stall regime. Despite its usefulness in dynamic stability analysis, a drawback is the requirement for a significant number of tuning parameters determined through an identification procedure involving oscillating airfoil wind tunnel tests. The ONERA model equations as given by Holierhoek et al. (2013) are as follows:

$$\dot{C}_{l_1} + \lambda_L C_{l_{pot}} + (\lambda_L s_L + \sigma_L) \dot{\alpha} + s_L \ddot{\alpha} \quad (2.28)$$

$$\ddot{C}_{l_2} + a_L \dot{C}_{l_2} + r_L C_{l_2} = -(r_L \Delta C_l + e_L \Delta \dot{C}_l) \quad (2.29)$$

$$C_{l_{dynamic}} = C_{l_1} + C_{l_2} \quad (2.30)$$

Equations are differentiated concerning non-dimensional time: $s = 2Utc$. The parameters λ , s_L , and σ_L depend on the angle of attack (α) and can be obtained from unsteady experimental data or flat plate values. Meanwhile, coefficients a_L , r_L , and e_L are functions of the difference between potential flow lift and static lift from steady airfoil polars, given by:

$$\Delta C_l = C_{l_{pot}} - C_{l_{static}} \quad (2.31)$$

$$r_L = \left[r_0 + r_2(\Delta C_l)^2 \right]^2; \quad a_L = a_0 + a_2(\Delta C_l)^2; \quad e_L = e_2(\Delta C_l)^2 \quad (2.32)$$

The model necessitates the determination of a larger number of parameters, all requiring experimental data. In the absence of data, the "mean airfoil", as defined by Holierhoek et al. (2013), can be used. The inclusion of higher-order differential equations enables the model to capture unsteady behaviour beyond stall, making it applicable to diverse conditions, contingent on accurate parameter determination.

2.3.3. Beddoes-Leishman Model

The B-L model, Originally designed by John Gordon Leishman and Beddoes (1989) for helicopter applications, S. Gupta and J. Gordon Leishman (2006) later adapted the model to suit wind turbine scenarios, conducting tests on a S809 airfoil, is a widely recognized and extensively tested dynamic stall model in scientific literature, with its primary objective being the emulation of physical mechanisms governing dynamic stall phenomena. These mechanisms involve the delayed lift coefficient of attached flow, the deferred onset of flow separation, and the enhanced lift coefficient through the introduction of a convecting leading-edge vortex.

The B-L model encapsulates the governing physical mechanisms of dynamic stall within four distinct modules, and their outcomes are combined linearly to derive the overall unsteady lift. The forcing input takes the form of angle of attack (α) variations over time. Utilizing an indicial formulation, the B-L model is well-suited for acquiring transient solutions in a time-marching manner. The discussion on each constituent module of the model is based on references by John Gordon Leishman and Beddoes (1989) and S. Gupta and J. Gordon Leishman (2006).

Attached Flow

In the first phase of the model, the airflow remains attached to the airfoil. The theory by Theodorsen (1935) is employed to capture the time delay in the loading response to changes in the angle of attack. This response comprises two components. Firstly, there is a circulatory part, influenced by the wake behaviour and featuring a time delay expressed in Equation 2.33 with $\alpha_{E,n}$ representing the effective angle of attack at the airfoil section. The basis for this module lies in Theodorsen's theory of unsteady flow over a flat plate. A rational function approximation of Theodorsen's function models the lag in lift build-up resulting from a sudden change (step) in the angle of attack. The indicial lift responses derived from this function are superimposed using the Duhamel integral over time, providing the circulatory part of the lift associated with the wake behind the airfoil. In the following Equation 2.34 and Equation 2.35, b_1 and b_2 represent the time constants of the lag equations, while A_1 and A_2 are their respective coefficients. The dimensionless time is introduced by normalizing with $\Delta S = \frac{2V\Delta t}{c}$.

$$C_{N,n}^C = C_{N_\alpha}(\alpha_{E,n} - \alpha_0) = C_{N_\alpha}(\alpha_n - X_n - Y_n - \alpha_0) \quad (2.33)$$

$$X_n = X_{n-1}e^{-b_1\Delta S} + A_1\Delta\alpha_n e^{-b_1\Delta S/2} \quad (2.34)$$

$$Y_n = Y_{n-1}e^{-b_2\Delta S} + A_2\Delta\alpha_n e^{-b_2\Delta S/2} \quad (2.35)$$

Additionally, a non-circulatory element is incorporated, stemming directly from the airfoil's motion. This introduces both an added mass impact and an impulse loading contribution, as delineated in the subsequent equations. In these mathematical expressions, depicted in Equation 2.36 and Equation 2.37, D_n represents the deficiency function. For the examination of how disturbances propagate across the airfoil, the non-circulatory time constant, denoted as $T_1 = c/a$, comes into play. This time constant is then scaled by a factor K_α , determined by the Mach number, following the insights provided by John Gordon Leishman and Beddoes (1989).

$$C_{N,n}^I = \frac{4K_\alpha c}{V} \left(\frac{\Delta\alpha_n}{\Delta t} - D_n \right) \quad (2.36)$$

$$D_n = D_{n-1}e^{-\Delta t/K_\alpha T_1} + \left(\frac{\Delta\alpha_n - \Delta\alpha_{n-1}}{\Delta t} \right) e^{-\Delta t/2K_\alpha T_1} \quad (2.37)$$

The sum between $C_{N,n}^C$ and $C_{N,n}^I$, shown in Equation 2.38, serves as a pivotal factor in ascertaining the comprehensive force coefficient acting on the airfoil. By combining these terms, the analysis unfolds the nuanced dynamics between circulatory and non-circulatory contributions, offering insights into the overall forces experienced by the airfoil during its motion.

$$C_{N,n}^p = C_{N,n}^C + C_{N,n}^I \quad (2.38)$$

Trailing Edge Separation

Within the framework of this model, the second phase addresses the intricacies of trailing-edge separation. The objective of this module is to capture the non-linear effects inherent in flow separation, employing Kirchhoff's theory and introducing a dimensionless parameter denoted as f . This parameter, representing the effective separation point, is derived from experimental static loading curves, a process expounded upon by S. Gupta and J. Gordon Leishman (2006).

Ensuring accuracy in this representation involves the modelling of pressure and viscous lag to account for the time delay characteristic of flow separation. The definition of loading draws from Kirchhoff's theory and is adaptable for larger angles of attack. To achieve this, the conventional small angle assumption is discarded, and the sine of the angle of attack is considered instead. This strategic adjustment aims to provide a more nuanced and precise depiction of the dynamic interplay involved in flow separation, particularly at higher angles of attack.

$$C_N = C_{N,\alpha} \left(\frac{1 + \sqrt{f}}{2} \right)^2 (\alpha - \alpha_0) \quad (2.39)$$

Upon rearranging the aforementioned expression, the dimensionless parameter f can be formulated as a function of the angle of attack. Extracting C_N and α values from static airfoil data, a piece-wise exponential function is employed to achieve a continuous and smooth variation of f with α . However, it's imperative to note that since f corresponds to static flow behaviour, modifications are required for its application in unsteady flows. In the context of unsteady flow, trailing edge separation encounters lag attributed to leading-edge pressure and boundary layer development. The integration of pressure lag is facilitated through the following equation:

$$C'_{N,n} = C_{N,n}^p - D_{p,n} \quad (2.40)$$

$$D_{p,n} = D_{p,n-1}e^{-\Delta S/T_p} + \left(C_{N,n}^p - C_{N,n-1}^p \right) e^{-\Delta S/2T_p} \quad (2.41)$$

The Mach number-dependent time constant T_p exhibits relative independence from airfoil shape and can be derived from unsteady airfoil data. Utilizing $C'_{N,n}$, an alternative effective angle of attack, denoted as α_f , is ascertained. This α_f is subsequently employed in determining another effective separation point, expressed as $f' = f(\alpha_f)$. In addition, an additional first-order filter, shown in Equation 2.43 Equation 2.44, is applied to the effective separation point to account for the effects of boundary layer lag.

$$\alpha_{f,n} = \frac{C'_{N,n}}{C_{N,\alpha}} + \alpha_0 \quad (2.42)$$

$$f'_n = f'_n - D_{f,n} \quad (2.43)$$

$$D_{f,n} = D_{f,n-1}e^{-\Delta S/T_f} + \left(f'_n - f'_{n-1} \right) e^{-\Delta S/2T_f} \quad (2.44)$$

The eventual trailing edge-induced unsteady normal force coefficient can be calculated with the following equation:

$$C_{N,n}^f = C_{N\alpha} \left(\frac{1 + \sqrt{f_n''}}{2} \right)^2 (\alpha_{E,n} - \alpha_0) + C_{N,n}^I \quad (2.45)$$

Leading Edge Separation

Under static conditions, the initiation of leading edge separation occurs with the attainment of a critical leading edge pressure. Given the direct proportionality between leading edge pressure and the normal force coefficient C_N , a straightforward criterion is established based on a critical value of C_N , denoted as C_{N_1} . This criterion serves to modify a non-dimensional vortex time parameter (τ_v), tracking the location of concentrated vorticity.

It is noteworthy that in unsteady scenarios, there exists a lag in leading-edge pressure, implying that the critical condition will be reached at a higher angle of attack (α) than in static conditions. To account for this effect, a comparison is made between C_N and C_{N_1} . The vortex time parameter undergoes updates during each time iteration, contingent upon meeting the critical conditions. In the absence of meeting these conditions, the parameter is reset to zero at the commencement of an upstroke cycle.

$$\tau_{v,n} = \begin{cases} \tau_{v,n-1} + \frac{0.45V_2\Delta t}{c} & \text{if } C_N' > C_{N_1} \\ 0 & \text{if } C_N' < C_{N_1} \text{ and } \Delta\alpha_n > 0 \end{cases} \quad (2.46)$$

Vortex Lift

The amplification of lift, expressed through the normal force coefficient, is facilitated by the Leading Edge Vortex (LEV) as long as it remains positioned over the upper surface of the airfoil. The Vortex Lift Module is designed to emulate this physical mechanism of dynamic stall, wherein the induced lift contribution from the LEV, commonly referred to as vortex lift, is calculated and combined with the lift generated by the trailing edge separation module to yield the overall unsteady lift. The augmentation of vortex lift is contingent upon the vortex maintaining its position over the airfoil surface; once it surpasses the trailing edge, its contribution diminishes and ceases to increase. The vortex time parameter plays a crucial role in determining when the vortex has traversed the airfoil's trailing edge. The increment in vortex lift is determined by the specific Equation 2.47.

$$C_{v,n} = C_{N,n}^C (1 - K_{N,n}) \quad (2.47)$$

$$K_{N,n} = \left(\frac{1 + \sqrt{f_n''}}{2} \right)^2 \quad (2.48)$$

Equation 2.49 for the total accumulated vortex lift increments only when the Leading Edge Vortex begins convecting over the upper surface, specifically when $0 < \tau_{v,n} < T_l$. While the LEV remains attached and undergoes growth at the leading edge, its impact on lift is minimal. Therefore, in this condition, the total accumulated vortex lift experiences exponential decay with a vortex decay constant, T . Notably, T_l represents the non-dimensional time taken by the vortex to traverse the chord. Both T_v and T_{vl} exhibit independence from the Mach number and a loose dependency on airfoil shape, with determinations derived from unsteady airfoil data.

$$C_{N,n}^v = \begin{cases} C_{N,n-1}^v \exp\left(-\frac{\Delta S}{T_v}\right) + (C_{v,n} - C_{v,n-1}) \exp\left(-\frac{\Delta S}{2T_v}\right) & \text{if } 0 < \tau_{v,n} < T_{vl} \\ C_{N,n-1}^v \exp\left(-\frac{\Delta S}{T_v}\right) & \text{else} \end{cases} \quad (2.49)$$

Combining

Each section within the model corresponds to a distinct flow regime characterized by different parameters, as previously discussed. However, certain parameters are contingent on airfoil data and necessitate calibration for each specific airfoil. It is important to highlight that the original development of this model was tailored for rotorcraft applications. Although it has been adjusted for wind turbines and their operational conditions, as demonstrated by S. Gupta and J. Gordon Leishman (2006), there is a notable limitation in modelling vortex shedding continuously.

In the final phase, the vortex shedding is singular, and its impact on loading would not recur without variations in inflow conditions. This characteristic restricts the model from accounting for higher-order effects. Consequently, applying the model to the specific problem under consideration appears unattainable. Ultimately, to obtain the total unsteady normal force, Equation 2.50, at each time sample, a linear sum combines the normal force from Equation 2.45 and Equation 2.49.

$$C_{N,n} = C_{N,n}^f + C_{N,n}^v \quad (2.50)$$

2.3.4. Dynamic Model Comparison

In Snel's Model, deep stall correction terms are integrated into the aerodynamic loading calculations for blade sections encountering dynamic stall. Empirical or semi-empirical relationships are employed to adjust lift and drag coefficients under deep stall conditions, ensuring accurate representation. These modifications are then seamlessly integrated into the noise prediction equations, accounting for deep stall's impact on noise generation.

For the Onera Model, the wake model is extended to accommodate the effects of deep stall on rotor wake structure. Adjustments in aerodynamic interaction coefficients within the model equations are made to reflect altered flow conditions during deep stall. Additional turbulence models or corrections are incorporated to address heightened turbulent intensity associated with deep stall.

In the Beddoes-Leishman Model, dynamic stall modeling is enhanced to accurately capture deep stall phenomena using advanced dynamic stall models or empirical corrections. Unsteady aerodynamic force coefficients are adjusted to reflect deep stall's impact on blade motion and airfoil characteristics. These adjustments are seamlessly integrated into the noise prediction formulations within the Beddoes-Leishman Model framework.

The comparison methodology involves several steps. Deep stall characterization begins with simulations or experimental tests to ascertain critical parameters such as stall onset angle, stall delay, and post-stall lift and drag characteristics. Implementation in MATLAB follows, with deep stall methods being integrated into each model using scripts or functions. Ensuring consistency in treatment across all models is paramount. Validation against experimental data is then conducted, comparing model predictions against data gathered from wind tunnel or flight tests on rotor systems experiencing deep stall conditions. Quantitative comparison metrics, including mean absolute error, root mean square error, and correlation coefficient, are computed to quantify agreement between model predictions and experimental data. Finally, sensitivity analysis is performed to assess parameter influences on deep stall predictions, identifying critical parameters and their implications.

2.4. Experimental Methods

This section delves into crucial aspects of aerodynamic experimentation, encompassing pressure measurement techniques, the application of PIV, corrections in wind tunnel testing, and the impact of Reynolds number variations. Understanding these elements is paramount for accurate assessments of aerodynamic performance and flow characteristics in experimental setups.

2.4.1. Pressure Measurements

Examining flow-dynamic pressure involves scrutinizing how a physical entity deforms under localized pressure forces, employing various methods to convert this deformation into a digital signal indicative of pressure as elaborated by Tropea, Yarin, and Foss (2007). Measurements within the flow include static pressure, total pressure, and velocity, each acquired through distinct techniques.

Gauging static pressure involves assessing pressure perpendicular to flow streamlines. This is typically done using pressure taps with small orifices on a model's surface, linked to pressure sensors. Measuring total pressure in the flow involves using a probe designed to interact with the stream flow direction, inducing flow stagnation for local total pressure assessment. Specialized probes assist in minimizing directional sensitivity and enhancing pressure accuracy in scenarios where flow direction is uncertain or unsteady.

Pressure-differential devices, frequently employed in aviation and high-performance vehicle applications, combine total pressure and static pressure measurements to determine dynamic pressure. For scenarios emphasizing flow direction and velocity components, multi-hole directional probes become crucial. These probes, featuring symmetrically arranged holes around a central channel, yield varied

pressure readings based on flow incidence angles. Achieving accurate determination of flow magnitude and direction is facilitated through calibration in three-axis components, although their adoption is restricted by high costs and intricate calibration procedures.

In aerodynamic investigations, obtaining pressure (and velocity) data within a model's wake is essential. Using either single probes or arrays to traverse the measurement domain captures pressure values, creating a two-dimensional pressure map. To minimize flow disruption, these probes are designed to be inconspicuous, with a consideration of viscosity effects to maintain pressure measurement precision. Various commercially available solutions cater to the requirements of such measurements.

2.4.2. Particle Image Velocimetry

In the intricate setup of a PIV system, first introduced by Adrian (1984), various interconnected subsystems play pivotal roles in capturing and analyzing velocity fields. The entirety of the theory is explained in the book from Markus Raffel et al. (2007) and explains the following. Tracer particles are introduced into the fluid flow, undergoing illumination twice within a brief temporal window, Δt . The resulting scattered light is meticulously recorded using high-quality lenses, either on a high-resolution digital or film camera or on two separate frames employing specialized cross-correlation digital cameras. Post-processing involves digitizing the photographic PIV recording through a scanner, with the digital sensor output directly transferred to the computer's memory for subsequent analysis.

Digital PIV recordings are segmented into smaller subareas termed "interrogation areas." The statistical method of cross-correlation is then employed to compute the displacement vector $\mathbf{d} = [\Delta x, \Delta y]$ for particles within each window between time instants t and $t + \Delta t$. This method, inclusive of auto- and cross-correlation, determines local displacement vectors for tracer particles between consecutive illuminations, aiding in the calculation of velocity components using the equations:

$$u = \frac{\Delta x}{M\Delta t} \quad (2.51)$$

$$v = \frac{\Delta y}{M\Delta t} \quad (2.52)$$

These account for the time delay between illuminations and the magnification during imaging. This process is iterated for all interrogation areas in the PIV recording.

Technological advances enable modern charge-coupled device (CCD) cameras to capture over 100 PIV recordings per minute. High-speed recording on complementary metal-oxide-semiconductor (CMOS) sensors facilitates acquisition in the kilohertz range. Evaluation of a digital PIV recording, comprising numerous instantaneous velocity vectors, typically takes seconds with standard computers. For applications requiring faster data rates, specialized software algorithms are available, performing evaluations with reduced precision within fractions of a second. This practical theory necessary for set-up is illustrated in Figure 2.7

Before diving into technical details, it's important to address broader aspects to aid in understanding. PIV, as an optical technique, distinguishes itself from other flow velocity measurement methods by its non-intrusive nature, making it applicable in high-speed flows and boundary layers close to walls where probes may disturb the flow.

Additionally, PIV involves indirect velocity measurement, akin to laser Doppler velocimetry, gauging the fluid element's velocity by measuring tracer particle velocities within the flow. PIV's whole-field technique, recording large parts of flow fields in various applications, sets it apart from other techniques providing velocity information at a single point with high temporal resolution.

Spatial resolution in PIV captures instantaneous images with clarity, allowing detection of spatial structures in unsteady flow fields. However, temporal resolution remains limited by current technological constraints, warranting careful consideration when comparing PIV results with traditional techniques.

Key factors during PIV implementation include assessing tracer particle fidelity, considering particle size for velocity lag, balancing illumination exposure in gas flows, and ensuring a homogeneous distribution of tracer particles for optimal recording quality.

Temporal resolution in PIV systems has improved with high-speed lasers and cameras, enabling time-resolved measurements. Spatial resolution, determined by interrogation area size, ensures accurate results in regions with significant velocity gradients. PIV's repeatability stands out, allowing the exchange of recordings for evaluation without repeating experiments.

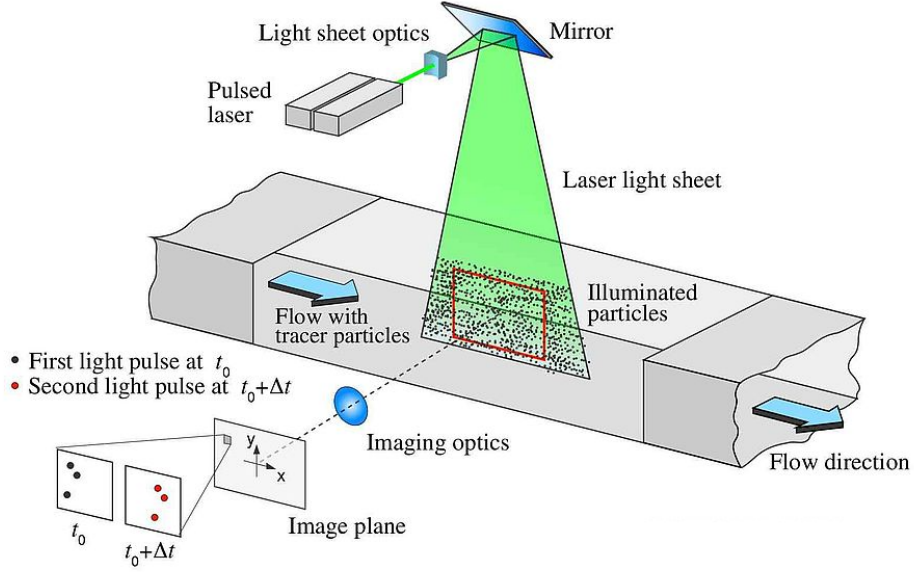


Figure 2.7: Configuration of the 2D 2 component PIV experimental setup, illustrating the tracer particles illuminated by the first light pulse at time t (depicted in black) and the subsequent light pulse at $t + \Delta t$ (depicted in red). Markus Raffel et al. (2007)

2.4.3. Wind Tunnel Corrections

From the basics of Garner et al. (1966) for subsonic wind tunnel corrections, the summary by W. A. Timmer (2021) has led to the following equations for wind tunnel correction, which are mainly applicable in lower angle of attack and since the main aim of this research are higher angles of attack this will only be explicitly named. All derivation can be found in studies by Ewald (1998), Ewald (1998) and W. A. Timmer (2021).

The foundational work by Garner et al. (1966) and subsequent investigations, as synthesized by W. A. Timmer (2021), have established fundamental equations for subsonic wind tunnel corrections, primarily suited for lower angles of attack. In this research, which focuses on higher angles of attack, specific corrections are derived from studies by Ewald (1998) and W. A. Timmer (2021). While the comprehensive derivations are detailed in Ewald's and Timmer's works, the following equations will give the basis of wind tunnel corrections.

$$\alpha = \alpha' + \frac{\sigma}{2\pi\beta} (C'_l + 4C'_m) \quad (2.53)$$

$$C_l = C'_l \left[1 - \frac{\sigma}{\beta^2} + 5.25 \frac{\sigma^2}{\beta^4} - \frac{(2-M^2)}{\beta^3} \Lambda \sigma \left(1 + \frac{1.1\beta}{(t/c)} \alpha^2 \right) - \frac{(2-M^2)(1+0.4M^2)}{4\beta^2} \left(\frac{c}{h} \right) C'_d \right] \quad (2.54)$$

$$C_d = C'_d \left[1 - \Delta C_d^* - \frac{(2-M^2)}{\beta^3} \Lambda \sigma \left(1 + \frac{1.1\beta}{(t/c)} \alpha^2 \right) - \frac{(2-M^2)(1+0.4M^2)}{4\beta^2} \left(\frac{c}{h} \right) C'_d \right] \quad (2.55)$$

$$C_m = C'_m \left[1 - \frac{(2-M^2)}{\beta^3} \Lambda \sigma \left(1 + \frac{1.1\beta}{(t/c)} \alpha^2 \right) - \frac{(2-M^2)(1+0.4M^2)}{4\beta^2} \left(\frac{c}{h} \right) C'_d \right] + C'_l \left(\frac{\sigma}{4\beta^2} - 1.05 \frac{\sigma^2}{\beta^4} \right) \quad (2.56)$$

$$q = q' \left[1 + \frac{(2-M^2)}{\beta^3} \Lambda \sigma \left(1 + \frac{1.1\beta}{(t/c)} \alpha^2 \right) + \frac{(2-M^2)(1+0.4M^2)}{4\beta^2} \left(\frac{c}{h} \right) C'_d \right] \quad (2.57)$$

$$Re = Re' \left[1 + \frac{(1 - 0.7M^2)}{\beta^3} \Lambda \sigma \left(1 + \frac{1.1\beta}{(t/c)} \alpha^2 \right) + \frac{(1 - 0.7M^2)(1 + 0.4M^2)}{4\beta^2} \left(\frac{c}{h} \right) C'_d \right] \quad (2.58)$$

Addressing Challenges in Deep-Stall Region Measurements

As the separation distance on the wind tunnel model increases, the impact of wake-induced blockage becomes increasingly pronounced, emerging as a dominant factor in the overall blockage within the test section. W. Timmer and Rooij (2001) explain that in such scenarios, conventional treatments for small perturbations due to blockage lose their validity. Particularly in the deep-stall region of angles of attack, where flow separation occurs from the leading edge, the two-dimensional airfoil model transforms its behaviour, resembling that of a bluff body. Correction methods for addressing wall interference effects in closed test sections, specific to bluff bodies, fall into two categories: those utilizing the measured drag of the model and those relying on the measured pressure distribution on the walls, known as the wall-signature method.

Maskell (1963) introduced a method to rectify wall interference effects when dealing with separated flow over bluff bodies. The method, initially developed for bluff bodies, proves applicable to stalled wings due to the similarity of the heavily separated region of the model to bluff body wakes. Maskell established a dynamic pressure correction based on the measured drag due to separation and specific geometric parameters. The invariance principle, confirmed experimentally, asserts the constancy of the pressure distribution on the model in the test section under wall constraint, leading to the expression:

$$\frac{C'_D}{k'^2} = \frac{C'_D}{(1 - C'_{pb})} = \text{const} \quad (2.59)$$

Here, C'_D is the measured drag coefficient, defined as $\frac{D'}{q'S}$, with S representing a representative area of the body, q' the dynamic pressure, and C'_{pb} the base pressure coefficient. The corrected drag coefficient (C_{DM}) is then determined as:

$$C_{DM} = \frac{C'_D}{1 + \theta \frac{S}{C} C'_D} \quad (2.60)$$

Here, θ is the blockage factor for bluff-body flow given by:

$$\theta = \frac{1}{k^2 - 1} \quad (2.61)$$

The parameter k^2 is iteratively derived using the measured mean base pressure as a starting value.

Application for Two-Dimensional Model Assumption

To calculate the blockage factor for a two-dimensional flat plate, Maskell utilized experimental results from Fage and Johansen (1927). Limitations of the method at higher $\frac{c}{h}$ values were recognized, prompting corrections based on comparisons with drag curves from different correction schemes. Notably, the method based on the model rear pressure proved inadequate for two-dimensional flow with $\frac{S}{C}$ values significantly larger than those in Maskell's measurements.

W. Timmer and Rooij (2001) continues to elaborate a refined analysis, that accounts for a blockage factor slightly larger than 0.96, which was proposed for improved agreement between drag curves at varying $\frac{c}{h}$ values. Acknowledging the significance of variations in measurement techniques when comparing drag curves with different $\frac{c}{h}$, the study offered valuable insights.

In scenarios where the airfoil generates lift, corrections on the angle of attack for streamlined flow are traditionally based on the alteration of streamline curvature due to the presence of walls. However, in two-dimensional models experiencing deep stall, where streamlines at the model location are approximately straight, arguments suggest that there is no need for an angle of attack correction.

The study from Hackett (1996) approaches to correcting lift and moment coefficients using Maskell's method involves a two-step procedure to account for wake distortion. The process begins by determining ΔC_D , defined as the difference between the corrected drag coefficient (C_{DM}) and the corrected drag coefficient without distortion ($C_{D\infty}$):

$$\Delta C_D = C_{D_M} - C_{D_\infty} \quad (2.62)$$

This ΔC_D term is then incorporated into the calculation of C_{D_∞} :

$$C_{D_\infty} = C_{D_M} - \Delta C_D = \frac{C_{D_M}}{1 + \theta \frac{S}{C} (C_{D_M} - \Delta C_D)} \quad (2.63)$$

Lift (C_L), moment (C_M), and pressure (C_p) coefficients can be corrected for wake blockage using the ratio of dynamic pressures:

$$\frac{q'}{q} = \frac{C_{D_\infty}}{C'_D} = \frac{C_{L_\infty}}{C'_L} = \frac{C_{M_\infty}}{C'_M} = \frac{1}{1 + \theta \frac{S}{C} (C_{D_M} - \Delta C_D)} \quad (2.64)$$

$$\frac{q'}{q} = \frac{-C_{P_\infty} + 1}{-C'_P + 1} = \frac{1}{1 + \theta \frac{S}{C} (C_{D_M} - \Delta C_D)} \quad (2.65)$$

Importantly, the negative sign in the result of ΔC_D is crucial, indicating that C_{D_∞} is larger than C_{D_M} . This methodology offers a comprehensive framework for correcting lift and moment coefficients in the presence of wake distortion, providing valuable insights into aerodynamic performance.

While Maskell's method proves effective in various scenarios, limitations arise when dealing with higher $\frac{c}{h}$ values. Neglecting terms on the order of $(\frac{S}{C})^2$ in Maskell's derivation restricts the method's applicability, as noted by Cooper in Ewald (1998). There is evidence suggesting that Maskell's method may over-correct at high area ratios.

Further investigations and comparisons with alternative correction methods may be necessary to assess the method's performance for significantly higher $\frac{c}{h}$ values and to understand its limitations.

2.4.4. Reynolds Number

Having delved into the intricacies of aerodynamics, it's essential to highlight the significance of dimensionless numbers. In the previous sections the Strouhal Number, subsection 2.1.3, and the Reduced Frequency, subsection 2.1.4, both of which have been elucidated in more detail. As a small reminder, The Strouhal Number (S_t), a dimensionless parameter, plays a pivotal role in understanding vortex shedding frequency dynamics, particularly in dynamic stall scenarios. Similarly, the Reduced Frequency (k), a non-dimensional metric, has been thoroughly investigated, symbolizing the oscillatory patterns within the incoming flow. To replicate this oscillatory motion, airfoil testing involves pitch simulations rather than inducing oscillatory inflow on a static blade. Directly calculated from the airfoil's pitching frequency, the reduced frequency of the flow becomes a crucial parameter in these analyses.

However, the last important dimensionless number is the Reynolds Number as it plays a crucial role in determining the aerodynamic characteristics of airfoils. As the Reynolds number increases, the flow around an airfoil undergoes significant changes, impacting lift, drag, and stall behaviour. The Reynolds number, taken from Anderson (2017), is defined as the ratio of inertial forces to viscous forces and is a key parameter in determining the flow regime around an airfoil. In the context of airfoils, the Reynolds number is particularly significant in low-speed aerodynamics, where viscous effects dominate the flow behaviour.

$$Re = \frac{\rho_\infty V_\infty c}{\mu_\infty} \quad (2.66)$$

At low Reynolds numbers, the flow around an airfoil is characterized by laminar separation and early stall. As the Reynolds number increases, the flow transitions from laminar to turbulent, leading to delayed stall characteristics. The impact of Reynolds number on the aerodynamic performance of airfoils has been extensively studied, revealing important insights into the behavior of airfoils under varying flow conditions.

The influence of Reynolds number on airfoil performance is evident in polar plots, which depict the variation of lift and drag coefficients with angle of attack. At low Reynolds numbers, the polar plots exhibit distinct characteristics, with sharp stall behavior and limited lift capabilities. As the Reynolds number increases, the polar plots evolve, showcasing delayed stall and improved lift characteristics. This transition is particularly significant as it signifies the convergence of polar plots after a certain threshold Reynolds number.

Research by Arunvinthan and Nadaraja pillai (2019)) provides valuable insights into the impact of Reynolds number on the aerodynamic characteristics of unsymmetrical airfoils under turbulent inflows. The study highlights that the coefficient of lift increases with the increase in turbulence intensity at different Reynolds numbers. Additionally, the presence of turbulence effectively delays the stall characteristics of the airfoil by attaching the flow over the airfoil for an extended region. This emphasizes the role of Reynolds number in influencing the aerodynamic performance of airfoils under turbulent inflows, particularly in relation to lift and stall characteristics.

Furthermore, the effects of Reynolds number on low-speed aerodynamics are discussed in the book "Low-Speed Wind Tunnel Testing Third Edition" by Barlow, Rae, and Pope (1999). The book emphasizes the significance of the Reynolds number as a key parameter in low-speed wind tunnel testing and its impact on drag coefficient, boundary layer behaviour, and profile drag. It also addresses the challenges associated with acquiring accurate data at very low Reynolds numbers, highlighting the importance of low turbulence and precise measurements.

The convergence of polar plots for airfoils after a certain threshold Reynolds number signifies the transition from laminar to turbulent flow regimes, leading to improved aerodynamic performance. Understanding the influence of the Reynolds number on airfoil behaviour is essential for optimizing airfoil designs and predicting their performance under varying flow conditions.

2.5. Computation Fluid Dynamics

In the realm of CFD simulations, OpenFOAM stands out as a widely used open-source software package known for its versatility and robustness. Researchers leverage this tool to delve into the intricate aerodynamic behaviour associated with various angles of attack. Focusing on critical angles of 40° and 50° , where dynamic stall phenomena are expected to manifest prominently, CFD simulations aim to bridge the gap between experimental and numerical analyses.

In carrying out a detailed CFD investigation for both stationary and moving conditions, the initial choice of angles at 40° and 50° is derived from observations in Figure 2.3. These angles were selected because they clearly exhibit characteristics associated with deep stall phenomena and operate within the linear portion of the drag graph. This decision aligns with the goal of gaining comprehensive understanding of aerodynamic performance in scenarios involving both static and dynamic conditions. For these angles, a systematic methodology is proposed of pitching amplitudes of 5° , 10° , and 15° at varying frequencies of 1 to 4 Hz, 2 and 3 Hz and 2 and 3 Hz respectively.

- **Geometry and Mesh Generation:**

Begin by defining the geometric model of the airfoil for both 40° and 50° angles of attack. Employ OpenFOAM's mesh generation capabilities to create a refined computational mesh that adequately captures the intricacies of the flow around the airfoil. Ensure that the mesh is sensitive to boundary layer resolution near the surface to address potential sensitivity to near-wall treatments

- **Boundary and Initial Conditions:**

Set up appropriate boundary conditions to simulate the static and dynamic scenarios. For the dynamic cases, incorporate the prescribed pitching motion with amplitudes and frequencies specified. Define initial conditions based on the flow's desired starting state, considering the simulation's static or dynamic nature .

- **Numerical Solver and Turbulence Model:**

Utilize OpenFOAM's solvers, such as the transient solver for dynamic cases, and select the Spalart-Allmaras (SA) turbulence model for its proven efficiency in capturing separated flows. Implement the SA Coder AFT model, considering its successful application in dynamic stall predictions across different airfoil geometries.

- **Simulation Setup:**

Configure the simulation parameters, including time step sizes, convergence criteria, and solution monitoring. For dynamic cases, synchronize the simulation time with the prescribed pitching frequencies to accurately capture the oscillatory behaviour of the airfoil.

- **Post-Processing and Validation:**

Employ OpenFOAM's post-processing tools, such as ParaView, to analyze the simulation results. Quantitatively assess aerodynamic coefficients, flow patterns, and dynamic stall characteristics.

Validate the simulation outcomes by comparing them against available experimental data and, where applicable, reference Large Eddy Simulations (LES) results.

- Sensitivity Analysis and Refinement:

Conduct sensitivity analyses to evaluate the impact of variations in parameters such as mesh density, time step size, and turbulence model settings. Refine the simulation setup iteratively to address any discrepancies and enhance the accuracy of predictions.

By adhering to this methodical approach, the proposed CFD study aims to provide a comprehensive understanding of the aerodynamic phenomena associated with static and dynamic stall at critical angles of 40° and 50° , contributing valuable insights to the existing body of research in the field.

3

Methods

To understand dynamic stall phenomena and their correlation with simulation models, a comprehensive experimental testing campaign was conducted in a state-of-the-art wind tunnel. This section delves into the intricacies of the experimental setup, detailing the methodology, parameters measured, and the dynamic testing procedures employed.

3.1. Experiment Description

Experimental procedures begin in a specially designed wind tunnel facility, carefully set up to study detailed aerodynamics. The integration of pressure taps and Particle Image Velocimetry (PIV) emerges as a comprehensive methodology to study the behaviour of the test model. The experiment includes a range of attack angles, specifically chosen to cover various aerodynamic situations seen in the real world.

At Delft University of Technology's Faculty of Aerospace Engineering, the Low-Speed Low Turbulence Wind Tunnel (LTT) features an octagonal test section. The dimensions of this section are a width of 1.80 m, a height of 1.25 m, and a length of 2.60 m. Notably, the tunnel's contraction ratio is 17.6, allowing it to reach a maximum test section velocity of 100 m/s. The turbulence intensity is consistently low, starting at 0.015 % at 10 m/s and increasing to 0.07 % at 75 m/s, as also given by C. Simão Ferreira et al. (2009).

In this carefully controlled aerodynamic study, the NACA643418 airfoil is examined with dimensions of a 250mm chord, where the maximum thickness is 17.9% at 34.8% chord and the maximum camber is 2.2% at 50% chord. The airfoil was tested at various angles of attack: 10°, 40°, 50°, 90°, 130°, 160°, and 170°. Each angle is chosen to cover specific points in the 180° lift polar of the blade section. The 10° angle is chosen because it remains within the attached flow regime. In contrast, the 40° and 50° angles are well into the deep stall regime, situated roughly at the peak of the C_l curve on the expected polar plot. The 90° angle is selected due to its association with the highest drag, which is expected to exhibit significant vortex structures. Angles above 90° are chosen similarly to those below 90°, but with the trailing edge leading the flow. This detailed approach aims to give us a good overall picture of how the airfoil behaves, focusing on understanding dynamic stall phenomena. The outline with corresponding dimensions of the NACA643418 airfoil with the corresponding pressure tap locations is given in Figure 3.1. Furthermore, the visual of the airfoil inside the wind tunnel has been given in Figure 3.2.

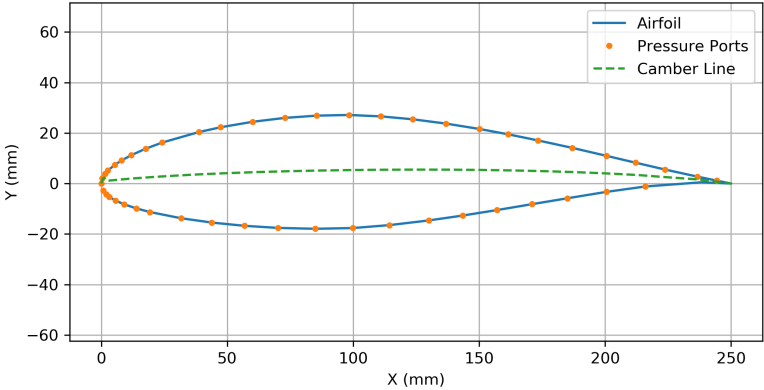


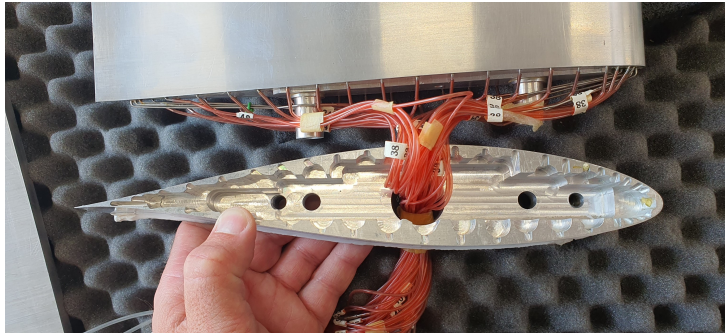
Figure 3.1: Visualization of the NACA643418 airfoil at a 0° angle of attack, highlighting the locations of pressure taps.



Figure 3.2: NACA643418 airfoil within the wind tunnel, depicted at a 50° angle of attack.

During static and dynamic testing, pressure ports are placed strategically to capture local pressure details. These transducers provide specific pressure readings that combine to create a comprehensive pressure map, revealing aerodynamic intricacies under static conditions. To measure the static pressure over the airfoil surface, 52 pressure orifices were placed strategically, with the location as already shown in Figure 3.1. There were 27 ports on the top side of the wing and 25 ports on the lower side. In the initial static testing phase, the aerodynamic profile is examined critically. During this phase, the model is firmly set at a specific angle of attack while the orifices are connected to pressure transducers, and data are collected at a rate of 300 Hertz. Each test case involves acquiring data for approximately

10 seconds. The figure below illustrates how the tubes in the model are connected to the pressure measurement device via connectors, as shown in Figure 3.3.



(a) Illustration of connection arrangements of the tubes for pressure taps.



(b) Connectors designed for interfacing the pressure tubes with the pressure reading device.¹

Figure 3.3: Comparison between connection tubes for pressure taps (a) and connectors for attaching pressure tubes to the pressure reading machine (b). Images provided by S. Bernardy.

Table 3.1: Dimensions of Pressure Measurements Components.

Component	Inner Diameter [mm]	Length [mm]
Tap	0.4	3
Steel Tube	0.7	450
Tube	0.8	220
Adapter	0.8	9
Tube	1	2000
Connector 1	0.65	6.6
Connector 2	0.9	21.1
Connector 3	0.95	6.9
Connector 4	0.65	20.15
Tube	1	500
Scanner	0.65	15

Dynamic testing is a method that goes beyond static investigations and involves incorporating sinusoidal pitching movements into the model. These movements replicate authentic oscillations on aerodynamic surfaces, with amplitudes of 5° , 10° , and 15° and frequencies ranging from 1 to 4 Hz. The combinations of amplitude and frequency are outlined in Table 3.2. It's important to note that both pressure measurements and PIV are conducted for static and dynamic measurements. This dual approach offers a vivid depiction of flow patterns around the dynamically moving model, which strives to simulate real-world scenarios authentically. This approach provides valuable insights by enabling a comprehensive exploration of fluid dynamics.

Table 3.2: A detailed presentation of configurations encompassing the dataset's various angles, amplitudes, and pitching frequencies.

Mean Angle [°]	Amplitude [°]	Pitching Frequency [Hz]
10	5	1, 2, 3, 4
	10	2, 3
	15	2, 3
40	5	1, 2, 3, 4
	10	2, 3
	15	2, 3
50	5	1, 2, 3, 4
	10	2, 3
	15	2, 3
90	5	1, 2, 3, 4
	10	2, 3
	15	2, 3
130	5	1, 2, 3, 4
	10	2, 3
	15	2, 3
160	5	1, 2, 3, 4
	10	2, 3
	15	2, 3
170	5	1, 2, 3, 4
	10	2, 3
	15	2, 3

To ascertain whether the default acquisition time of 5 seconds is adequate for computing the average pressure field in the Labview program for static cases, one must delve into the interplay between acquisition time (T), the Strouhal number (St), and flow characteristics. The number of cycles recorded in the flow hinges on various factors, encompassing the Strouhal number, flow velocity, and characteristic length scale of the flow (in this instance, the chord length), as elucidated in subsection 2.1.3. Typically, a higher vortex shedding frequency correlates with a larger Strouhal number, necessitating less time to capture flow features precisely. Given a Strouhal number range of 0.17-0.25, a wind speed (U_∞) of 15 m/s, and a chord length (here L_c) of 0.25 m, the shedding frequency (f_s) can be determined using the formula:

$$f = St \cdot (U_\infty / L_c) \quad \text{and} \quad N_{cycles} = f_s \cdot T \quad (3.1)$$

Table 3.3: Estimated number of vortex shed cycles captured within 5 seconds for varying Strouhal numbers (St) and wind speeds, demonstrating the sufficiency of acquisition time for static cases in LabVIEW.

Estimation	Low	Medium	High
St [-]	0.17	0.21	0.25
Wind Speed [m/s]	15	15	15
Measurement Time [s]	5	5	5
Estimated Cycles	51	63	75

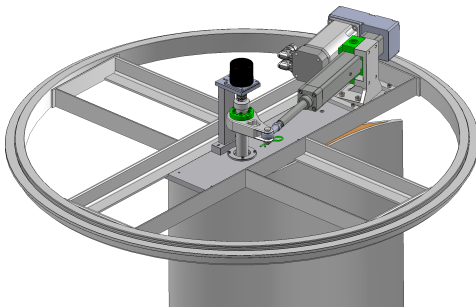
This computation reveals that with data collected over 5 seconds, between 51 and 75 vortex shed cycles will be captured when measuring at a frequency of 300 Hz. This volume of data is deemed sufficient to determine if the shed vortices are adequately captured. Moreover, it is viable to compute an average of the mean for these vortices using the collected data.

The reduced frequency induced in the flow by the pitching of the airfoil depends, as explained in subsection 2.1.4, on the pitching frequency, chord, and wind speed. Since the exact wind speed is unknown and varies for different α , it is possible to derive the wind speed value from the Reynolds number. This will provide the induced frequency values and clearly understand which cases are considered quasi-steady and which involve fully unsteady aerodynamics. The values used for these calculations are based on the normal conditions inside the wind tunnel facility. This results in an air temperature of 21°C , an air density of 1.205 kg/m^3 , and a dynamic viscosity of $1.83 \times 10^{-5}\text{ kg/(m}\cdot\text{s)}$. The values are calculated and presented in Table 3.4. Additionally, according to subsection 2.1.4, it is noted that the aerodynamics are quasi-steady for $0 \leq k \leq 0.05$, whereas this research specifically requires the fully unsteady regime. In the table, it is shown that the values for $f_{pitching} = 1$ at Reynolds number of $250k$ and $f_{pitching} = 1, 2$ at $500k$ are at or below the boundary of fully unsteady aerodynamics.

Table 3.4: Induced frequency values for different frequency cases.

$f_{pitching}$ [Hz]	$k(Re = 150k)$	$k(Re = 250k)$	$k(Re = 500k)$
1	0.086	0.051	0.026
2	0.17	0.10	0.052
3	0.26	0.16	0.078
4	0.34	0.21	0.10

The actuator system used during dynamic testing to adjust the pitch of the airfoil involves several critical components. The most significant component of this entire system is the PNCE-40-BS-1610-200-S linear actuator from Unimotion, which provides precise and controlled movement. It works alongside the Sangalli servo motor DSM5.32.1146.98, which converts electrical signals into mechanical motion. The LinUDP servo controller C 1450-LU-VS-1S-000 coordinates and controls the operation. An Elap encoder REV621 C 36000 5/28 R 8 PP 2 accurately measures the pitch angle. This specific component is designed to work alongside the NI cRIO-9053 CompactRIO system and NI-9401 module to provide accurate pitch angle measurements. These components work together to precisely adjust the airfoil's pitch, which is crucial for conducting detailed experiments and analyses in aeronautical research. Figure 3.4 shows the CAD version and the real-life picture of the actuator setup, providing a clear view of the integration and utilization of the components in the system.



(a) Schematic representation of the actuator system.



(b) Photograph of the actual actuator setup.

Figure 3.4: Comparison between the schematic diagram (a) and the actual setup (b) of the actuator system. The schematic diagram illustrates the theoretical arrangement and components involved, while the photograph depicts the physical implementation of the system. Provided by S. Bernardy.

3.2. PIV Setup and Calibration

Tools play a crucial role in transitioning to the PIV phase of the experiment. To create the desired atmosphere inside the tunnel, a SAFEX smoke generator was utilized to produce water-glycol droplets with a median diameter of $1\ \mu\text{m}$. These tiny droplets were then dispersed into the tunnel, filling the space with their misty presence. The effect allowed the laser to illuminate these particles from both sides of the airfoil. Two EverGreen² lasers, *EverGreen² (70-200 mJ @ 532 nm) - Quantel (2023)*, a dual-pulsed laser designed for PIV applications, are used. It offers customizable pulse energies—

choose from 70 mJ, 145 mJ, or 200 mJ at 15 Hz, creating a thin laser sheet of roughly 2 mm . This laser system, comprising a single laser head and power supply, illuminates particles into the flowing medium, working with laser light to visually capture the evolving vortical structures.

The sCMOS camera by GmbH (2023) enhances the process further. Featuring a scientific sCMOS sensor, this camera combines modern CCD and CMOS technologies, ensuring image quality and system performance. The sCMOS camera, equipped with 50 mm Nikon lenses, is an essential tool for extracting velocity vectors during data processing. It provides high-quality imaging with 5.5 million pixels, low readout noise, and a frame rate of 50 Hz at full resolution. Its CameraLink HS interface adds to the efficiency by enabling data throughput over extended distances. The suggested setup, covering both the test section and the PIV arrangement, is depicted in Figure 3.5 with a schematic view of the set up given in Figure 3.6.

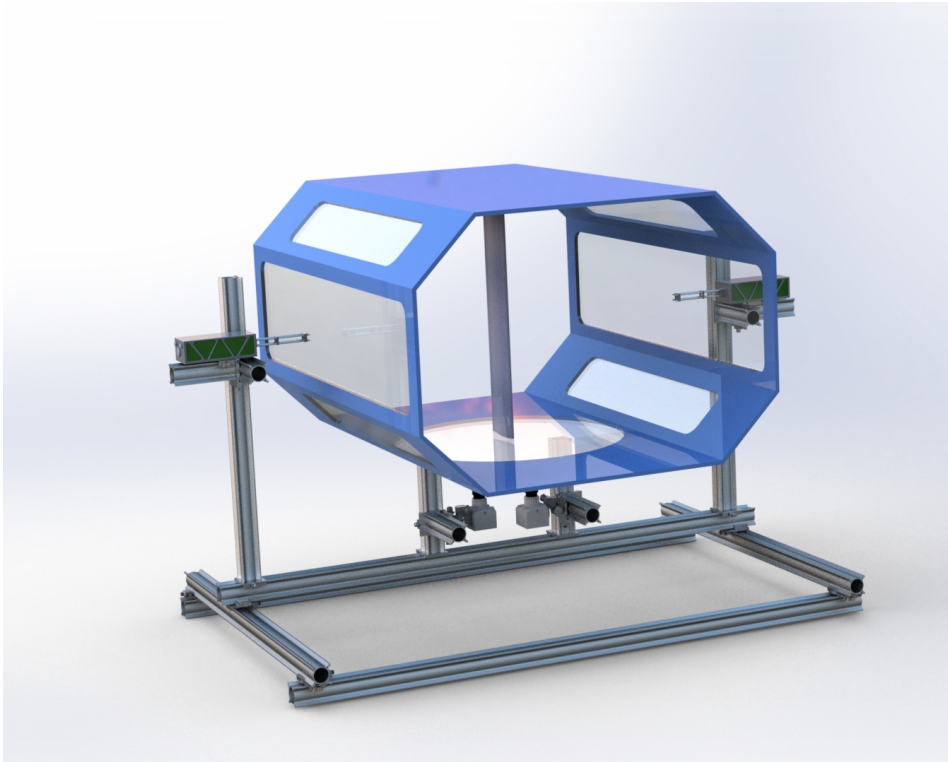


Figure 3.5: CAD image of the wind tunnel configuration featuring the NACA643418 airfoil at a 0° angle of attack, showcasing the blue-coloured test section. The PIV setup is shown alongside the test section with the Evergreen lasers, and sCMOS cameras positioned underneath the test section.

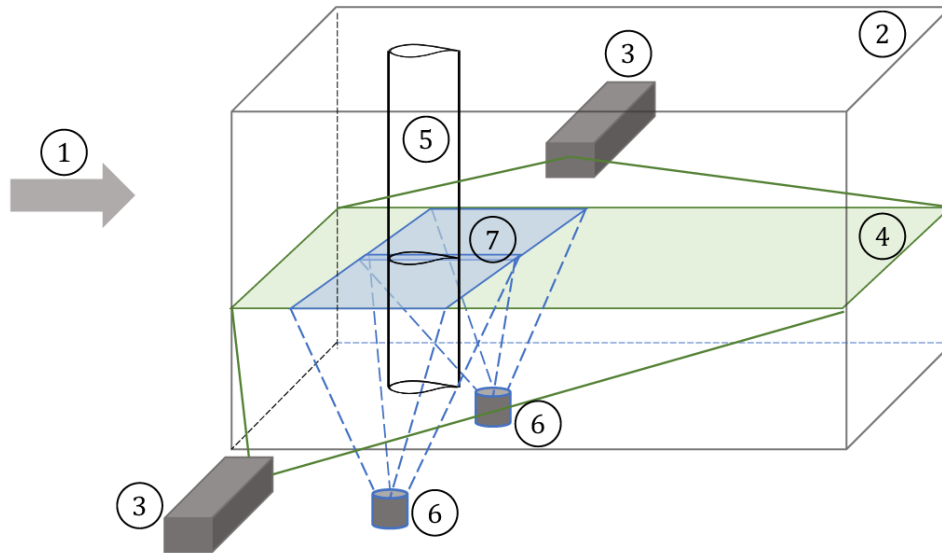
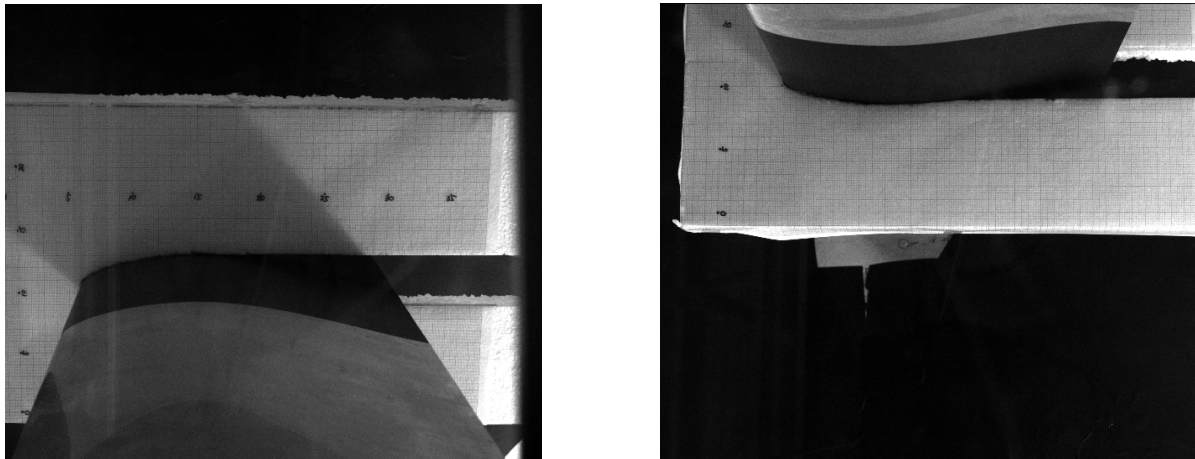


Figure 3.6: Schematic plot of the PIV measurement setup. The components of the measurement are: ①: incoming wind ②: test section ③: laser ④:illumination plane ⑤: airfoil model ⑥: camera ⑦: camera view.

Calibrating a PIV setup involving two cameras and two lasers is a critical step to ensure accurate velocity measurements in fluid dynamics studies. The calibration process aligns the cameras and lasers with the flow field and establishes a relationship between the pixel coordinates in the camera images and the physical coordinates in the measurement volume. The use of a calibration plate, featuring a millimeter grid of known dimensions, is essential for this process. While specific steps can vary depending on the PIV system and software, the following description outlines the used approach to calibration using the Davis Software, a widely used platform for PIV data analysis.

Firstly, the calibration plate made from a Styrofoam plate is positioned within the test section where the flow measurements will be taken. It's crucial that the plate is aligned perpendicular to the laser sheet and that the entire grid can be captured by both cameras. Another important aspect is that both cameras should see the a common point on the grid. This setup ensures that the calibration accounts for the stereoscopic arrangement necessary for two-dimensional velocity measurements.

The next step involves capturing images of the calibration plate with both cameras. The settings of the lenses involved in the calibration were two 2x35mm Nikon lenses. These lenses were initially calibrated at an f-stop of 5.6, but the real measurement was taken at an f-stop of 8. The Davis Software uses these images to compute the transformation between the camera's pixel coordinates and the physical space coordinates. It's essential to capture images from various angles and positions by slightly adjusting the calibration plate's orientation and position. This variability enhances the calibration's robustness and accuracy. The two pictures taken for calibration are shown in Figure 3.7.



(a) Upper side of the airfoil.

(b) Lower side of the airfoil.

Figure 3.7: Figures showing the upper and lower side of an airfoil with a calibration plate.

After capturing the necessary images, the Davis Software processes the images to identify the grid points on the calibration plate. The software then uses these points to compute the calibration parameters, including the position and orientation of the cameras and lasers relative to the measurement plane. This step may involve iterative optimization to minimize the error between the known grid positions and the positions measured by the PIV system. The calibration process also includes adjusting the lasers to ensure that the laser sheets intersect the plane of interest accurately and uniformly illuminate the particles within the flow. Proper alignment of the lasers is crucial for capturing high-quality images with well-defined particle images.

Finally, a validation step is performed to verify the calibration's accuracy. This step involved capturing images of a known flow of 15 m/s around the 0° angle of attack position to check the wind speed away from the airfoil. The validation ensures that the PIV setup accurately measures velocities throughout the measurement plane.

The settings for PIV computations in Davis Software are crucial for ensuring accurate and efficient analysis of fluid flows. The initial step in the PIV image computation process involves applying a Time-series Subtract time filter, which is essential for enhancing the quality of the images by reducing noise and brightness from reflective surfaces and improving the visibility of the particles. This preprocessing step is critical for preparing the images for subsequent analysis and ensuring that the PIV computation can be performed effectively.

Following the preprocessing, the PIV computation with three final passes, utilizing a window size of 32×32 pixels and a 75% overlap, is performed. This specific window size and overlap percentage are selected to optimize the balance between spatial resolution and measurement accuracy. The choice of window size directly impacts the spatial resolution of the velocity field, with smaller windows allowing for higher resolution but potentially increasing noise. Conversely, larger windows may reduce noise but at the cost of spatial resolution. The 75% overlap is used to increase the amount of velocity information obtained from the images, enhancing the accuracy of the velocity field measurements. This high overlap ensures that each particle's movement is captured multiple times, providing a more detailed and accurate representation of the flow field.

3.3. Component list

This subsection presents a comprehensive list of the most vital components utilized to conduct the tests, excluding the wind tunnel and the airfoil model itself. In Table 3.5 the components are given. This list encompasses all essential items required to ensure accurate and reliable test results. Each component plays a critical role in the experimental setup, contributing to the precise measurement and analysis of aerodynamic properties. The detailed enumeration of these items serves as a reference for replicating the experiments and understanding the full scope of the equipment involved.

Item	Description	Quantity
Actuator	Linear actuator for controlling pitching movement of the blade section by Unimotion. Model PNCE-40-BS-1610-200-S	1
Aluminium Tape	Adhesive tape made of aluminium for sealing gaps and smoothening surfaces.	1
Angular Encoder	Device for reading angular information by Elap. Model REV621 C 36000 5/28 R 8 PP 2. In combination with a NI cRIO-9053 CompactRIO system with a NI-9401 module	1
Labview Programs	Software programs developed using LabVIEW by S. Bernardy.	1
LaVision DaVis 10.2	PIV software for flow visualization and analysis.	1
Laser Protection Goggles	Protective eyewear shielding eyes from laser light.	4
Millimeter Paper	Paper with a millimetre grid for accurate PIV setup calibration.	1
NACA643418 Model	NACA-developed 6-digit airfoil with 250mm chord.	1
Nikon Lenses	Optical lenses by Nikon for cameras with 35mm focal length.	2
PTU X Timing Unit	Timing unit for synchronizing measurement starting point.	1
Quantel Evergreen ²	Laser system for PIV applications.	2
SAFEX Smoke Generator	Device for generating smoke safely with fine particle size.	1
sCMOS Camera	High-performance scientific camera for PIV applications.	2
Styrofoam	Lightweight foam for creating calibration plate.	1
Servo Motor	Motor to drive the linear actuator by Sangalli. Model DSM5.32.1146.98	1
Servo Controller	Controller by LinUDP to steer the motor accordingly. Model C 1450-LU-VS-1S-000.	1
Wind Rake	Instrument for measuring wind characteristics.	1
X-Beams	Aluminium X-profiled beams for sturdy setup support. In lengths 3000, 2000, 1000, 300 and 200 <i>mm</i>	25

Table 3.5: Comprehensive list of components used in the experimental setup.

4

Results and Discussion

4.1. Reynolds Number Study

The analysis of lift coefficient curves across a range of angles of attack from 0° to 180° for the airfoil provides valuable insights into the effect of varying Reynolds numbers on aerodynamic performance. Clear patterns emerge by comparing the behaviour of C_l at Reynolds numbers of $80k$, $150k$, $250k$, $500k$, $700k$, and $1000k$, revealing the influence of Reynolds number on lift generation and stall characteristics. These values are depicted in Figure 4.1. The values for the $1000k$ only go up to an angle of attack of 44° . Beyond this point, there was too much vibration in the wind tunnel at high wind speeds, making it unfeasible to continue testing.

The lift coefficient curve at $Re = 80k$ is notably distinct from higher Reynolds number curves. This discrepancy arises due to the relatively higher viscosity of air at this Reynolds number. As a result, the air is more adhesive, leading to a higher maximum lift coefficient ($C_{l_{max}}$) and elevated lift coefficients within the α range of 20° to 80° . The elevated C_l values in this range indicate increased lift generation potential at these angles of attack compared to higher Reynolds number regimes.

The lift coefficient curve at $Re = 150k$ exhibits intermediate characteristics, positioned between the low and high Reynolds number curves. Notably, it achieves a higher $C_{l_{max}}$ at a lower α compared to the higher Reynolds number curves. Additionally, it can be observed that there is a small deviation in the measured lift in the α range of 40° to 60° compared to higher Reynolds number regimes, but this is not considered significant. These observations suggest a transition towards relatively reduced air viscosity effects.

For Reynolds numbers $Re = 500k$, $700k$, and $1000k$, the lift coefficient curves exhibit close alignment, particularly outside the stall regime. This convergence indicates the minimal influence of Reynolds number variations on lift characteristics beyond $Re = 500k$. The consistency in C_l values suggests that aerodynamic performance stabilizes at higher Reynolds numbers, with differences primarily observed in stall characteristics.

The stall phenomenon, characterized by a sudden decrease in lift and increase in drag, exhibits notable Reynolds number dependency. Specifically, higher Reynolds numbers delay stall onset and alter stall characteristics. As the Reynolds number increases, stall onset is delayed, resulting in sustained lift production at higher angles of attack. This delay is attributed to Reynolds number effects, wherein increased airflow smoothens flow separation, thus postponing the stall occurrence.

The lift coefficient curve at $Re = 250k$ closely aligns with higher Reynolds number curves, exhibiting minimal deviations, particularly in the deep stall regime. This observation suggests that $Re = 250k$ represents a critical threshold wherein aerodynamic performance resembles that of higher Reynolds number regimes. Consequently, $Re = 250k$ is identified as the optimal Reynolds number for further testing. This selection balances the testing environment's capabilities, allowing for easier pitching due to reduced forces acting on the airfoil, with the need for accurate aerodynamic behaviour representation, particularly in the deep stall regime.

Overall, the comparative analysis of lift coefficient curves across various angles of attack and Reynolds numbers elucidates significant trends in aerodynamic performance. The results underscore the influence of Reynolds number variations on lift generation, stall characteristics, and overall aerody-

dynamic behaviour. Notably, higher Reynolds numbers mitigate viscosity effects, leading to consistent lift characteristics and delayed stall onset.

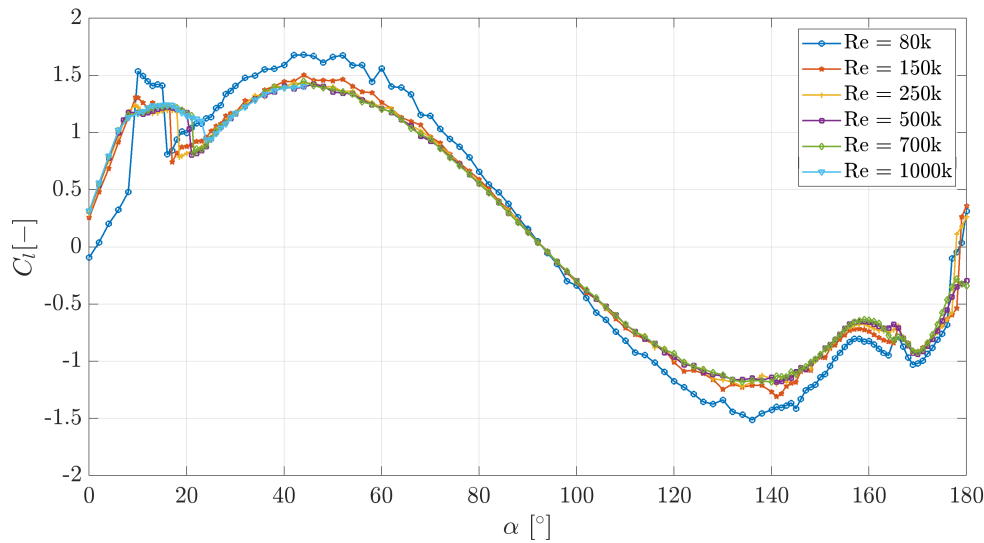


Figure 4.1: Comparison study of C_l values for different Reynolds numbers.

The drag coefficient curves for the Reynolds numbers of $80k$, $150k$, $250k$, $500k$, $700k$, and $1000k$, again show similar conclusion as the lift coefficient curves. The drag coefficient curves are depicted in Figure 4.2.

The drag coefficient curve at $Re = 80k$ consistently exhibits higher values for all angles of attack, indicative of increased aerodynamic drag. This observation aligns with the relatively higher viscosity of air at this Reynolds number, resulting in greater frictional forces and turbulence, thereby elevating drag coefficients across all α values.

The drag coefficient curve at $Re = 150k$ demonstrates a tendency to converge towards higher Reynolds number curves, albeit remaining slightly elevated. Particularly within the α range of 40 to 90° , the drag coefficients tend to surpass those of higher Reynolds number regimes. This deviation suggests lingering effects of air viscosity at $Re = 150k$, contributing to elevated drag coefficients, especially at extreme angles of attack.

For Reynolds numbers $Re = 250k$ to $Re = 1000k$, the drag coefficient curves appear to converge closely, with negligible deviations observed. This convergence indicates that beyond $Re = 250k$, Reynolds number variations have minimal impact on drag characteristics, emphasizing the stabilization of aerodynamic performance at higher Reynolds numbers. The disparities in drag coefficients primarily manifest in the stall regime, where the delay in stall onset influences the magnitude of the drag jump.

The stall-induced drag, characterized by a sudden increase in drag accompanying stall onset, exhibits Reynolds number dependency. Higher Reynolds numbers delay stall occurrence, thereby postponing the abrupt increase in drag. Consequently, the magnitude of the drag jump in the stall regime is directly influenced by the Reynolds number, with higher Reynolds numbers leading to more gradual increases in drag.

The drag coefficient curve at $Re = 250k$ demonstrates significant convergence, particularly in the deep stall regime, indicating minimal deviations from higher Reynolds number values. This convergence, along with the convergence observed in Figure 4.1, indicates that $Re = 250k$ is an appropriate benchmark for further testing. It effectively balances the need for efficient testing with the importance of accurately capturing aerodynamic phenomena.

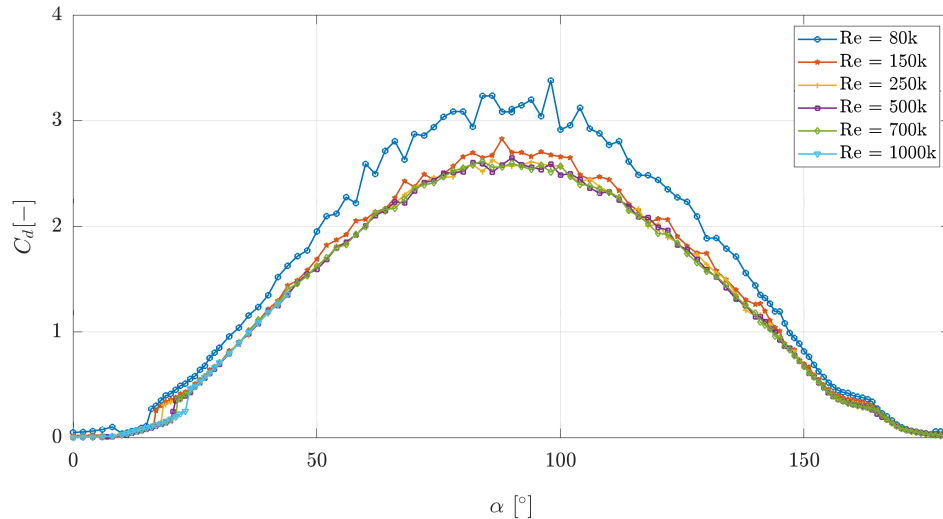


Figure 4.2: Comparison study of C_d values for different Reynolds numbers.

4.2. Actuator

The investigation sought to assess the performance of an actuator in pitching angles against ideal sine waves across varying conditions. Four distinct cases were analyzed, each characterized by different mean angles of attack, frequencies, and amplitudes. Results were evaluated through the examination of single-sided amplitude spectrum graphs and by fitting sine waves to measured angle signals.

In the first case, depicted in Figure 4.3, where the mean α was set at 10° , frequency at 1 Hz and amplitude at 5° , the actuator exhibited behaviour closely resembling the ideal sine wave. Notably, the single-sided amplitude spectrum graph depicted an identical pattern between the measured signal and the ideal sine wave.

Transitioning to the second case, with a mean α of 40° , frequency of 2 Hz, and amplitude of 5° , the actuator's performance is closely aligned with the ideal sine wave. Similar to case 1, the single-sided amplitude spectrum graph indicated a consistent pattern between the measured signal and the ideal sine wave. As can be seen in Figure 4.4. Nevertheless, the propensity for over- or undershooting at higher amplitudes persisted, indicating that the precision deviates from a perfect sine wave. However, this difference remains within 1%.

In the third case, featuring a mean α of 10° , frequency of 3 Hz, and amplitude of 10° , the actuator's behaviour remained consistent with the specified frequency. As the single-sided amplitude spectrum is again aligned, shown in Figure 4.5. However, a more pronounced overshooting tendency was observed as the frequency and amplitude increased. This observation underscores the correlation between the higher energy the actuator has to deliver and the tendency to overshoot at the peaks. However, the inaccuracy seems to be within operating accuracy as it only overshoots the peak at maximum with an amplitude of 0.0625° on a case with an amplitude of 10° .

Finally, in Figure 4.6 case 4 is shown. This involves a mean α of 40° , frequency of 4 Hz, and amplitude of 5° . Despite the higher frequency, the actuator demonstrated fidelity to the specified frequency.

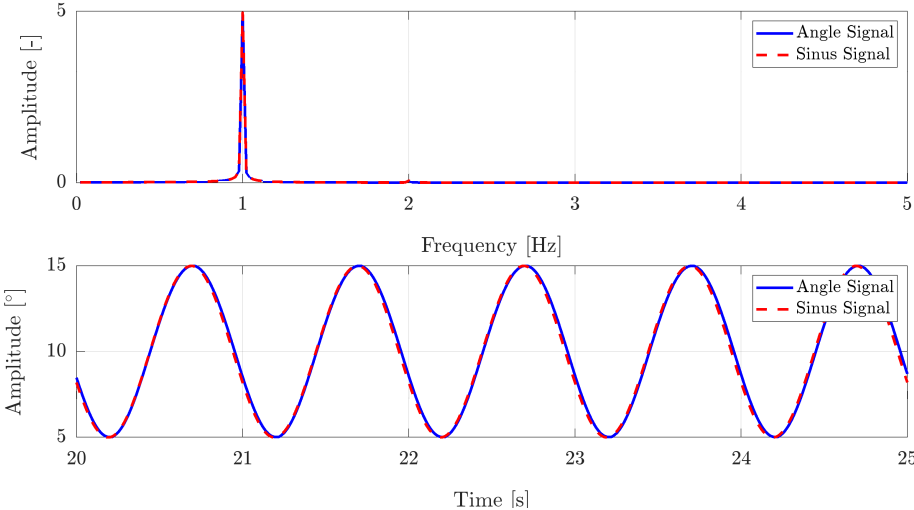


Figure 4.3: Single-sided FFT amplitude spectrum and real angle data for both the measured signal and a perfect sinusoidal signal at $\alpha_{\text{mean}} = 10^\circ$, $f_{\text{pitching}} = 1\text{Hz}$, and $A_{\text{pitching}} = 5^\circ$.

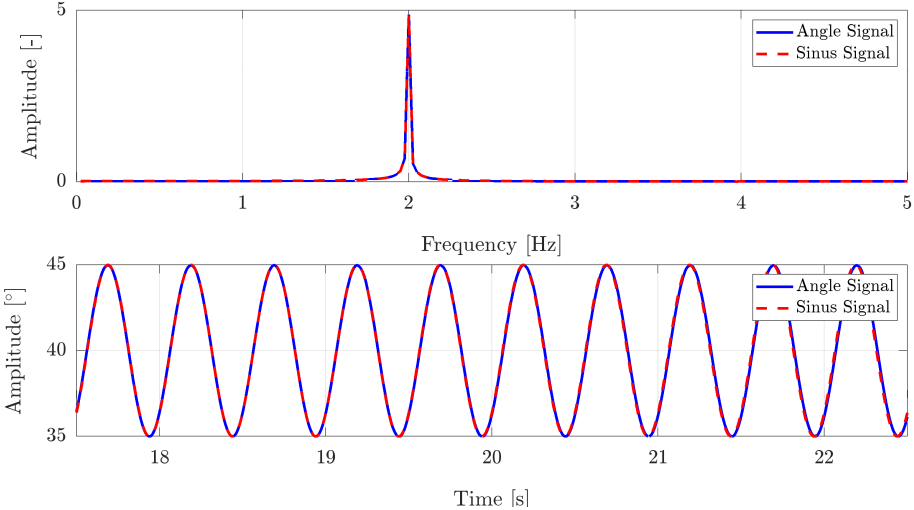


Figure 4.4: Single-sided FFT amplitude spectrum and real angle data for both the measured signal and a perfect sinusoidal signal at $\alpha_{\text{mean}} = 40^\circ$, $f_{\text{pitching}} = 2\text{Hz}$, and $A_{\text{pitching}} = 5^\circ$.

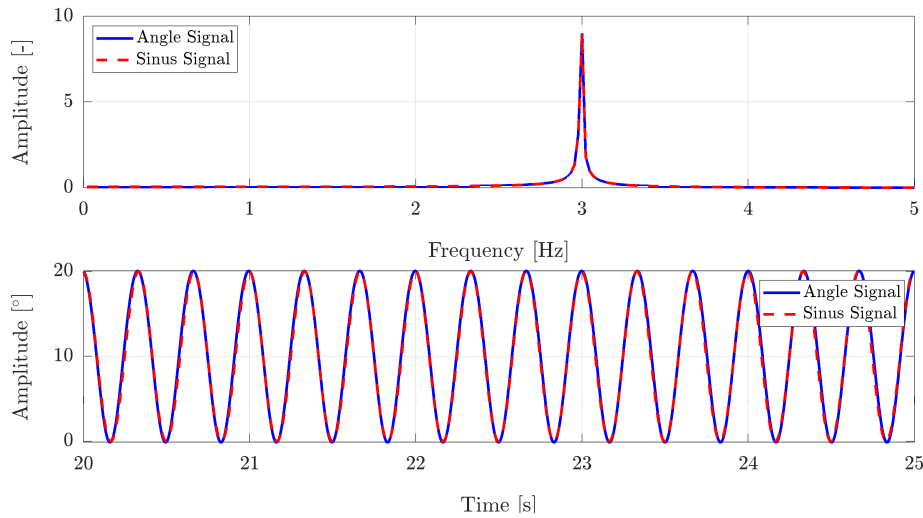


Figure 4.5: Single-sided FFT amplitude spectrum and real angle data for both the measured signal and a perfect sinusoidal signal at $\alpha_{\text{mean}} = 10^\circ$, $f_{\text{pitching}} = 3\text{Hz}$, and $A_{\text{pitching}} = 10^\circ$.

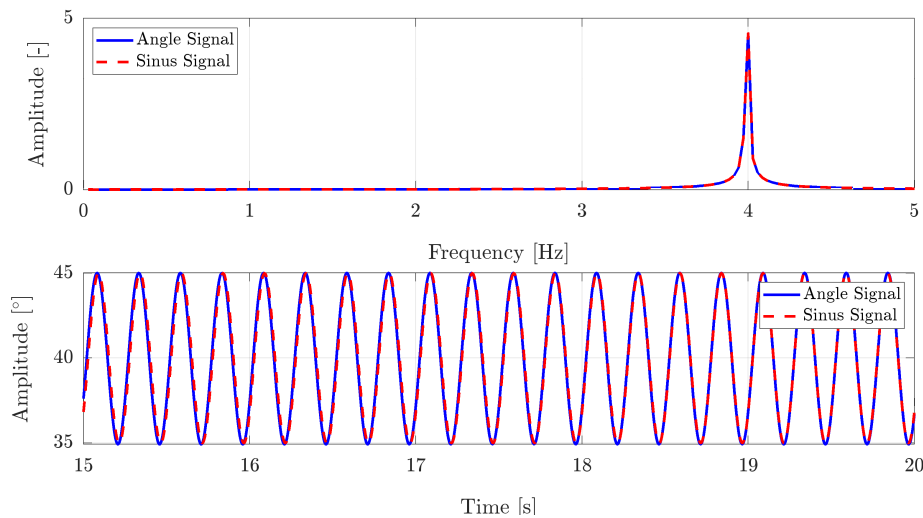


Figure 4.6: Single-sided FFT amplitude spectrum and real angle data for both the measured signal and a perfect sinusoidal signal at $\alpha_{\text{mean}} = 40^\circ$, $f_{\text{pitching}} = 4\text{Hz}$, and $A_{\text{pitching}} = 5^\circ$.

In addition to the single-sided amplitude spectrum analysis, fitting a perfect sine wave over the measured angle signal provided further insights. Across all cases, a slight lag was observed as more cycles progressed. The data recorded by the angular encoder during pressure tests for six cases were investigated. The analysis focused on the shift in pitching from the encoder readings compared to a perfect sine wave. These values are shown in Table 4.1. The actuator demonstrates consistency in controlling the specified frequencies across different cases. Despite variations in angle of attack and frequency, the measured frequencies closely match the specified values. This indicates that the actuator effectively maintains the desired pitching mechanism frequency.

The data shows a small decrease in performance as more cycles occur. This decrease is consistently observed in all instances. However, the difference is minimal and does not have a significant impact on the accuracy of the measurements. It indicates that there may be a slight delay or inertia effect within the actuator system, which becomes more noticeable over successive cycles but stays within acceptable limits.

The actuator shows signs of overshooting, as seen in the measured shift values that sometimes exceed the expected values. However, the actuator consistently meets the specified frequencies. This

indicates that although there may be temporary overshooting when the actuator responds to input commands, it ultimately stabilizes and maintains the desired frequency.

The actuator's consistent adherence to specified frequencies and minimal impact of lag or overshooting on measurement accuracy highlights its reliability in controlling the pitching mechanism, crucial for ensuring stable and predictable performance in various operational scenarios. Furthermore, the average values and standard deviations provided in the table offer a summary of the actuator's overall performance across the tested cases.

Table 4.1: Performance metrics of the actuator in controlling pitching mechanism.

α [°]	f_{pitch} [Hz]	A_{pitch} [°]	Meas. Shift [s]	Cycles [-]	Run Time [s]	Shift/Cycle [10^{-3} s]	Time Error [%]
40	1	15	0.05	40	40.0	1.3	0.12
10	1	5	0.06	40	40.0	1.5	0.15
40	2	5	0.06	78	39.0	0.77	0.15
40	2	15	0.0667	86	43.0	0.78	0.16
10	3	10	0.0566	100	33.3	0.57	0.17
40	4	5	0.0534	120	30.0	0.45	0.18
50	3	5	0.0833	132	44.0	0.63	0.19
Average						0.85	0.16
Std						0.34	

4.3. Static Cases

This section examines static cases within the study, focusing on fundamental aerodynamic parameters such as drag, lift, and pressure coefficient. In addition, PIV images are analyzed to visualize flow patterns around the object. The goal is to enhance our understanding of aerodynamic behaviour by carefully analyzing these specific cases. This analysis will focus on addressing the first two research questions, which are related to the flow field around the airfoil and the forces acting on it during deep stall.

4.3.1. Drag Coefficient

The analysis of the uncorrected versus corrected drag coefficient curves across a range of angles of attack from 0° to 180° , for Reynolds numbers $150k$, $250k$, $500k$, and $700k$, provides valuable insights into the effectiveness of correction methods and the behaviour of aerodynamic coefficients under varying conditions.

The corrections applied to the drag coefficient values show clear patterns across different angles of attack. Notably, the Allen method is primarily effective for angles up to 20° . In comparison, the Maskell method is more suitable for angles beyond 20° , as discussed in subsection 2.4.3. This division of correction methods suggests a tailored approach to address the complexities of aerodynamic behaviour at different α . The need for a transition between correction methods reflects the intricate interplay between flow regimes and the applicability of correction algorithms.

A key observation is the correlation between the magnitude of drag coefficient correction and the measured drag coefficient values. Specifically, regions where the measured drag coefficient is lower correspond to lesser correction, while higher drag coefficient values undergo more substantial correction. This can be seen in all 4 cases in Figure 4.7. This phenomenon is particularly evident in the α range of 50° - 130° , where the highest drag coefficients are recorded. The underlying rationale can be traced back to the nature of the correction equations, wherein deviations from ideal behaviour result in greater correction efforts. Equation 2.64 underscores this relationship, indicating that discrepancies between real and measured drag coefficients lead to variations in the correction ratio. Consequently, as the measured drag coefficient increases, the correction factor diverges from the value of one, necessitating more extensive correction.

The Allen method correction range demonstrates proper results in correcting drag coefficient values. This result is reasonable, as smaller angles of attack typically show less variation between the measured and actual C_d values. Therefore, the corrective modifications made by the Allen method

are proportional to the level of correction needed, demonstrating its effectiveness in addressing minor discrepancies in C_d values at lower angles of attack.

The trend observed, showing greater correction at higher drag coefficients, aligns with established principles of wind tunnel correction methods. Higher drag coefficients indicate increased aerodynamic resistance, leading to larger wake areas and augmented flow disturbances. Consequently, the presence of walls in wind tunnel testing necessitates additional correction to account for the influence of boundary effects. The amplified correction observed at higher drag coefficients reflects the intensified aerodynamic complexities induced by flow separation and wake formation, affirming the relevance of wind tunnel correction principles.

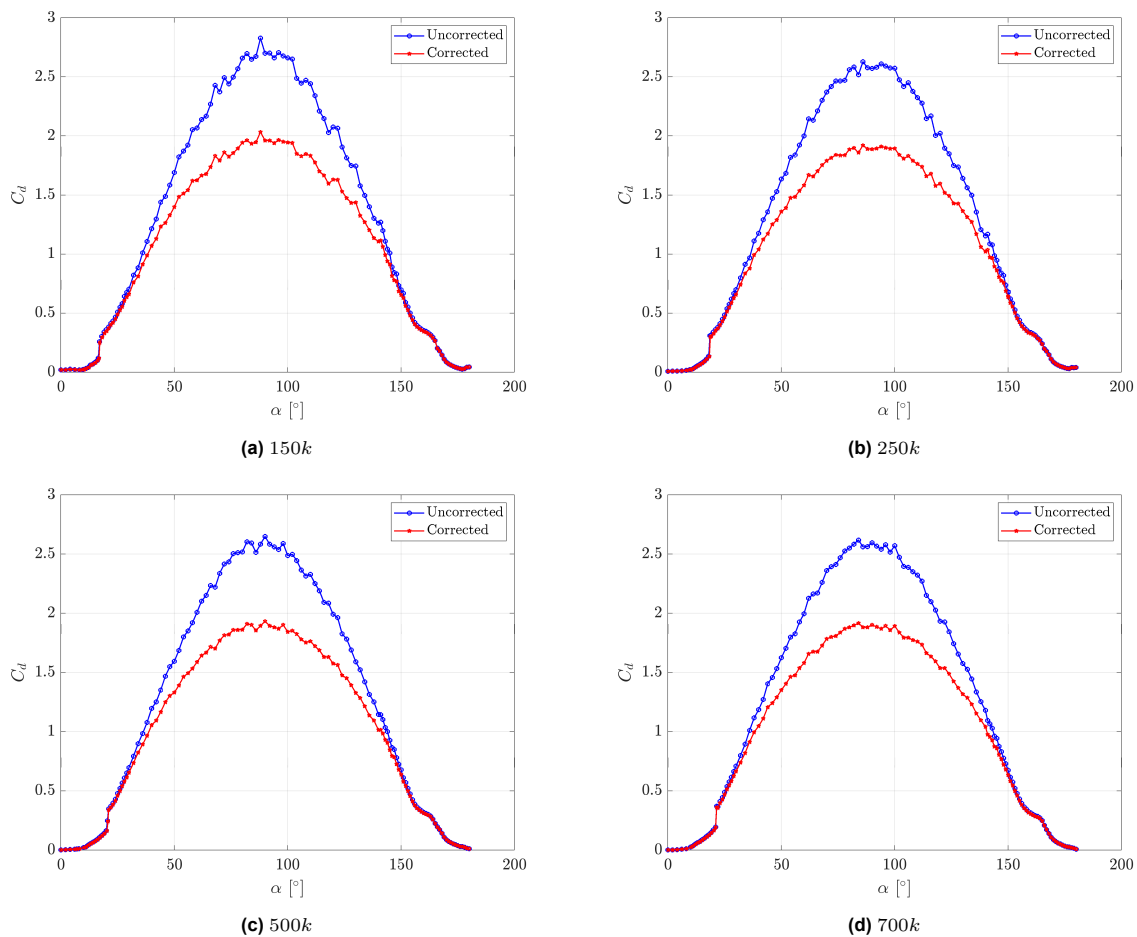


Figure 4.7: Comparison of uncorrected and corrected C_d values using combined Allen (0° to 20°) and Maskell (21° to 180°) wind tunnel corrections at different Reynolds numbers.

The findings from the study in section 4.1 regarding the appropriate choice of Reynolds number for dynamic testing are further supported by the corrected values of the drag coefficient for different Reynolds numbers. These values are shown in Figure 4.8. Upon closer examination, it becomes evident that the corrected values for the $150k$ Reynolds number do not align completely with the higher $500k$ and $700k$ curves, unlike the $250k$ curve. This discrepancy may indicate a distinct aerodynamic behaviour at the $150k$ Reynolds number. Additionally, the graph also illustrates the previously discussed delay in the stall regime, providing further evidence for the importance of Reynolds number selection in dynamic testing.

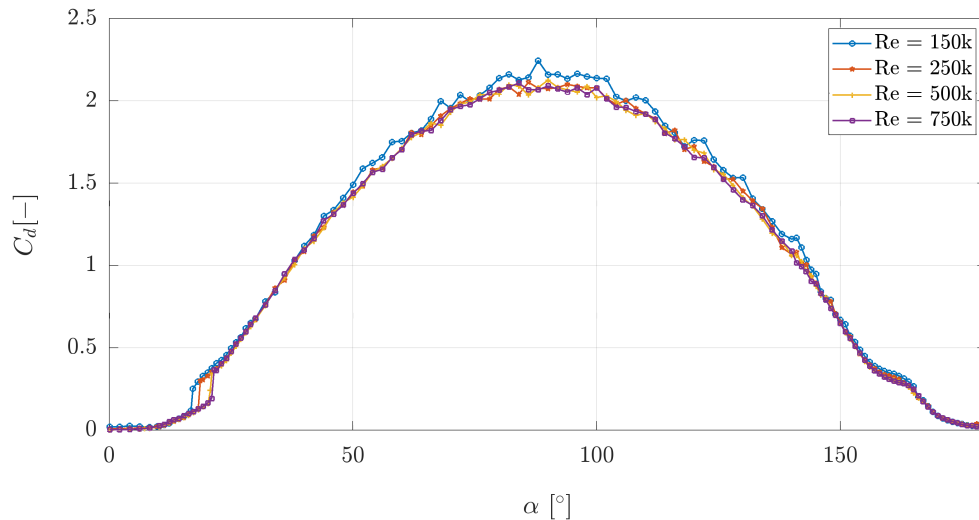


Figure 4.8: Comparison of corrected C_d values using combined Allen (0° to 20°) and Maskell (21° to 180°) wind tunnel corrections for different Reynolds numbers.

4.3.2. Lift Coefficient

The analysis of uncorrected versus corrected lift coefficient (C_l) curves for angles of attack ranging from 0° to 180° across different Reynolds numbers provides valuable insights into the aerodynamic behaviour of the airfoil. The results unveil several noteworthy findings, shedding light on stall regimes, the efficacy of correction methods, and the consistency of corrected values with expected trends. The results of both the uncorrected and corrected values from both the Allen and the Maskell methods for the four different Reynolds numbers are shown in Figure 4.9.

The observed stall regime, characterized by a sudden drop in C_l , suggests a probable combined stall mode contributing to full separation. This phenomenon is likely attributed to the simultaneous occurrence of leading-edge stall and trailing-edge stall. The presence of a small kink in the C_l curve preceding the abrupt drop, particularly evident in the α range of 10° - 18° , supports this hypothesis. Such deviations in the C_l curve are unlikely to occur in isolation but rather indicate the coalescence of multiple stall mechanisms. The suggested combination of leading-edge and trailing-edge stall is indicative of a complex aerodynamic interaction, possibly involving the bursting of a separation bubble near the airfoil's leading edge coupled with the onset of trailing-edge separation. This dual-stall mode culminates in a drastic reduction in lift coefficient, consistent with the observed behaviour in the deep stall regime. The exact combination will become evident when analysing the pressure coefficient plot for different angles in subsection 4.3.3.

Furthermore, the corrected lift coefficient curves exhibit significant alterations, particularly in the deep stall regime. This indicates the necessity of correction methods for accurately analyzing aerodynamic behaviour, especially in regions where flow separation is pronounced. The corrections applied seem to effectively capture the underlying aerodynamic phenomena, yielding values that align with theoretical expectations. Notably, the corrected values exhibit a logical progression, displaying a reduction compared to the measured values at higher angles of attack while maintaining coherence with the zero point of lift coefficient at similar locations as the measured values.

Moreover, the analysis again points out the correlation between correction magnitudes and angle of attack, with the angles closest to 90° s exhibiting more pronounced corrections. This trend can be attributed to the inherent workings of the correction method, which is based on the C_d , as again shown in Equation 2.64. As the angle of attack comes closest to the maximum drag, the influence of drag becomes more significant, thereby necessitating larger corrections to reconcile discrepancies between measured and theoretical values of the lift coefficient.

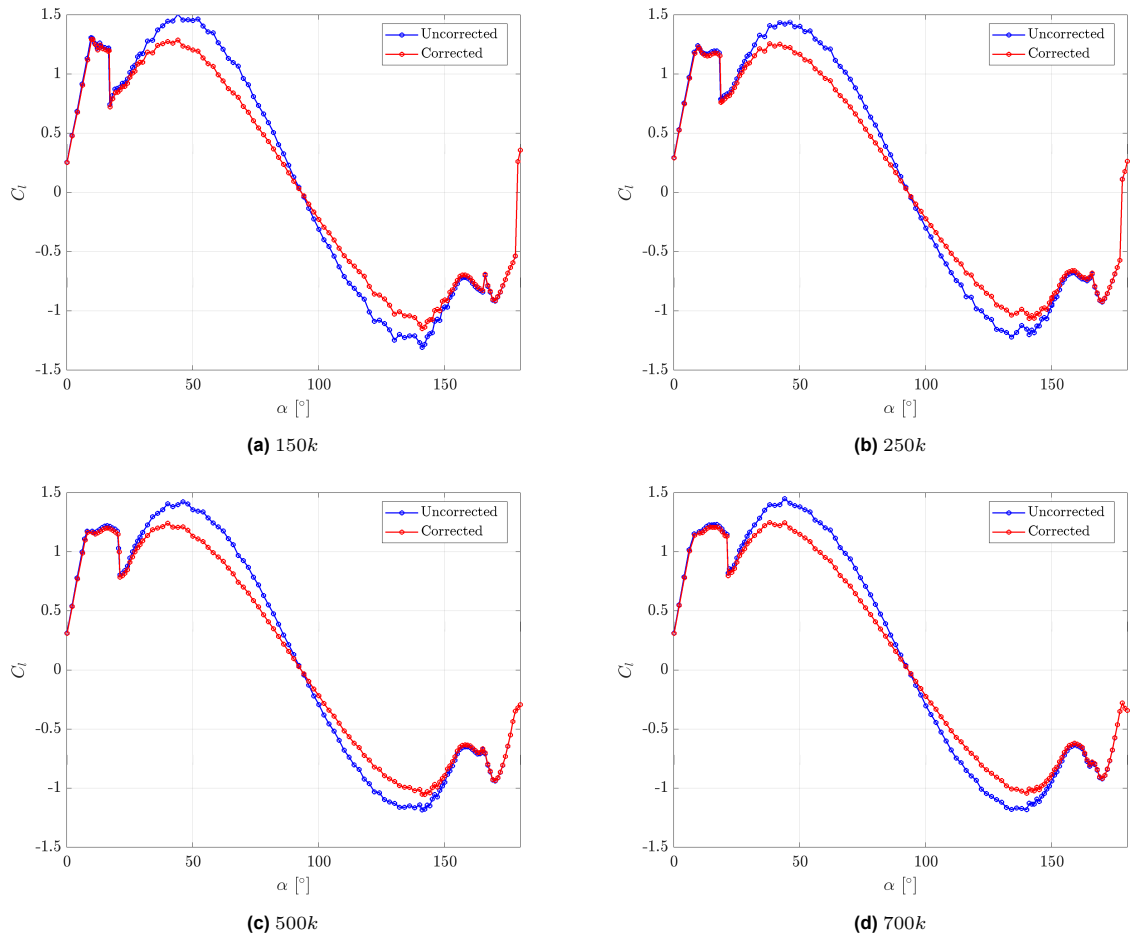


Figure 4.9: Comparison of uncorrected and corrected C_l values using combined Allen (0° to 20°) and Maskell (21° to 180°) wind tunnel corrections at different wind speeds.

The graph displaying the corrected C_l values for different Reynolds numbers in Figure 4.10 reveals two main findings. Firstly, the shape of the graph just before the stall is noteworthy. It is observed that as the Reynolds number increases, the curve between 10° and 18° becomes rounder, and the small peak at 10° becomes less prominent. This is likely due to the effect of Reynolds number on stall, as explained in section 4.1. Furthermore, the same conclusion from previous sections applies to the value of the Reynolds number, which is significantly similar to the larger Reynolds numbers. Once again, it can be observed that the curve for $250k$ fits the curves for $500k$ and $700k$ closely, with only small deviations at the point of the steep curve of the stall and a slight kink at 10° . There is a slight deviation in the 170° - 180° range, likely due to a complex aerodynamic situation related to the spoiler-like created shape and corresponding Reynolds number.

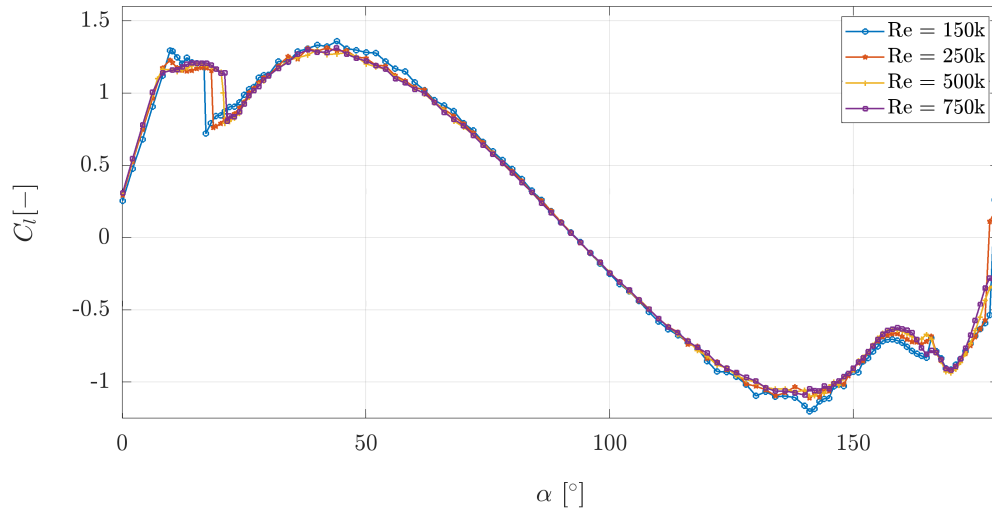


Figure 4.10: Comparison of corrected C_l values using combined Allen (0 to 20°) and Maskell (21 to 180°) wind tunnel corrections for different Reynolds numbers.

4.3.3. Pressure Coefficient

The comparison between uncorrected and corrected pressure coefficient values is essential for gaining valuable insights into the accuracy of aerodynamic measurements. This section also delves deep into stall aerodynamics at a Reynolds number of 250k, shedding light on this specific aerodynamic phenomenon at this particular Reynolds number.

The previous sections have shown that the deep stall angles require more correction compared to the lower angles. This is also evident when looking at Figure 4.11. The uncorrected C_p values for the angles 30°, 40°, 50°, and 90° are provided. It is observed that the corrected values for the 90°, depicted in Figure 4.11d, case deviate more from the measured values compared to the shown in Figure 4.11a 30° case, where it was found that the value for C_d is lower. Furthermore, it's crucial to take into account that the pressure ports located at the trailing edge were either not fully operational in the full wake or were damaged, leading to improper function. As a result, these specific points are not depicted in the images. Nonetheless, despite the absence of these last one or two ports, the C_p distribution shape remains distinctly visible. It is interesting to note the possible trend from the C_d and C_l graphs in the previous sections, which could indicate that the flow becomes largely separated for the angles of attack above 20°. This separation is also evident in the C_p plots, where the upper (suction) side shows a nearly flat plot, suggesting a significant separation of the flow with little pressure gradient. On the other hand, the lower (pressure) side of the airfoil exhibits the presence of a pressure gradient and attached flow. This observation highlights the flow separation phenomenon's substantial impact on the airfoil's aerodynamic behaviour beyond the 20° angle of attack.

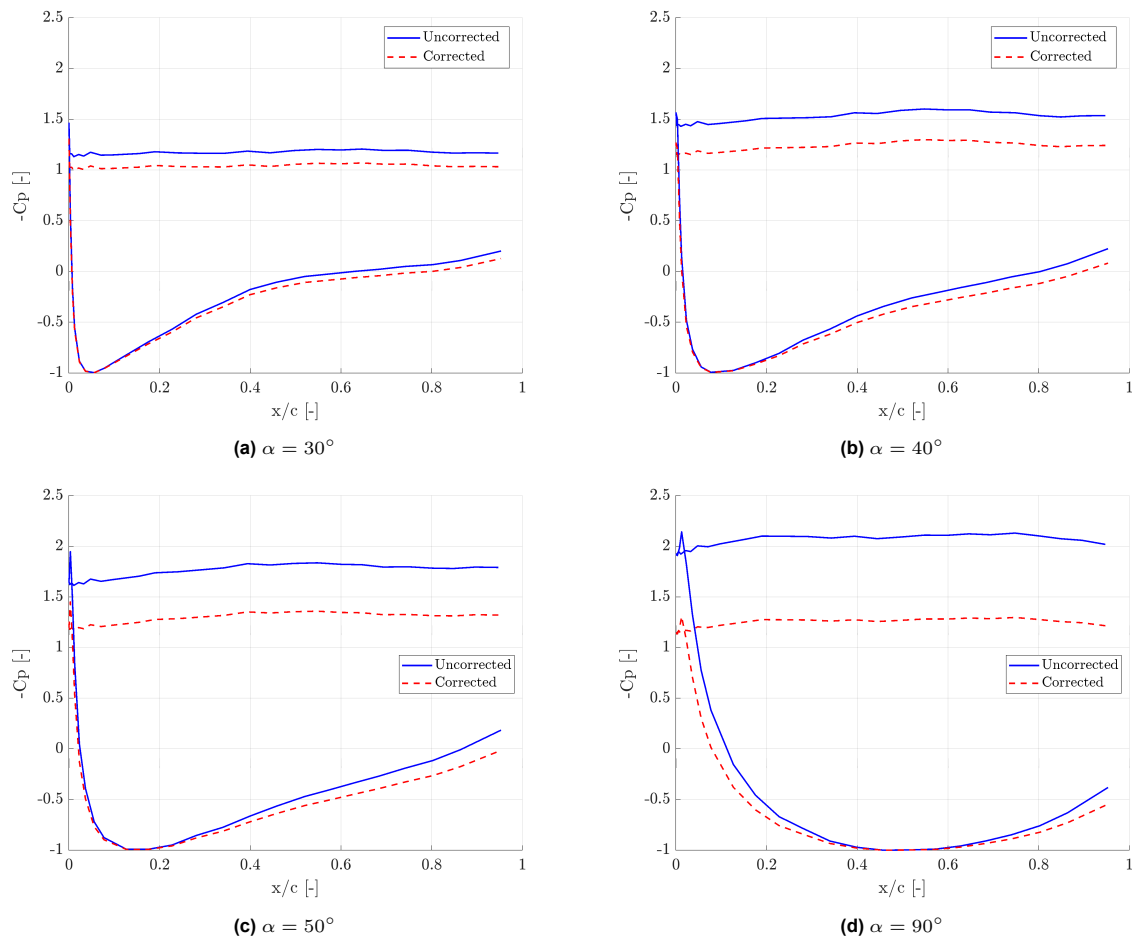


Figure 4.11: Comparison of uncorrected and corrected C_p values using Maskell wind tunnel corrections for different deep stall angles of attack at $Re = 250k$.

In the previous discussion in section subsection 4.3.2, it was observed that at a Reynolds number of $250k$, the airfoil's stall mode is likely due to trailing edge separation and the formation of a bubble on the suction side. Upon further examination of the C_p plots for the angles just before and just beyond the stall point at the same Reynolds number, it becomes even more apparent that this is the most likely stall mode. In the first image, Figure 4.12a, the plot at an angle of attack of 8° is presented. This instance occurs at the end of the 'linear' part of the C_l plot, and it can be observed that there is most likely a bubble present at the $x/c = 0.5$ location. As the angle of attack increases to 10° , where for this Reynolds number the $C_{l_{max}}$ is achieved before stall, this bubble is smoothed out. However, a small kink is still visible at the $x/c = 0.4$ location, but not as prominent as before.

Upon observing Figure 4.12c, two new aerodynamic events are evident. Firstly, the rear part of the suction side curve appears flatter, indicating likely separation. Secondly, it is noticeable that a new bubble has formed at the front of the suction side, or the existing bubble has split into a smaller and a larger one. In the subsequent images, Figure 4.12d and Figure 4.12e, the bubble will be further compressed towards the front. This can be observed by the kink just behind the initial peak moving closer to the front and becoming narrower compared to the kink at $\alpha = 12^\circ$. Additionally, the point of separation at the trailing edge will move forward as the flat part of the curve shifts from $x/c = 0.62$ to $x/c = 0.42$ and becomes longer. Eventually, as the airfoil is pushed beyond 18° to 18.5° , the bubble at the front likely bursts and joins the trailing edge separation, leading to a single large separation and the stall. From Figure 4.12f, it can be inferred that the entire flow is separated on the suction side, as the curve is completely flat from almost the entire front.

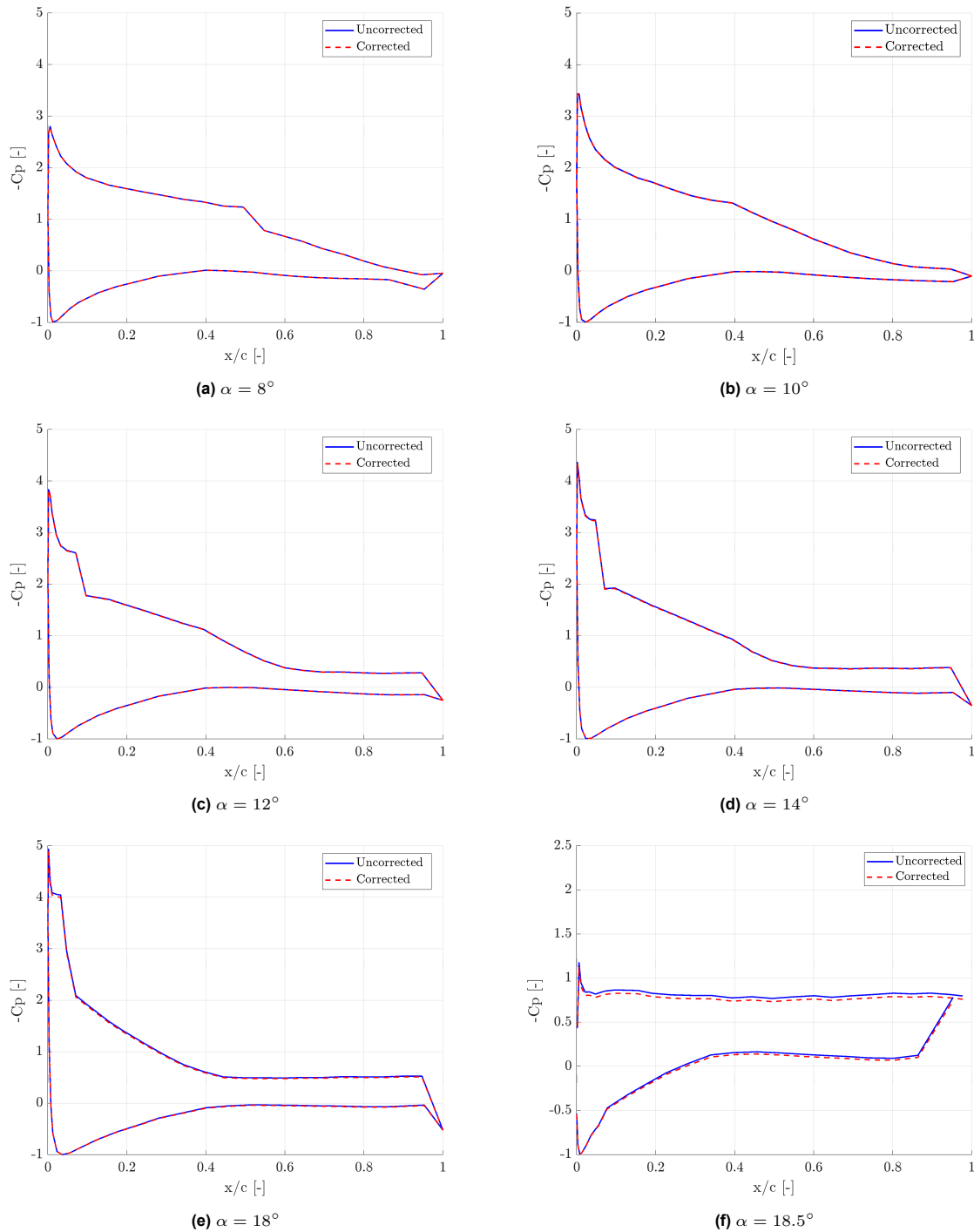


Figure 4.12: Comparison of uncorrected and corrected C_p values using Maskell wind tunnel corrections for different angles of attack at $Re = 250k$, showcasing the stall mode in static airfoil conditions.

4.3.4. PIV

The chapter presents and discusses PIV images for static airfoil cases to understand airflow under different conditions. Both average and instantaneous flow fields are analyzed to provide a complete picture of the airflow behaviour. Firstly, static average plots show the overall average flow patterns around the airfoil, giving a clear view of typical flow behaviour. Next, instantaneous plots reveal the dynamic aspects of the flow, such as turbulence and changing patterns that aren't visible in the average data. Specific cases with significant vortices are highlighted, showing how these vortices form, change, and affect the airfoil's performance. Understanding these vortices is key to understanding flow

separation and aerodynamic behaviour. Combining these views provides a thorough analysis of both steady and changing flow patterns, enhancing the understanding of static airfoil performance.

The static averaged flow fields at various angles (α) show different wake patterns and flow behaviours, providing insights into the aerodynamic characteristics of the airfoil. The PIV images for these cases are shown in Figure 4.13. At a low angle of attack of 10° (see Figure 4.13a), the wake is minimal and almost non-existent, which is in line with the expected behaviour for such a small angle. This corresponds with the small wake observed in pressure coefficient (C_p) plots for low angles, where only initial signs of leading-edge separation are visible. This was discussed in subsection 4.3.3. These signs match predicted regions, indicating early but minor trailing edge flow separation.

As the angle of attack increases to 40° , Figure 4.13b, a significant change is observed with a prominent reverse flow area depicted in deep blue. This reverse flow contracts more aggressively compared to other high-angle cases, indicating some flow recovery which most likely is initiated but the non-rotary outside flow. The flow around the wake area speeds up significantly, reaching velocities up to 1.8 times the incoming wind speed U_∞ . In front of the airfoil, the flow slows down considerably, as indicated by green colours, demonstrating the substantial impact of the wake on the incoming flow. At 50° , Figure 4.13c, the wake continues to grow, showing extensive flow separation. While the pattern is similar to the 40° case, the reverse flow contraction is less aggressive. The airflow speed around the wake increases significantly, similar to the 40° case, and the slowing of the flow in front of the airfoil remains evident.

At a 90° angle of attack, Figure 4.13d, the wake is the largest among all cases, as expected. The airflow separates around the airfoil, creating a vast wake region that is the largest of the shown cases. The airspeed around the wake area increases markedly, but not overly exceeding the speeds from the 40° and 50° cases, and the green areas in front of the airfoil indicate a substantial reduction in flow speed, highlighting the significant impact of the wake on the incoming flow. Moving to a 130° angle of attack, Figure 4.13e, the wake size remains considerable, with noticeable flow separation. The pattern is similar to the 50° case but with slight variations in wake shape and size. The airspeed increases significantly around the wake area, and the flow in front of the airfoil slows down notably, although reaching slightly less far than 50° .

At even higher angles of attack, such as 160° , Figure 4.13f, the wake remains large but not as extensive as at 90° . The flow separation and wake size are consistent with high angles of attack. The flow patterns show less significant speed increases around the wake shown by the less dark red areas in the plot and notable smaller area of slowing of the flow in front of the airfoil, akin to other high-angle cases. At 170° , Figure 4.13g, the wake is again relatively small, with the substantial flow acceleration still on the suction side, which is now the lower side in the frame. However, there is a larger wake which also starts more upstream on the airfoil compared to the 10° case. This is most likely due to the geometry of the airfoil being not designed to optimally function in this position and will be better represented by the term spoiler than an airfoil in such working operations.

The size of the wake gets larger as the angle of attack goes past the stall point (around 18.5°), with the biggest wake occurring at 90° . At high angles of attack (40° , 50° , 90° , and 130°), the airflow speeds up significantly around the wake area and slows down in front of the airfoil, showing the wake's impact on the incoming flow. In deep stall cases, like at 90° , there are dark blue areas in the wake, which indicate severe reverse flow. This reverse flow matches with the negative average flow in the x direction and the observed performance in pressure measurements. These results showcase the presence of wake size, flow separation, and speed changes that cause the difference in aerodynamic performance.

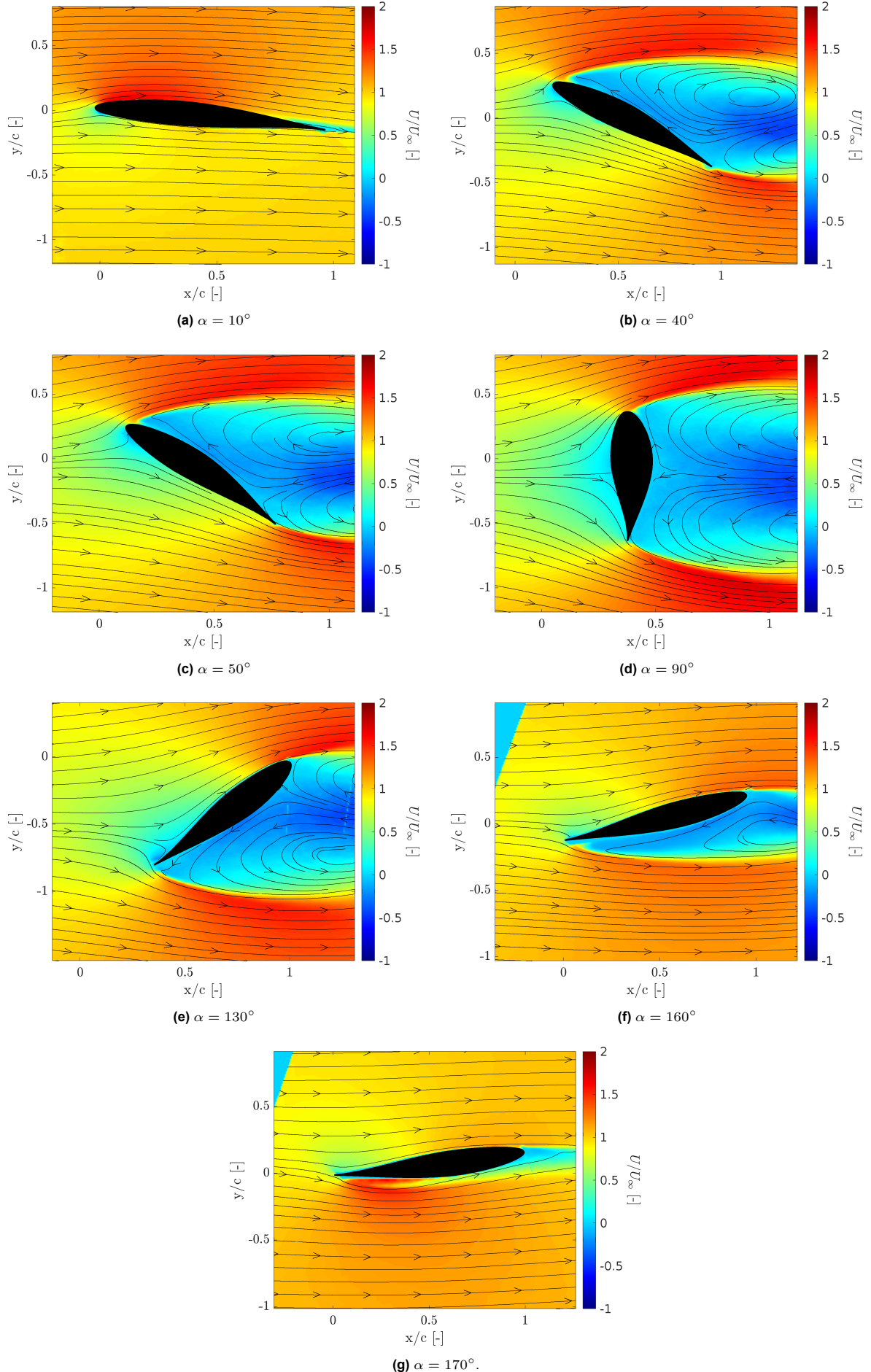


Figure 4.13: Static averaged flow fields (U/U_∞) at various α for $Re = 250k$ with the black lines showing the average flow field function.

The analysis of the static instantaneous flow fields at α of 40° , 50° , and 90° offers a detailed look at the dynamic behaviour of wake regions. These figures were chosen from the same time frame within their respective measurements, specifically from the 60th to the 65th image, to reduce bias in the plots. With the PIV installation's maximum camera speed at 15 Hz and the predicted sinusoidal corrected shedding frequency for all cases between 10 and 17 Hz, it is not possible with these frames to certainly determine the progression of individual structures within two frames.

For the 40° case, Figure 4.14, each instantaneous frame reveals a wake shape that roughly represents the static averaged PIV plots. However, noticeable differences arise in each frame, with certain areas appearing darker blue indicating reverse flow occurring at different locations at different times. Furthermore, the height of the wake varies between frames such as in Figure 4.14a and Figure 4.14c, where there is roughly $0.2 y/c$ height difference of the top boundary of the wake. This showcases the fluctuating motion of the wake region. This variability suggests a dynamic and unstable wake, where reverse flow regions shift over time, reflecting the transient nature of the flow field.

Moving to the 50° case, Figure 4.15, the differences in the wake become more pronounced and violent compared to the 40° scenario. While the general shape of the wake remains consistent with the static averaged plots, the instantaneous frames reveal a larger reverse flow area and regions of accelerated flow. In the final image of the sequence, mild reverse flow is observed, highlighting the erratic and fluctuating behaviour of the wake over time. This increased variability again indicates heightened turbulence.

At a 90° angle of attack, Figure 4.14, the differences in the wake across time instances are even more pronounced. Figure 4.16e shows a very large reverse flow area, while Figure 4.16c displays a wake region with both red and blue values in the U/U_∞ -component. This indicates chaotic behaviour in the wake region or the presence of one or multiple large vortices. The substantial variability in the wake structure at this angle suggests severe instability and complex vortex dynamics, leading to significant fluctuations in the flow field. These frames highlight the chaotic nature of the wake, characterized by large-scale flow separation and vortex shedding that varies dramatically from moment to moment.

The instantaneous flow fields at angles of attack of 40° , 50° , and 90° reveal dynamic and fluctuating wake behaviours that are not shown in the static averaged plots. At 40° , the wake exhibits shifting reverse flow regions and varying wake heights, indicative of an unstable and transient wake. At 50° , the wake differences become more violent, with larger reverse flow areas and more erratic behaviour, suggesting heightened turbulence. At 90° , the wake demonstrates even greater variability, with chaotic flow patterns and large vortices, indicating severe instability. This emphasizes the importance of capturing instantaneous flow fields to understand the transient behaviours not visible in static averaged plots, highlighting the complex and dynamic nature of wake regions at high angles of attack.

When examining the three standard deviation plots for the complete time series in Figure 4.14g, Figure 4.15g, and Figure 4.16g, similar conclusions can be drawn across the different angles of attack. The plot for the 90° case exhibits the most significant amount of deviation in the boundary of the wake, characterized by the thickest boundary. This deviation gradually decreases when moving to the 50° case, and it becomes even less pronounced in the 40° case. The progression indicates a clear trend where the boundary thickness and corresponding deviations are highest at 90° , moderate at 50° , and lowest at 40° , reflecting the changing flow dynamics in the wake at these angles.

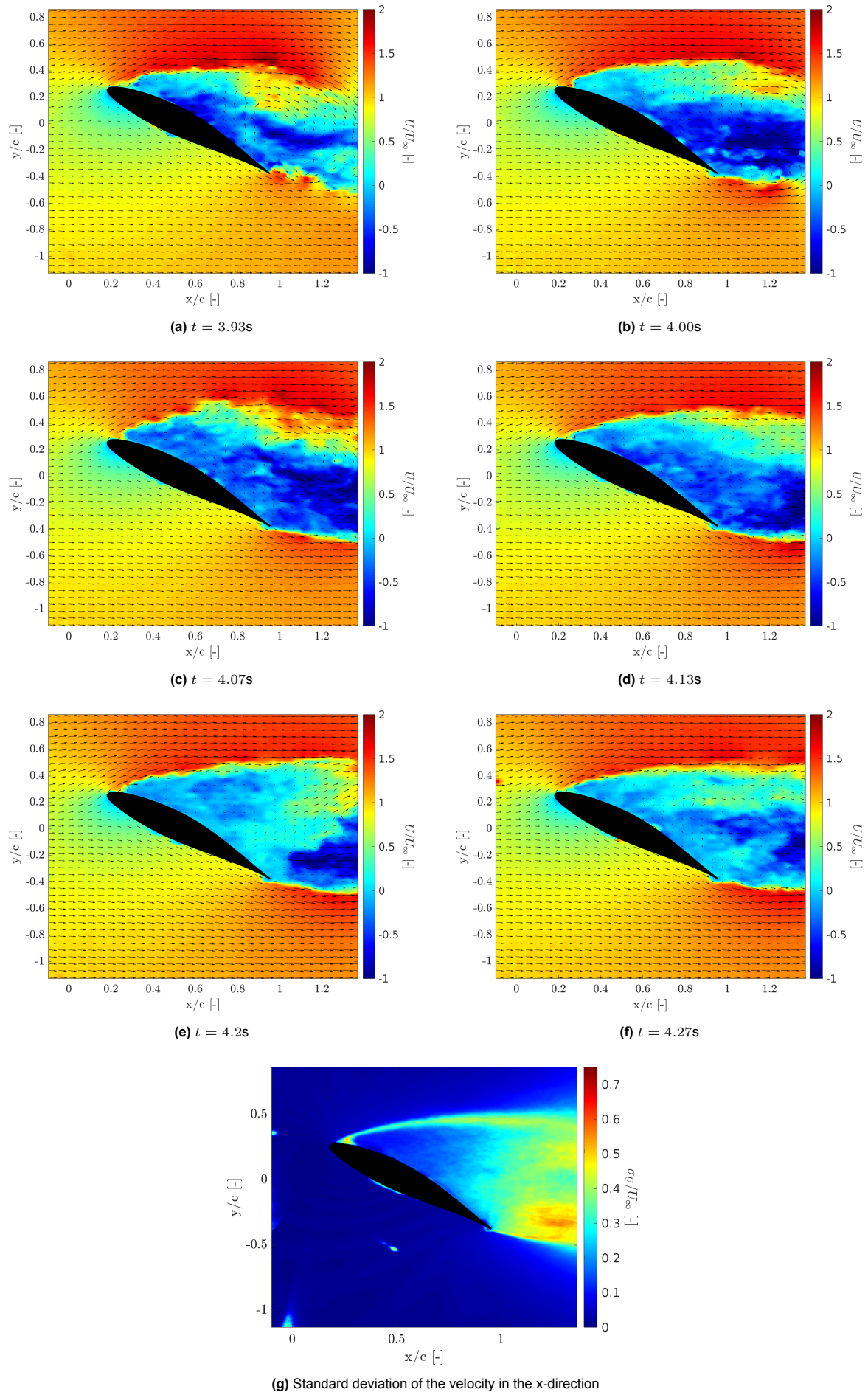


Figure 4.14: Instantaneous flow fields in a time series with vector arrows that display the relative magnitude and direction of the flow in both x- and y-direction and one standard deviation plot at $\alpha = 40^\circ$ and $Re = 250k$.

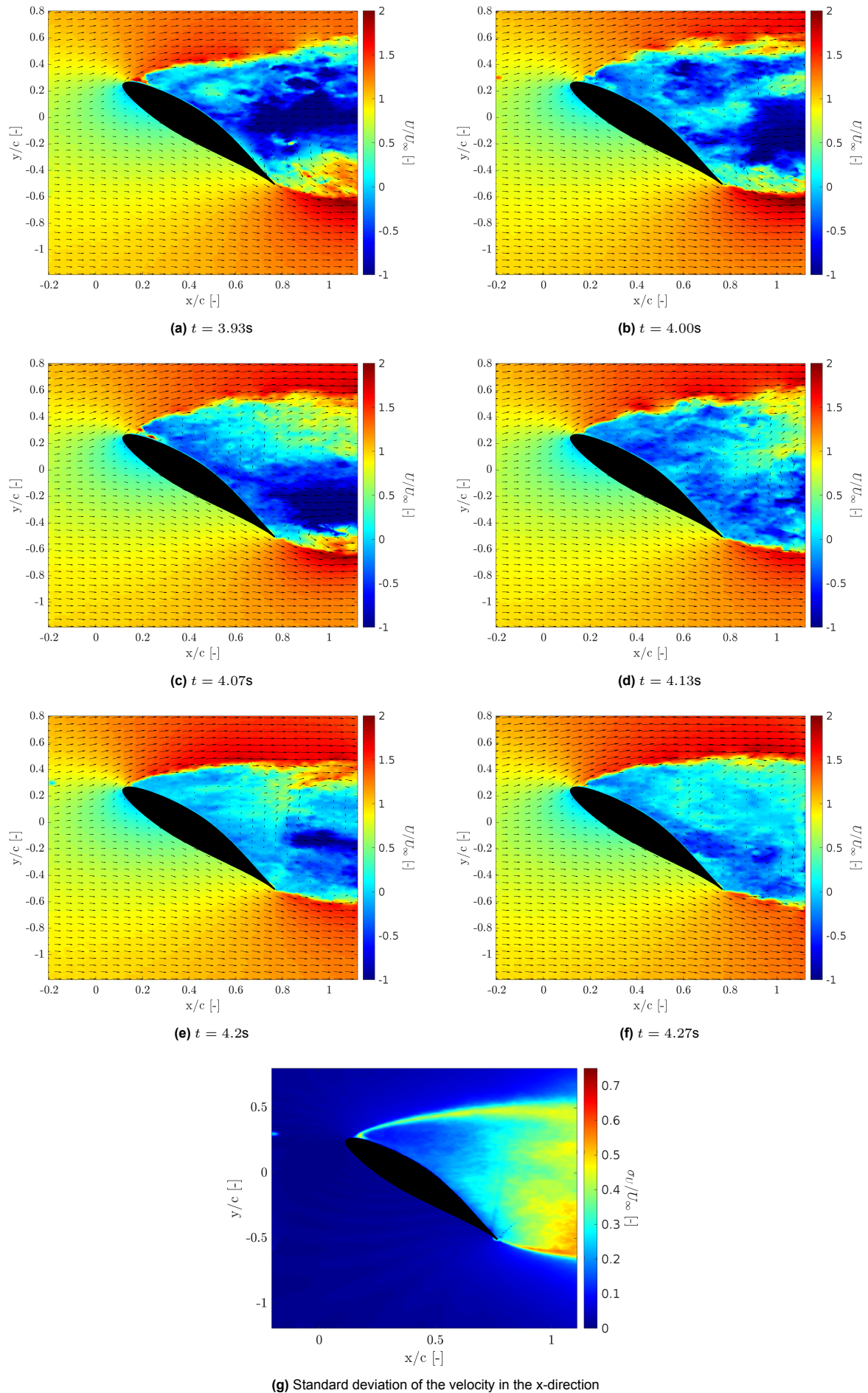


Figure 4.15: Instantaneous flow fields in a time series with vector arrows that display the relative magnitude and direction of the flow in both x- and y-direction and one standard deviation plot at $\alpha = 50^\circ$ and $Re = 250k$.

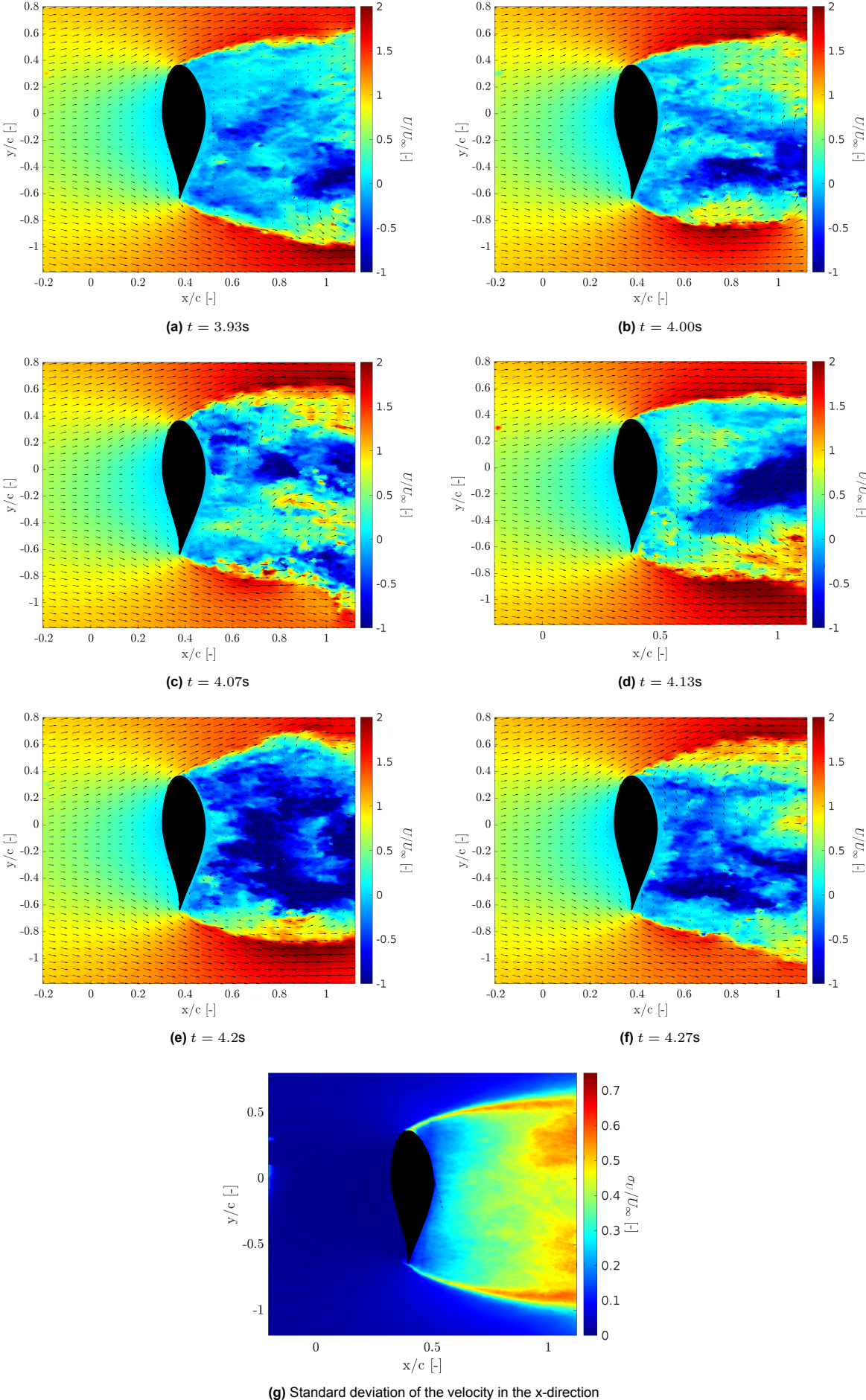


Figure 4.16: Instantaneous flow fields in a time series with vector arrows that display the relative magnitude and direction of the flow in both x- and y-direction and one standard deviation plot at $\alpha = 90^\circ$ and $Re = 250k$.

The analysis of the static instantaneous flow fields, depicted in Figure 4.17, Figure 4.18 and Figure 4.19, for α at 40° , 50° , and 90° provides insights into the presence and characteristics of vortex structures generated by the airfoil. Due to limitations in camera capture rates, individual structures cannot be tracked as they progress in time without certainty of continuity. Therefore, four chosen images depicting two large vortices created by the leading edge (blue) and two vortices created by the trailing edge (red) are analyzed. The blue colour indicates a clockwise-oriented vortex structure, while the red colour represents a counter-clockwise-oriented vortex structure.

In the 40° cases, significant vortex structures are present within the wake region. Analysis of individual images reveals predominantly negatively oriented flow rotation in the middle and upper halves of the wake, occasionally interspersed with positively oriented red vortices, likely being shed. Furthermore, the blue vortices appear larger, shown in Figure 4.17a and Figure 4.17b, compared to the red vortices. This concludes that the blue vortices exhibit a larger spatial extent compared to their red counterparts, a trend consistent with broader trends observed throughout the dataset. Not all images have been shown, only those displaying clear vortex structures. This is because including all individual images does not create a clearer image and will use up too much space. More images of the complete time series are shown in Appendix A.

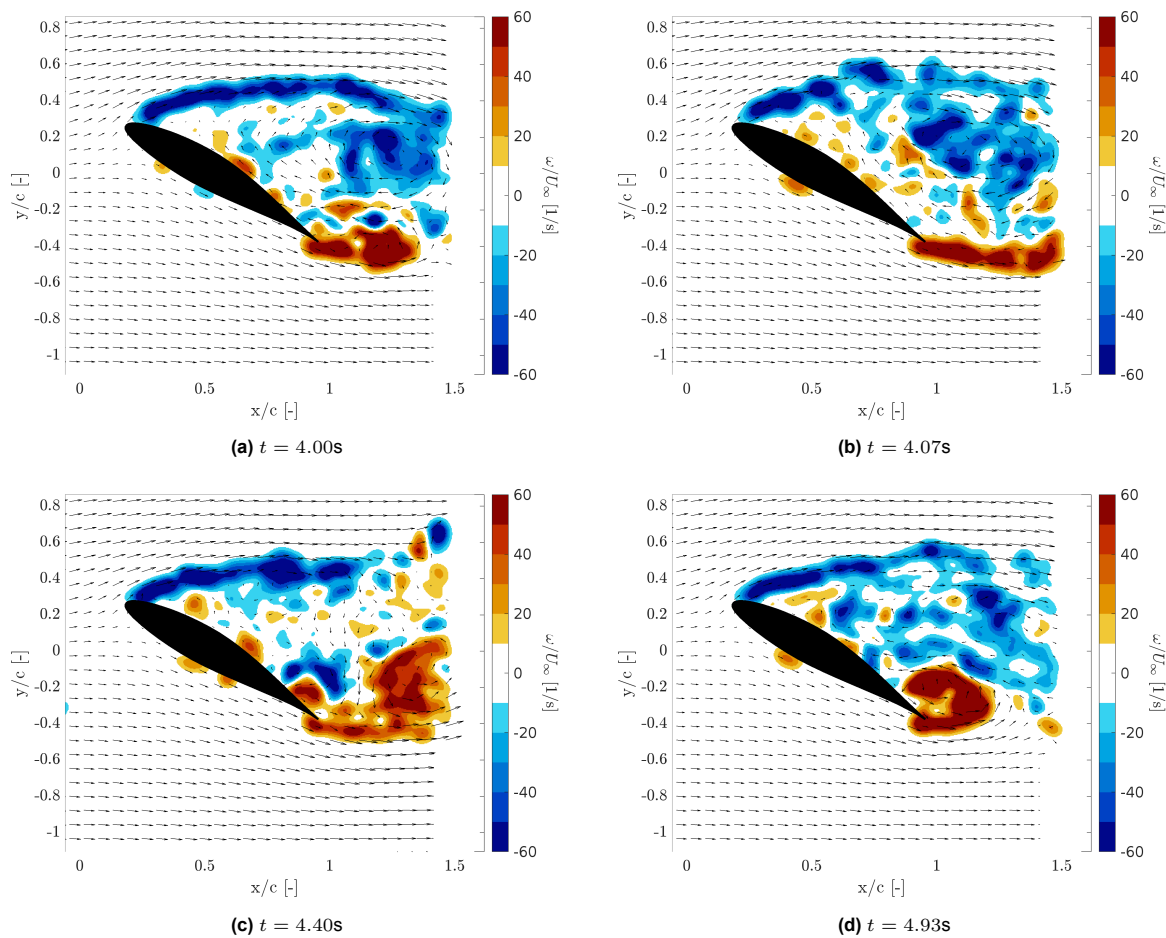


Figure 4.17: Instantaneous vorticity field (ω/U_∞) with vector arrows that display the relative magnitude and direction of the flow in both x- and y-direction at $\alpha = 40^\circ$ and $Re = 250k$.

When we shift to the 50° case, Figure 4.18, we observe that the red vortices grow significantly larger compared to the 40° case. At this point, the sizes of the blue and red vortices start to approach each other, with fewer occurrences of blue vortices starting to roughly align with the now larger red vortices. This suggests that the red vortices are exerting a greater influence. However, in general, blue vortices still outnumber red vortices, albeit by a small margin.

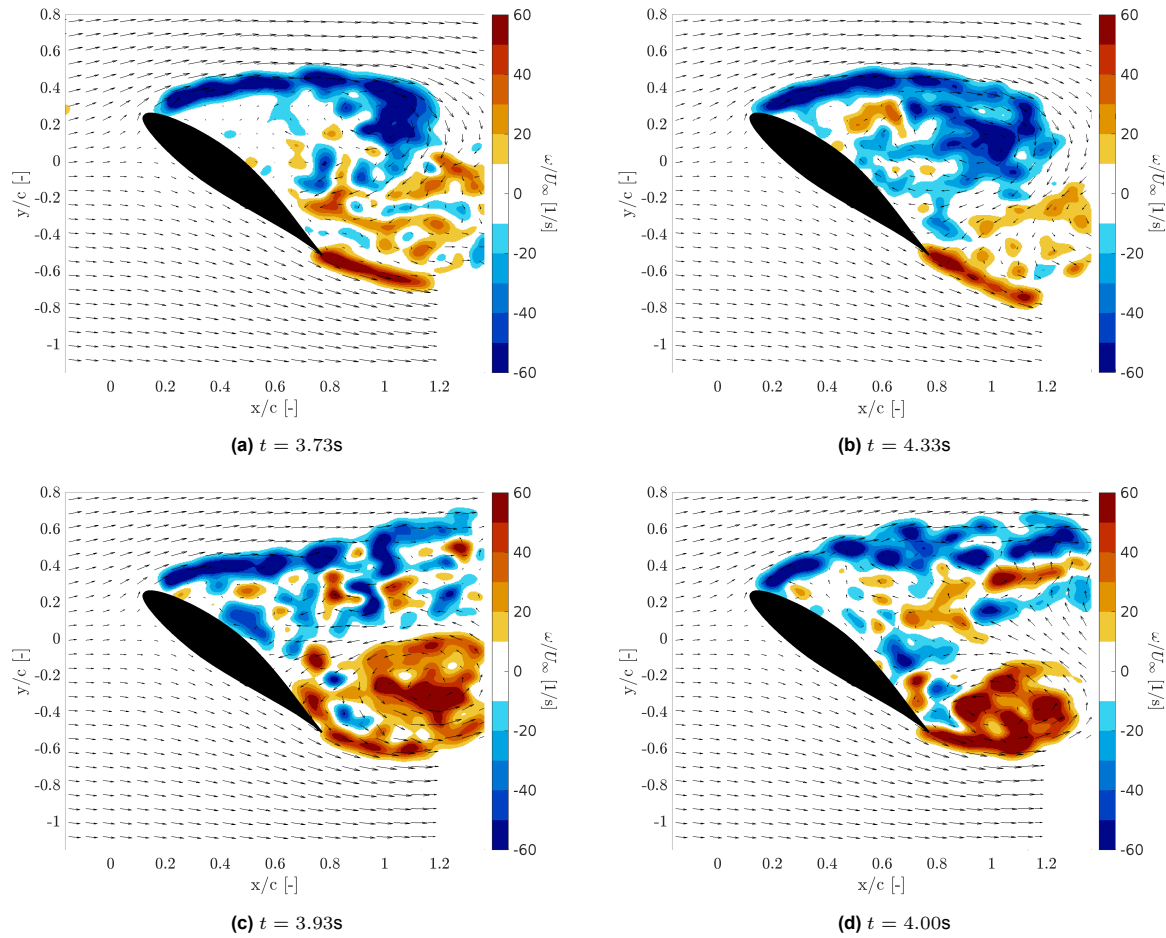


Figure 4.18: Instantaneous vorticity field (ω/U_∞) with vector arrows that display the relative magnitude and direction of the flow in both x- and y-direction at $\alpha = 50^\circ$ and $Re = 250k$.

In the 90° case, Figure 4.19, vortices of different orientations are similar in size and appear to occur relatively equally. Additionally, when large vortices are present near the leading or trailing edge, smaller vortices on the opposite side tend to flare out more away from the centre of the wake. This can be seen the best in Figure 4.19c and Figure 4.19d. This behaviour suggests that the shedding frequency might be creating a von Karman sheet, although this interpretation cannot be definitively confirmed based solely on the available data. Altogether this reveals the presence and behaviour of vortex structures at different angles of attack. While blue vortices tend to dominate in size and occurrence, red vortices show increased prominence at higher angles of attack.

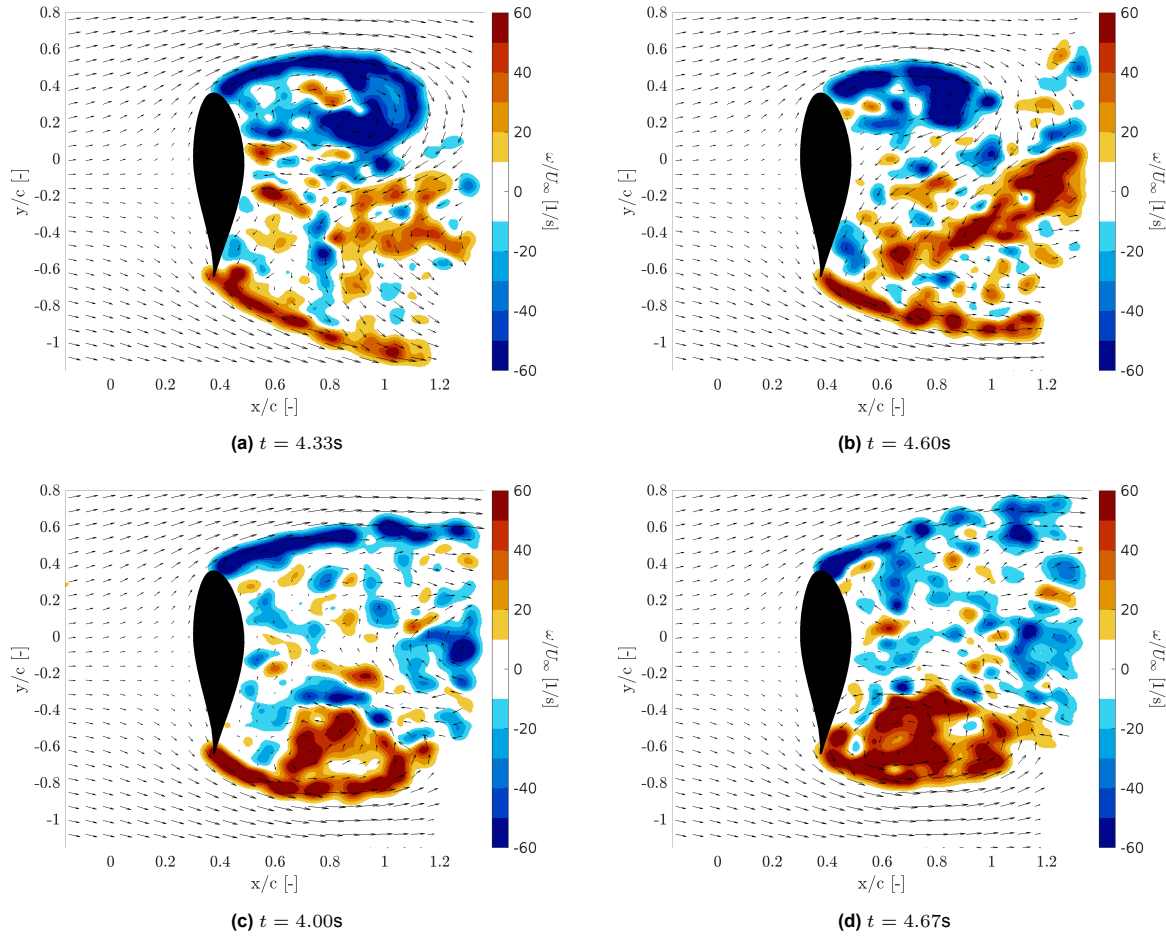


Figure 4.19: Instantaneous vorticity field (ω/U_∞) with vector arrows that display the relative magnitude and direction of the flow in both x- and y-direction at $\alpha = 90^\circ$ and $Re = 250k$.

4.4. Dynamic Cases

This section focuses on the various dynamic cases studied in the research, specifically looking at important aerodynamic factors like drag, lift, and pressure coefficient. The analysis also includes a study on cycle convergence, examining how pressure gauges respond dynamically. Additionally, the study looks at changes in the coefficient of drag (Given by C_{d_p} or $C_{d_{pressure}}$), which stands for the drag coefficient as calculated by the pressure distribution, and the coefficient of lift (C_l). To enhance our understanding of aerodynamic behaviour, we analyze phase-locked PIV images to observe the averaged flow patterns around the airfoil and in real-time. The main goal of this analysis is to thoroughly address the first two research questions related to the airflow around the airfoil and the forces acting on it during deep stall, using insights gained from dynamic scenarios.

4.4.1. Cycle Convergence Study

The analysis of the number of cycles required for dynamic measurements underscores the significance of achieving convergence to meaningful average values. Using 150 cycles as a base value, the examination reveals notable insights. Firstly, across different cycle counts ranging from 10 to 150 cycles, the mean values consistently fall within the same ballpark, as depicted in Figure 4.20. However, significant deviations, particularly evident in lower cycle counts, highlight the importance of cycle selection. Notably, the 100 and 150-cycle cases exhibit smoother, less oscillatory behaviour compared to lower cycle counts (10-25 cycles). This oscillatory behaviour, attributed to the shedding of vortices impacting C_{d_p} and C_l values, underscores the necessity of sufficient cycle counts to mitigate such fluctuations. The test case was done for a mean angle of attack of 40° , frequency of 2 Hz, and amplitude of 5° . Furthermore, the relative differences or errors are depicted in Figure 4.21. This analysis demonstrates

that the percentage variability relative to the 150-cycle average remains relatively small, with deviations never exceeding 2% for both C_d and C_l values in cases with 25 or more cycles. Thus, it can be inferred that a minimum of 50 to 100 cycles is requisite for obtaining an average less susceptible to individual oscillatory behaviour. Initial testing was conducted with cycle counts of 15 and 20, based on prior literature, which suggested values around or below 15 cycles. However, subsequent findings revealed that 150 cycles yield a less oscillatory average, prompting their adoption. Exceptionally, mean angle cases at 90° were tested only with 15 cycles; however, their inclusion is warranted due to the reduced oscillatory behaviour observed in C_{d_p} and C_l graphs and the more linear behaviour of these parameters. This comprehensive analysis underscores the critical importance of cycle count selection in dynamic measurements, ensuring robust and reliable results essential for advancing our understanding of aerodynamic behaviour.

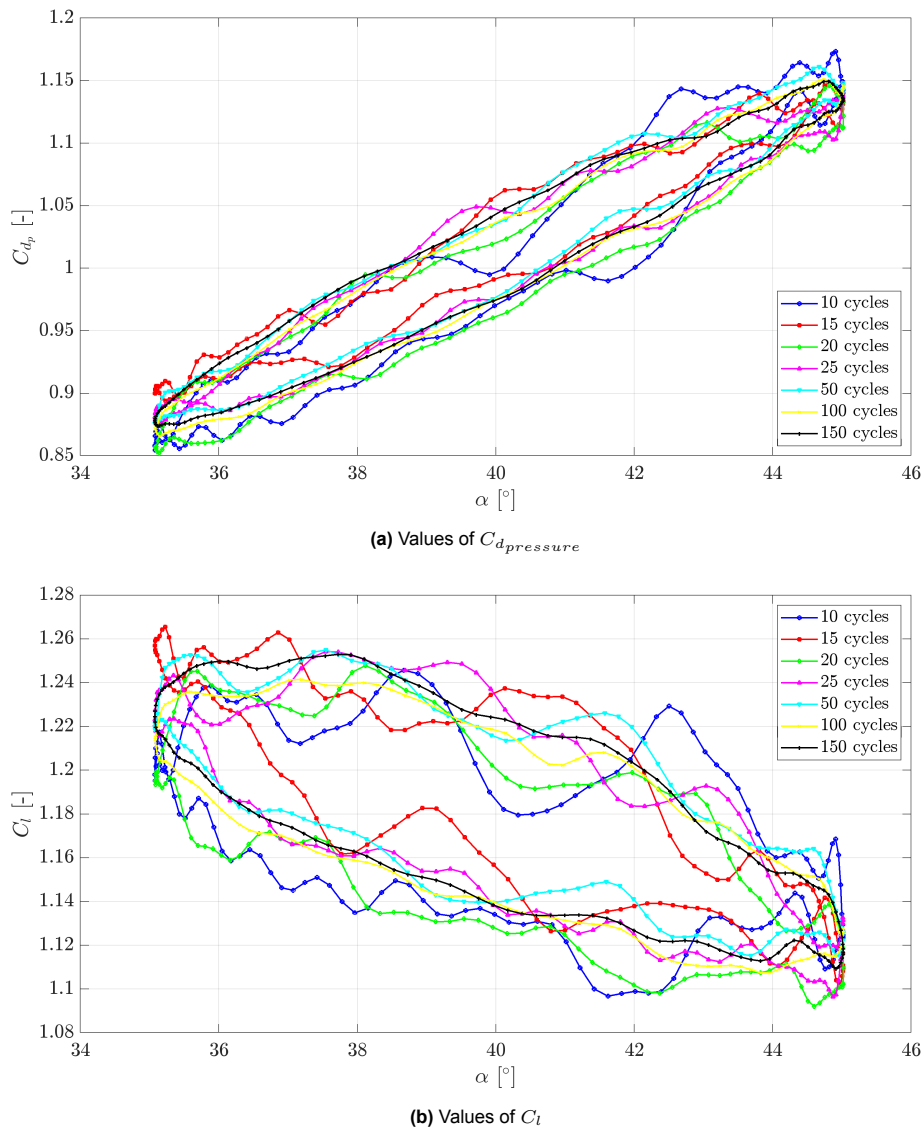


Figure 4.20: Comparison of C_l and C_d for different amount of data acquisition cycles.

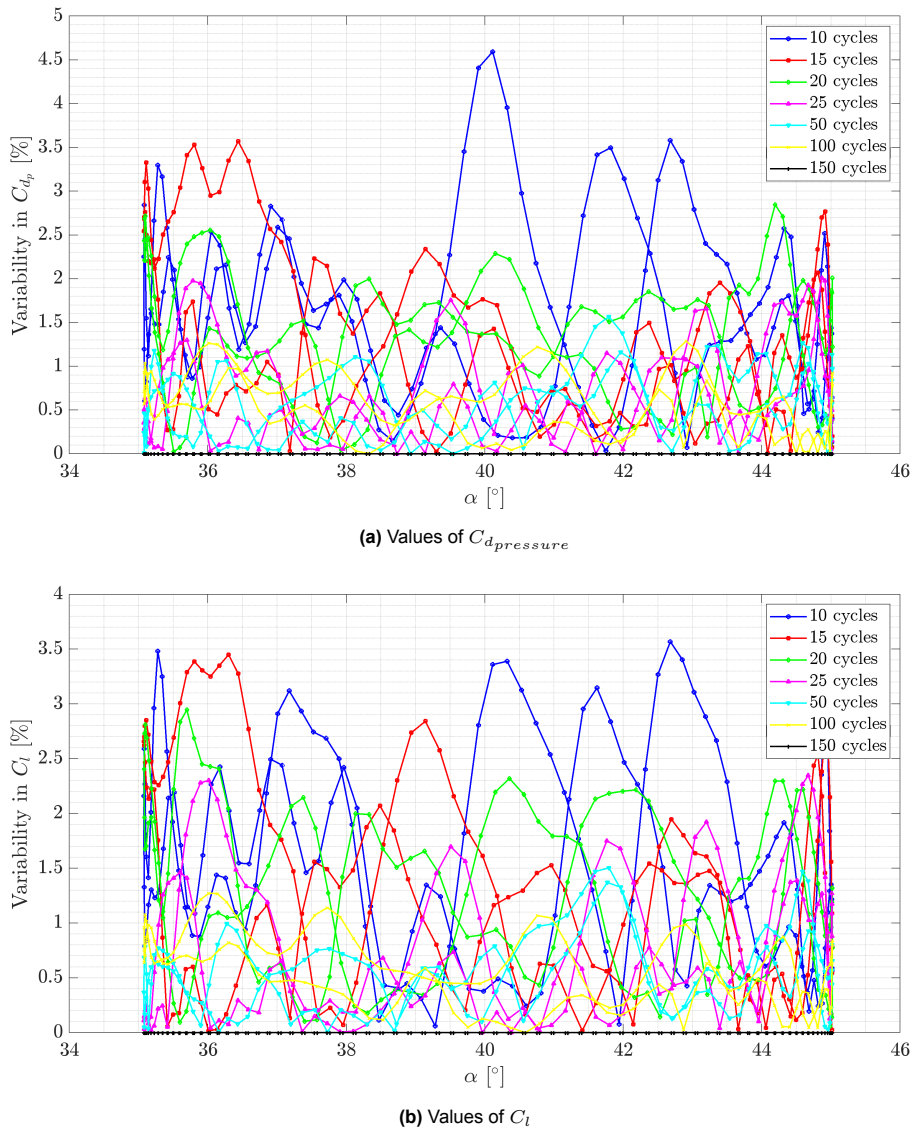


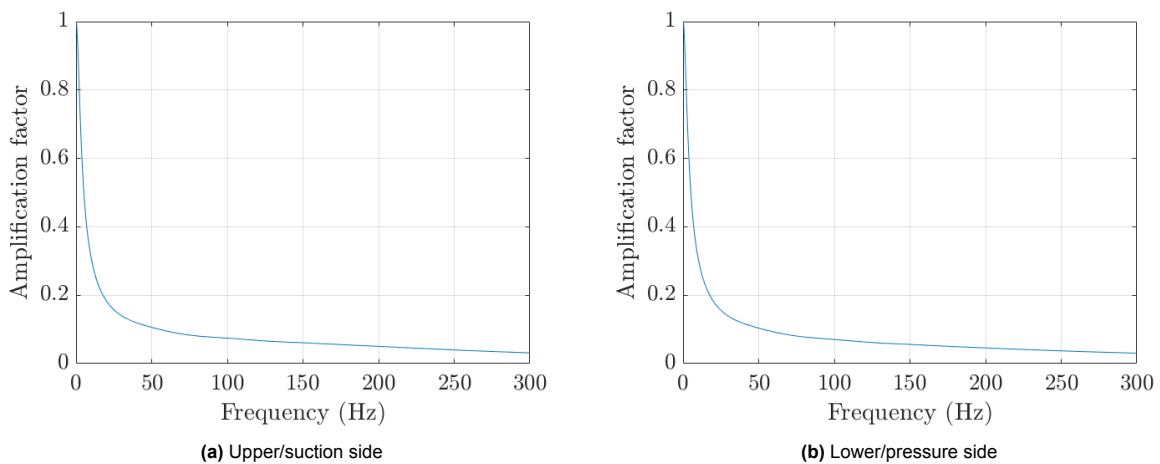
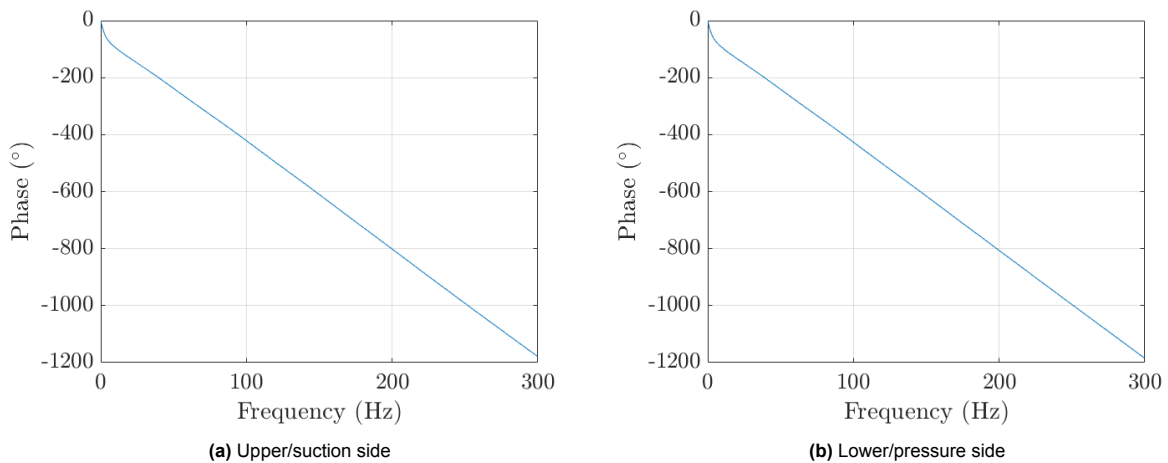
Figure 4.21: Comparison of the percentage variability of C_l and C_d for different amount of data acquisition cycles.

4.4.2. Dynamic Pressure Response

The analysis of dynamic pressure correction focuses on addressing the amplification factor and phase corrections to ensure accurate pressure readings during dynamic testing. Despite variations in connector lengths and tube configurations, which lengths are shown in Table 4.2, the response values for the upper and lower surfaces of the airfoil tend to be nearly identical, indicating similar performance across different connectors. The corrections were computed using the package from Jorge Caetano Alves (2005). The results are displayed in Figure 4.22 and Figure 4.23. To account for delays in pressure readings inherent in dynamic testing, corrections were applied to the incoming signals of each pressure port. These corrections are crucial for synchronizing the recorded pressure data with the actual aerodynamic events occurring on the airfoil surfaces.

Table 4.2: Measured dimensions of the pressure gauges tubes used during dynamic testing.

	$D_{inner,upper}$ [mm]	$L_{inner,upper}$ [mm]	$D_{inner,lower}$ [mm]	$L_{inner,upper}$ [mm]
Tap	0.40	3	0.40	3
Steel Tube	0.70	450	0.70	450
Plastic Tube	0.80	220	0.80	220
Adapter	0.80	9	0.80	9
Plastic Tube	1.00	2000	1.00	2000
Connector	0.95	6,9	0.65	6,9
Tube	1.00	500	1.00	500
Scanner	0.65	15	0.65	15

**Figure 4.22:** Amplitude factor response dynamic pressure for the upper and lower side of the airfoil.**Figure 4.23:** Phase response dynamic pressure for the upper and lower side of the airfoil.

One significant challenge encountered was the amplification of non-existent higher frequencies in the original data, which resulted in highly oscillatory corrected values that did not accurately represent the physical phenomena. This issue arose from the computed response values and their tendency to amplify higher frequency components disproportionately. To mitigate this problem, a high-pass filter was introduced. The primary function of this filter was to eliminate these artificially boosted high-frequency components, thereby producing more realistic and smooth corrected pressure values.

The low-pass filter was set to 60 Hz, a value determined by considering the maximum pitching frequency of the airfoil, which is 4 Hz. The filter setting was chosen to be ten times this maximum frequency, with an additional 50% safety factor to ensure comprehensive filtering of undesired high-frequency noise while maintaining the integrity of the actual pressure signal. This approach effectively smooths out the pressure data, making it more representative of the true aerodynamic conditions experienced by the airfoil.

The analysis of dynamic pressure correction and the original signal for the 40° cases reveals several critical insights. The values for the two frequency cases are depicted in Figure 4.24 and Figure 4.25. Firstly, the presence of several pronounced peaks is evident in the data. One such peak occurs at 0 Hz, which is likely an artefact of the experimental setup. This artefact arises because the pitching motion could only be initiated after the measurements had started in LabVIEW, occasionally resulting in a 0 Hz frequency reading. This peak is not of primary interest as it does not represent actual aerodynamic phenomena.

More importantly, a prominent peak at the pitching frequency is consistently observed for both pitching frequencies of 2 Hz and 3 Hz. This clear peak signifies the primary oscillatory motion induced by the pitching action. Additionally, for higher amplitude cases, another smaller peak appears close to the pitching frequency, specifically at twice the pitching frequency. This secondary peak suggests the occurrence of phenomena that manifest once every two cycles, possibly related to non-linear dynamic effects or periodic flow separation and reattachment events.

Another significant peak is observed at around 18 Hz, which is more prominent in the spectra with a 5° amplitude compared to those with 10° and 15° amplitudes. This 18 Hz peak corresponds to the expected shedding frequency in static conditions, leading to a sin corrected Strouhal number of approximately 0.19. This value aligns well with the estimated Strouhal number presented in section 3.1, corroborating the presence of vortex-shedding phenomena at this frequency.

Furthermore, as the amplitude of the pitching motion increases, several trends become noticeable. The amplitude of the main frequency shedding peak decreases, indicating a redistribution of energy across a broader frequency range. This is accompanied by the spreading of side lobes, reflecting increased flow unsteadiness and complexity. Additionally, the peaks at both the primary pitching frequency and its harmonic (twice the pitching frequency) become more pronounced. This amplification could indicate that higher pitching amplitudes lead to a more significant effect on the dynamic response of the airfoil, resulting in more noticeable periodic flow features and interactions influenced by pitching.

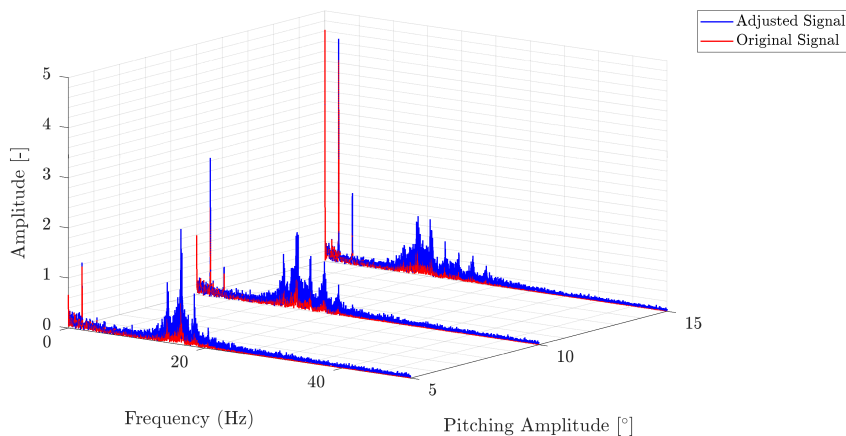


Figure 4.24: Single-sided amplitude plot for the original signal and the dynamic response corrected signal for $\alpha_{mean} = 40^\circ$ at $f_{pitching} = 2\text{Hz}$.

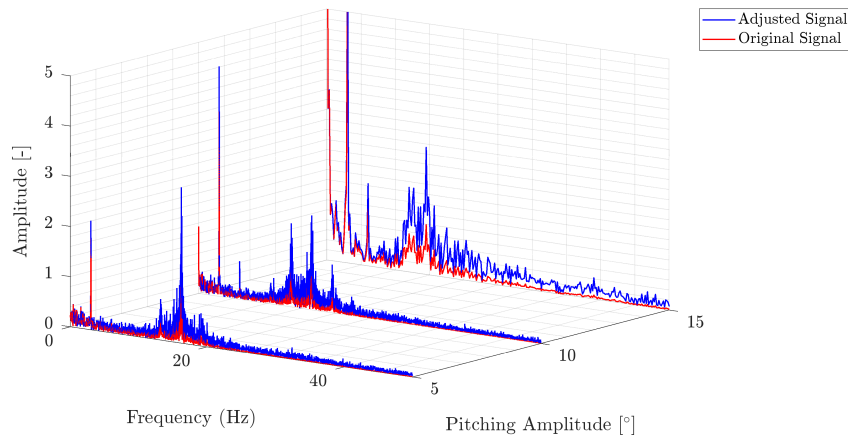


Figure 4.25: Single-sided amplitude plot for the original signal and the dynamic response corrected signal for $\alpha_{mean} = 40^\circ$ at $f_{pitching} = 3\text{Hz}$.

The analysis of dynamic pressure correction and the original signal for the 50° cases reveals patterns that largely align with the observations from the 40° cases, with some notable differences. In both cases, shown in Figure 4.26 and Figure 4.27, the frequencies at the pitching frequency and its harmonic become more pronounced as the amplitude of the pitching motion increases. This trend indicates that higher pitching amplitudes amplify the dynamic response, making the primary oscillatory components more prominent.

However, in the low amplitude cases for the 50° scenarios, there is a noticeable reduction in the presence of side lobes at the higher frequency peak. For these cases, the primary peak is around 13 Hz, resulting in a sin-corrected Strouhal number of 0.165. This suggests a cleaner shedding of vortices at the same frequency, implying a more stable and regular vortex-shedding process under these conditions. The reduction in side lobes indicates less flow unsteadiness and fewer secondary oscillations, which could point to a more uniform aerodynamic response.

Additionally, for the 50° case with a pitching frequency of 3 Hz, the peaks at the harmonic frequency (twice the pitching frequency) are lower compared to the primary pitching frequency. This reduction suggests that fewer double-cycled phenomena are occurring, indicating a simpler dynamic behaviour at this higher angle of attack and pitching frequency. The lower harmonic peaks imply that the energy distribution is more concentrated around the primary pitching frequency, with less influence from higher-order harmonics.

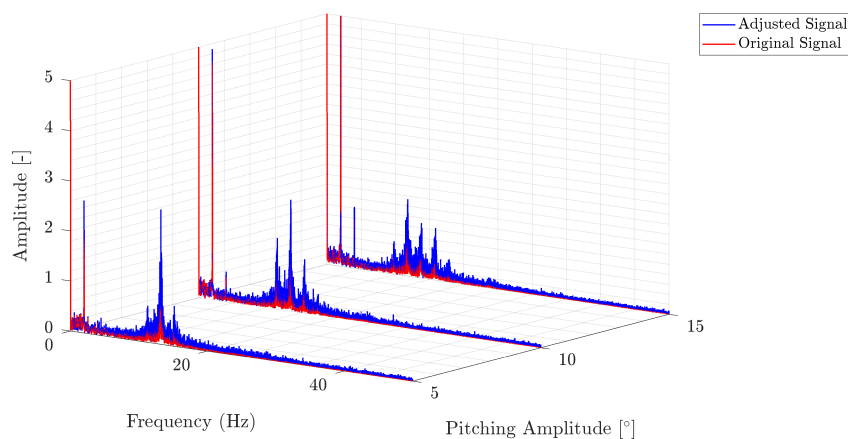


Figure 4.26: Single-sided amplitude plot for the original signal and the dynamic response corrected signal for $\alpha_{mean} = 50^\circ$ at $f_{pitching} = 2\text{Hz}$.

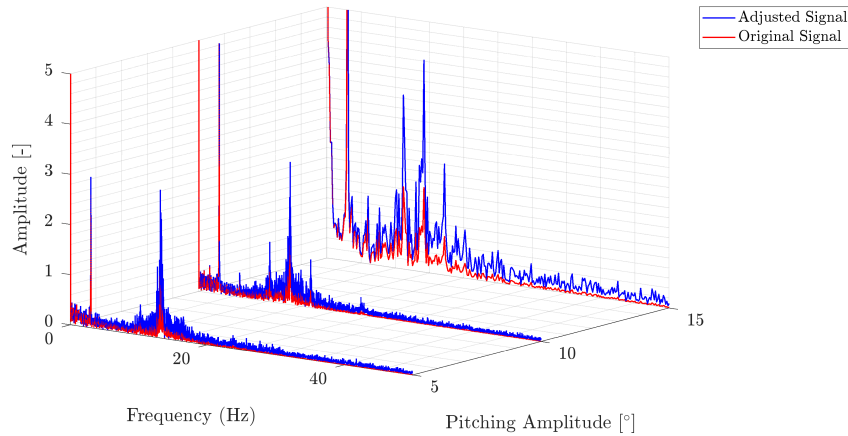


Figure 4.27: Single-sided amplitude plot for the original signal and the dynamic response corrected signal for $\alpha_{mean} = 50^\circ$ at $f_{pitching} = 3\text{Hz}$.

The analysis of dynamic pressure correction and the original signal for the 90° cases offers valuable insights, though it is constrained by the limitations of the testing setup. Due to the actuator overheating, only 15-cycle measurements were feasible for this angle of attack, precluding the completion of an additional 150-cycle measurements. Despite this limitation, several significant conclusions can be drawn from the available data.

Firstly, many of the observations from the 40° and 50° cases apply to the 90° scenarios as well. However, a notable exception is the behaviour of the shedding frequency peak. Which in this case is around 11 Hz, leading to a corrected Strouhal number of 0.18. Unlike the lower angle cases, the shedding frequency peak at 90° does not exhibit significant side lobes as the pitching amplitude increases. This suggests a more stable and consistent vortex shedding process, even at higher amplitudes, indicating less flow unsteadiness and fewer secondary oscillations around the primary shedding frequency.

Additionally, the absence of harmonic frequencies in the 90° plots is a significant deviation from the 40° and 50° cases. In the lower angle scenarios, harmonic frequencies were prominent, especially at higher pitching amplitudes. The lack of such harmonics in the 90° cases indicates that the flow dynamics are dominated by the primary frequencies—shedding and pitching—without significant contributions from higher-order oscillations.

These findings imply that, at a 90° angle of attack, the flow field is primarily characterized by the periodic phenomena of shedding and pitching frequencies. The reduced complexity in the frequency spectrum suggests a more straightforward dynamic behaviour compared to the lower angles of attack, where multiple harmonics and side lobes introduced additional complexity.

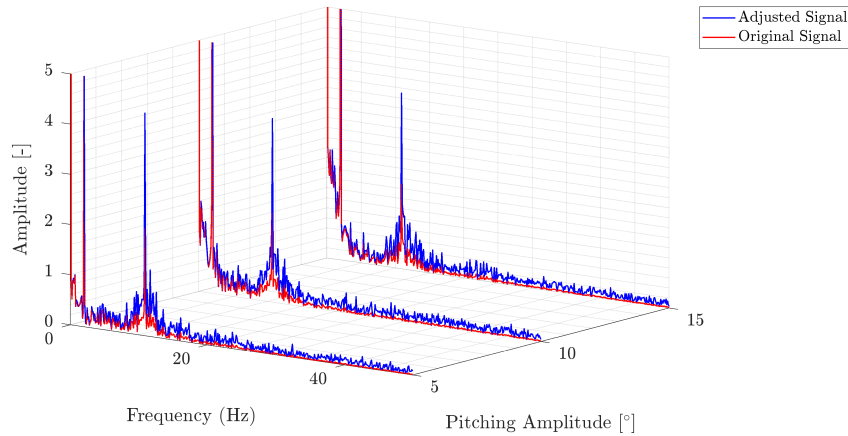


Figure 4.28: Single-sided amplitude plot for the original signal and the dynamic response corrected signal for $\alpha_{mean} = 90^\circ$ at $f_{pitching} = 2\text{Hz}$.

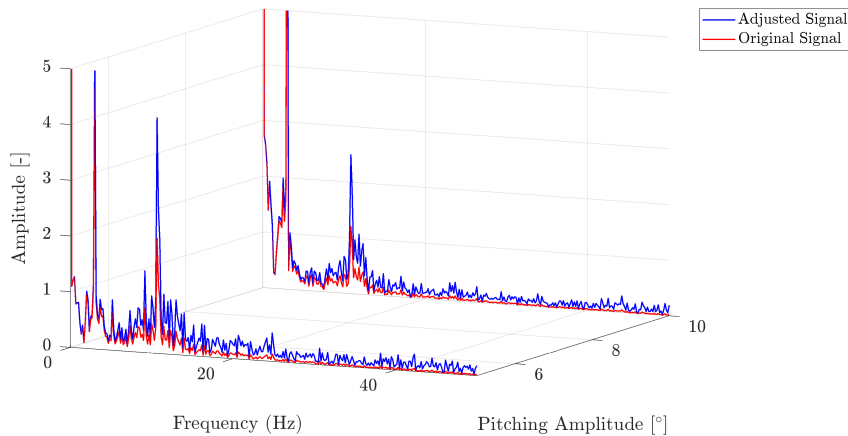


Figure 4.29: Single-sided amplitude plot for the original signal and the dynamic response corrected signal for $\alpha_{mean} = 90^\circ$ at $f_{pitching} = 3\text{Hz}$.

4.4.3. Drag Coefficient

The analysis of the $C_{d_{pressure}}$ vs α plots for the mean angle 40 cases, shown in Figure 4.30, reveals important insights into the dynamic aerodynamic behaviour of the airfoil. At lower pitching amplitudes, such as Figure 4.30a, Figure 4.30c and Figure 4.30e, individual cycles show less synchronization with the mean value, resulting in a scattered distribution around the mean hysteresis loop. This scatter indicates that at lower amplitudes, the flow could be significantly influenced by the vortex shedding frequency rather than primarily by the pitching frequency and amplitude, leading to irregularities in the $C_{d_{pressure}}$ values due to intermittent flow separation and reattachment. Fewer individual lines cross the middle of the hysteresis loop, suggesting a less stable aerodynamic response in the mid-range of the angle of attack.

Conversely, higher pitching frequencies result in a more oval-shaped mean hysteresis loop, compared to the flatter, disk-shaped loops observed at lower frequencies. The oval shape of the hysteresis loop at higher frequencies indicates a more regular and predictable oscillatory behaviour, suggesting that the aerodynamic forces become more synchronized with the pitching motion, resulting in a relatively less oscillatory drag response. As the pitching amplitude increases, individual cycles align more closely with the mean loop, reducing scatter and indicating a stronger influence of the pitching motion on the flow, which diminishes the relative impact of vortex shedding and results in a more stable aerodynamic behaviour. This transition from a flat disk-shaped to an oval-shaped hysteresis loop with

increased pitching frequency signifies a shift in dominant aerodynamic forces, with the airfoil's motion synchronizing better with the aerodynamic forces, leading to a smoother and more continuous drag response.

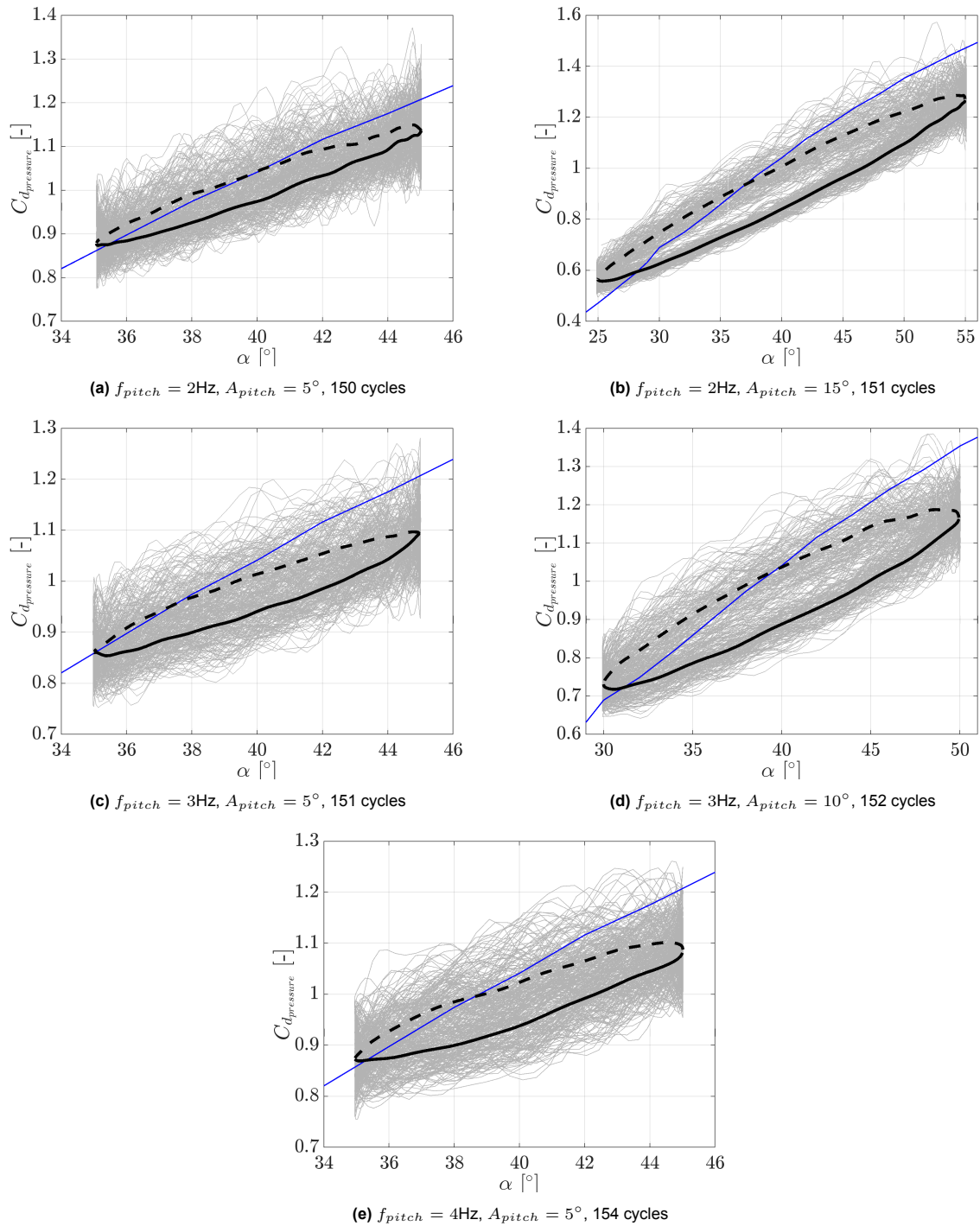


Figure 4.30: Comparison of $C_{d,pressure}$ for unsteady cases at $\alpha_{mean} = 40^\circ$ and $Re = 250k$. The black line represents the mean value, with the solid line representing the upstroke motion, the dashed line representing the downstroke motion and the blue line the values of static measurements.

The analysis of the $C_{d,pressure}$ vs α plots for the mean angle 50° cases reveals several important aspects of the airfoil's dynamic aerodynamic behaviour. These graphs for again the same cases have been depicted in Figure 4.31. One notable observation is that the $C_{d,pressure}$ values for the 50° cases are

significantly lower than the corresponding static values. The observed discrepancy could potentially be attributed to the dynamic effects linked to the airfoil's motion. However, a comprehensive presentation of evidence supporting this assertion is currently lacking.

Another key observation is that the slope of the hysteresis loop for the dynamic cases matches the slope of the static values. Additionally, the upstroke phase of the loop consistently shows higher drag values compared to the downstroke phase. This indicates that during the upstroke, the airfoil experiences greater drag, potentially due to the higher effective angle of attack. In contrast, during the downstroke, the airfoil might benefit from a propelling motion that reduces drag. The similarity in slopes between the static and dynamic cases suggests that the fundamental aerodynamic characteristics of the airfoil remain consistent, despite the dynamic conditions.

As the pitching amplitude ($A_{amplitude}$) and frequency ($f_{pitching}$) increase, the mean hysteresis loop becomes more pronounced and loopy. This indicates that higher pitching energy leads to greater variations in drag values between the upstroke and downstroke phases. The more pronounced loopiness at higher pitching amplitudes and frequencies suggests that increased pitching energy causes significant changes in the aerodynamic forces acting on the airfoil, resulting in a more dynamic response.

The plots also display erratic behaviour, with some individual cycle values deviating up to 20% from the mean values. This erratic behaviour indicates that significant unsteady aerodynamic effects are at play, likely due to the complex interaction between the airfoil's motion and the surrounding flow. The substantial deviations in individual cycles suggest that each cycle can experience markedly different aerodynamic forces, emphasizing the necessity of considering a large number of cycles to obtain reliable average values.

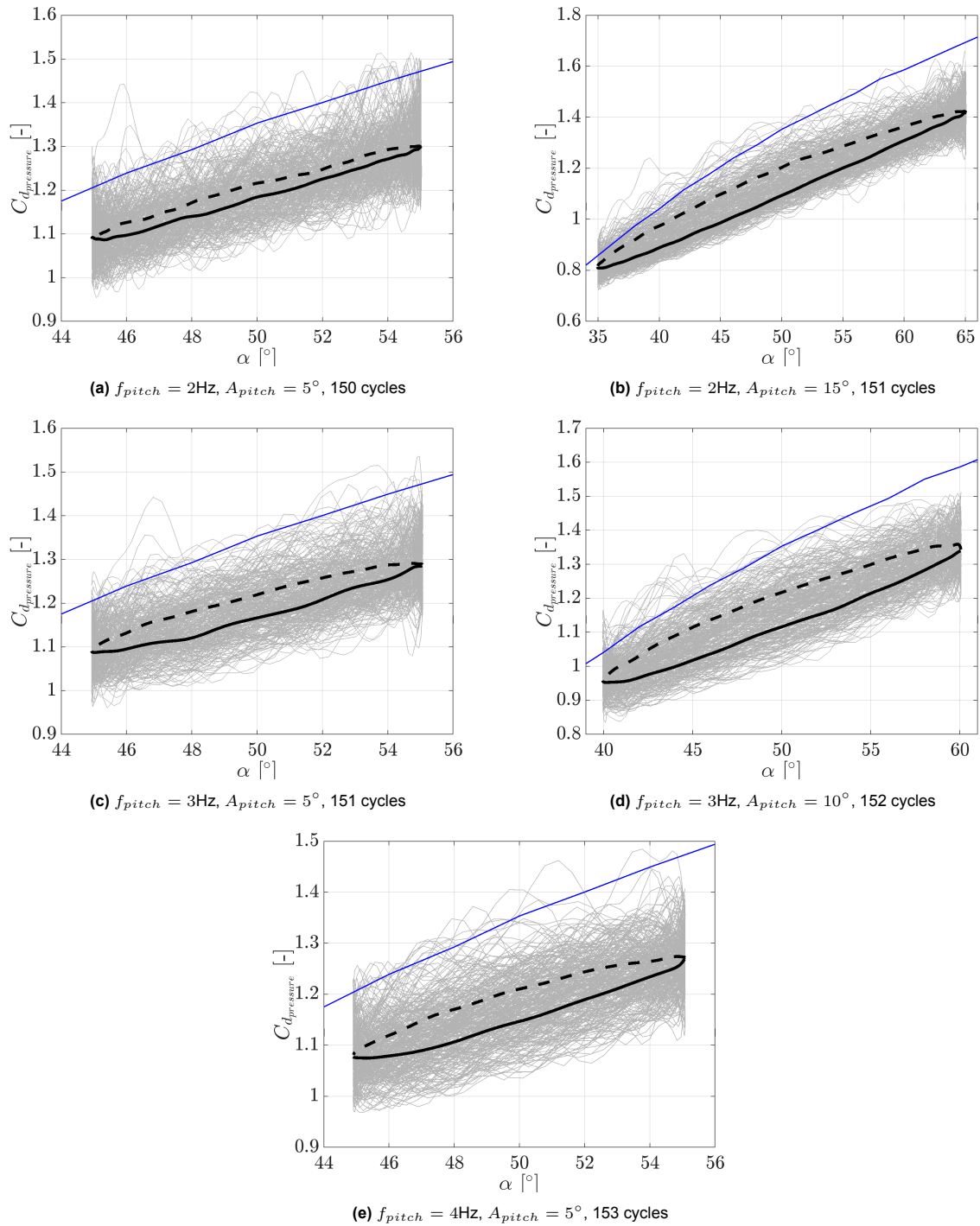


Figure 4.31: Comparison of $C_{d,pressure}$ for unsteady cases at $\alpha_{mean} = 50^\circ$ and $Re = 250k$. The black line represents the mean value, with the solid line representing the upstroke motion, the dashed line representing the downstroke motion and the blue line the values of static measurements.

The analysis of the $C_{d,pressure}$ vs α plots for the mean angle 90 cases reveals several noteworthy findings regarding the dynamic aerodynamic behaviour of the airfoil, particularly focusing on the hysteresis loops that are shown in Figure 4.32. One significant observation is that the $C_{d,pressure}$ values show minimal deviation over the entire range of angles of attack, mirroring the behaviour observed in the static plots. This alignment between dynamic and static plots indicates that the dynamic behaviour of the airfoil closely matches its static aerodynamic characteristics. Both the upstroke and downstroke phases exhibit consistent $C_{d,pressure}$ values, further emphasizing the similarity between dynamic and

static conditions.

In contrast to the mean angle 40 and 50 cases, where the hysteresis loops displayed distinct lower and upper stroke values, the mean angle 90 cases show no such division. This absence of distinct lower and upper stroke values suggests that the aerodynamic forces acting on the airfoil during pitching are more evenly distributed between the upstroke and downstroke phases. This phenomenon could be attributed to the dominance of shedding frequency phenomena in dictating the flow behaviour, with pitching having a lesser impact on the resulting $C_{d_{pressure}}$.

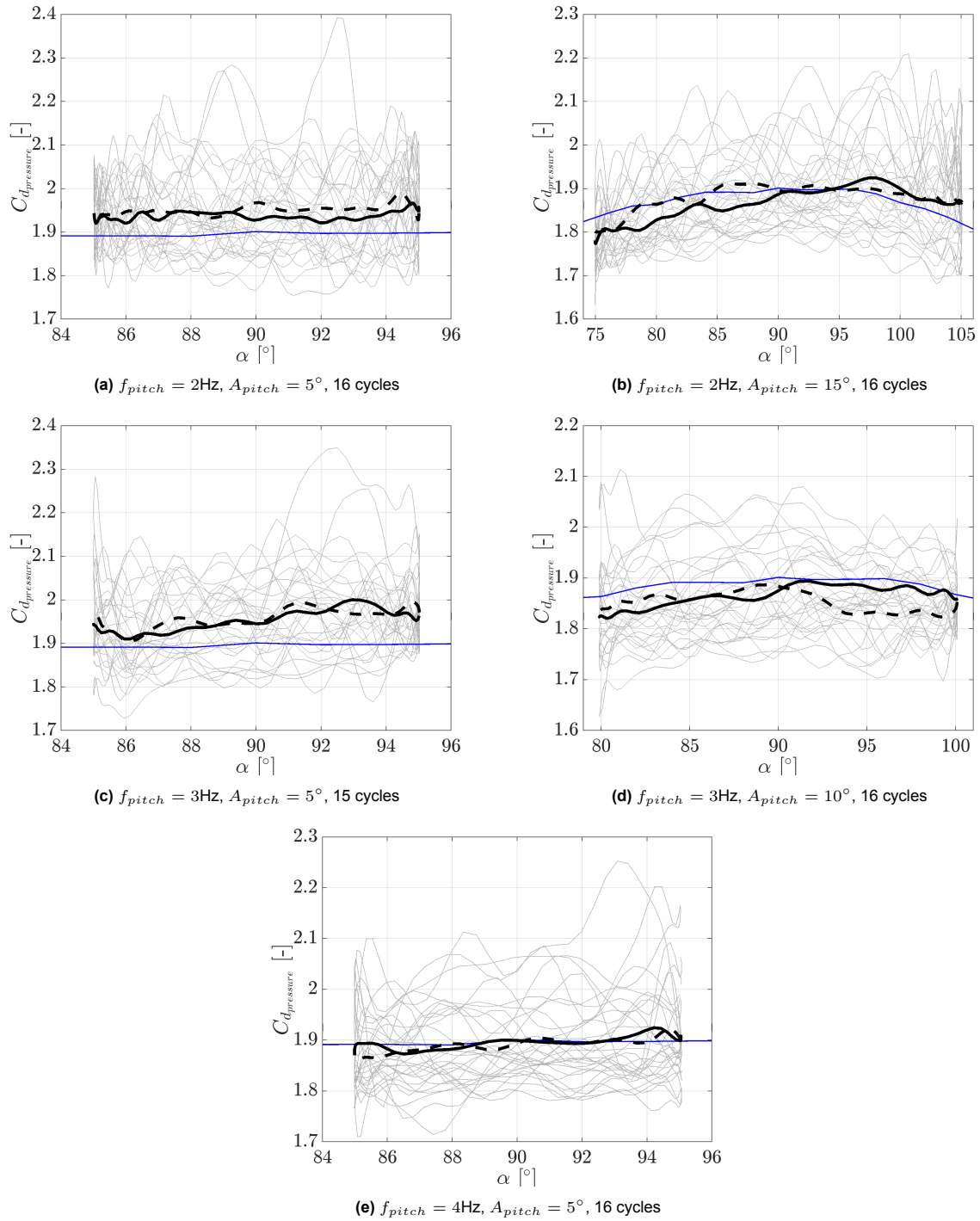


Figure 4.32: Comparison of $C_{d_{pressure}}$ for unsteady cases at $\alpha_{mean} = 90^\circ$ and $Re = 250k$. The black line represents the mean value, with the solid line representing the upstroke motion, the dashed line representing the downstroke motion and the blue line the values of static measurements.

In the plot depicted in Figure 4.33, we observe the differences between the upstroke and downstroke $C_{d_{pressure}}$ values for various frequency and amplitude cases. Each subplot represents different pitching frequencies, while the line colours represent different amplitudes. All plots share the same axes to facilitate comparison across data sets. On the y-axis, the difference between $C_{d_{pressure}}$ values is displayed for the same angle of attack, while the corresponding averaged alpha values are shown on the x-axis. Consistent with previous findings, we anticipate that increasing the pitching frequency or amplitude will lead to larger disparities between the upstroke and downstroke $C_{d_{pressure}}$ values. However, the 90° cases exhibit a unique pattern, with their $C_{d_{pressure}}$ values clustering closely together without a clear trend. This pattern is evident in the figure. Specifically, we observe that as the pitching frequency increases, the $C_{d_{pressure}}$ values for the green lines (representing $A_{amplitude} = 15^\circ$) also increase. Additionally, the difference between upstroke and downstroke $C_{d_{pressure}}$ values expands as the amplitude grows larger, consistent across all amplitude cases represented by the red and blue lines. This observation underscores the significant influence of $f_{pitching}$ and $A_{amplitude}$ on the $C_{d_{pressure}}$, highlighting their crucial role in shaping aerodynamic behaviour.

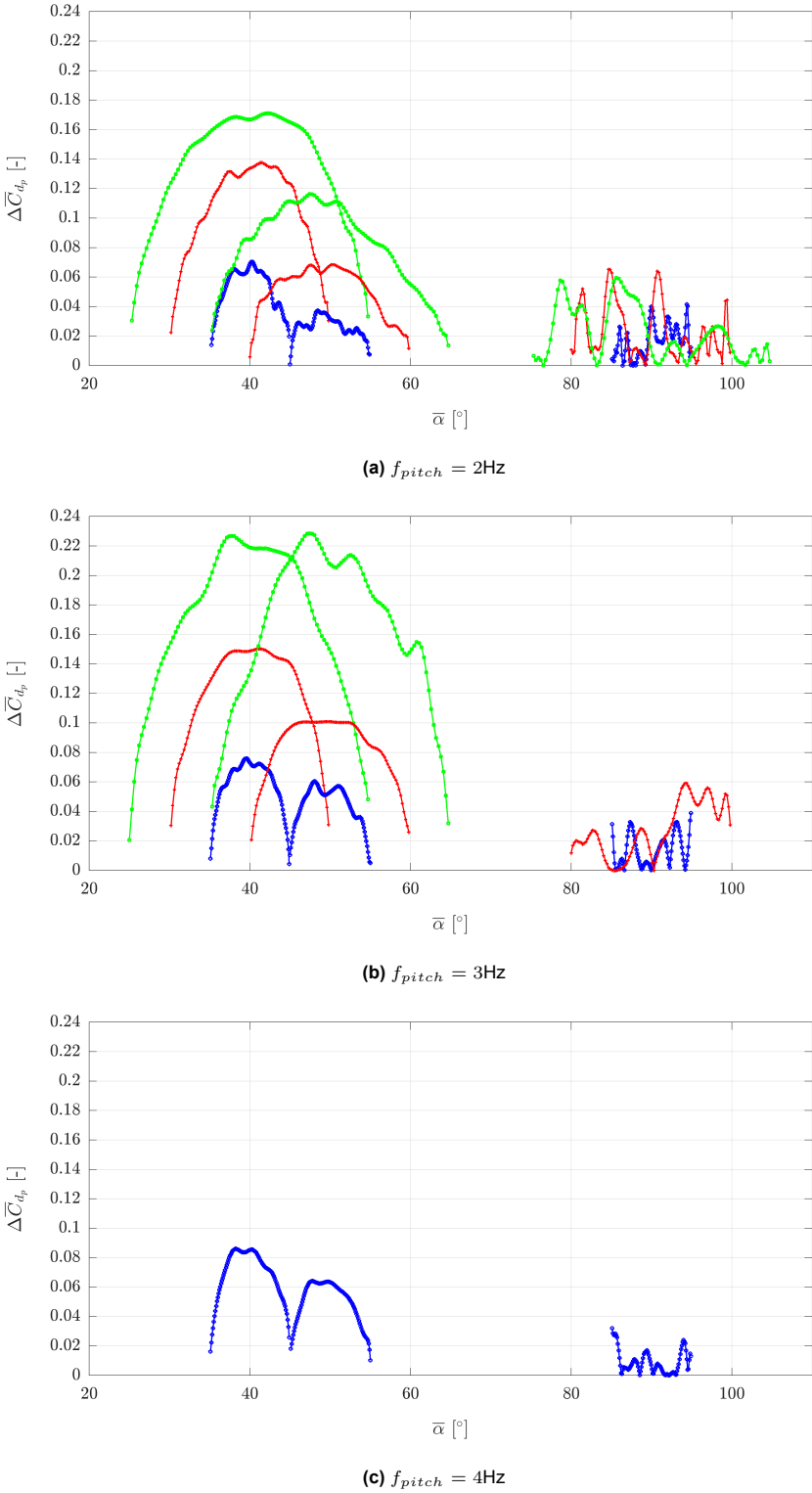


Figure 4.33: Comparison of $\Delta C_{d_{pressure}}$ at different pitching frequencies. Where the blue lines represent the $A_{amplitude} = 5^\circ$ cases, the red lines the $A_{amplitude} = 10^\circ$ and the green lines the $A_{amplitude} = 15^\circ$.

4.4.4. Lift Coefficient

The analysis of the C_l vs α plots for the mean angle of 40 cases provides several key insights into the dynamic aerodynamic behaviour of the airfoil, focusing on both individual cycles and the average of all cycles. These are shown in Figure 4.34. One notable observation is that the C_l plots for the 40° case align with the point where the maximum C_l occurs after the stall point. However, the hysteresis loop does not directly reflect this rounding top-shaped graph. Similar to the C_d plots, the C_l hysteresis loops exhibit a primarily linear tilt, with the upstroke consistently experiencing higher values than the downstroke. This linear tilt suggests a consistent aerodynamic response to changes in the angle of attack, albeit with variations due to dynamic effects.

Furthermore, increasing the pitching frequency results in more rounded hysteresis mean plots, indicating a smoother variation in C_l values throughout the pitching cycle. However, the effect of increasing amplitude becomes even more pronounced in the C_l plots. The hysteresis loops clearly demonstrate that amplitude has a significant impact on C_l values in unsteady aerodynamics, with larger amplitudes (Figure 4.34b and Figure 4.34d) leading to greater variations in lift coefficients.

Moreover, the individual lines in all plots exhibit extremely erratic behaviour, particularly evident in the lower amplitude cases. In these instances, the individual lines intersect and fluctuate around the mean values, which can pose challenges in visually differentiating between them.. This erratic behaviour underscores the complex and unpredictable nature of unsteady aerodynamic phenomena, highlighting the challenges in accurately predicting lift coefficients during dynamic motion.

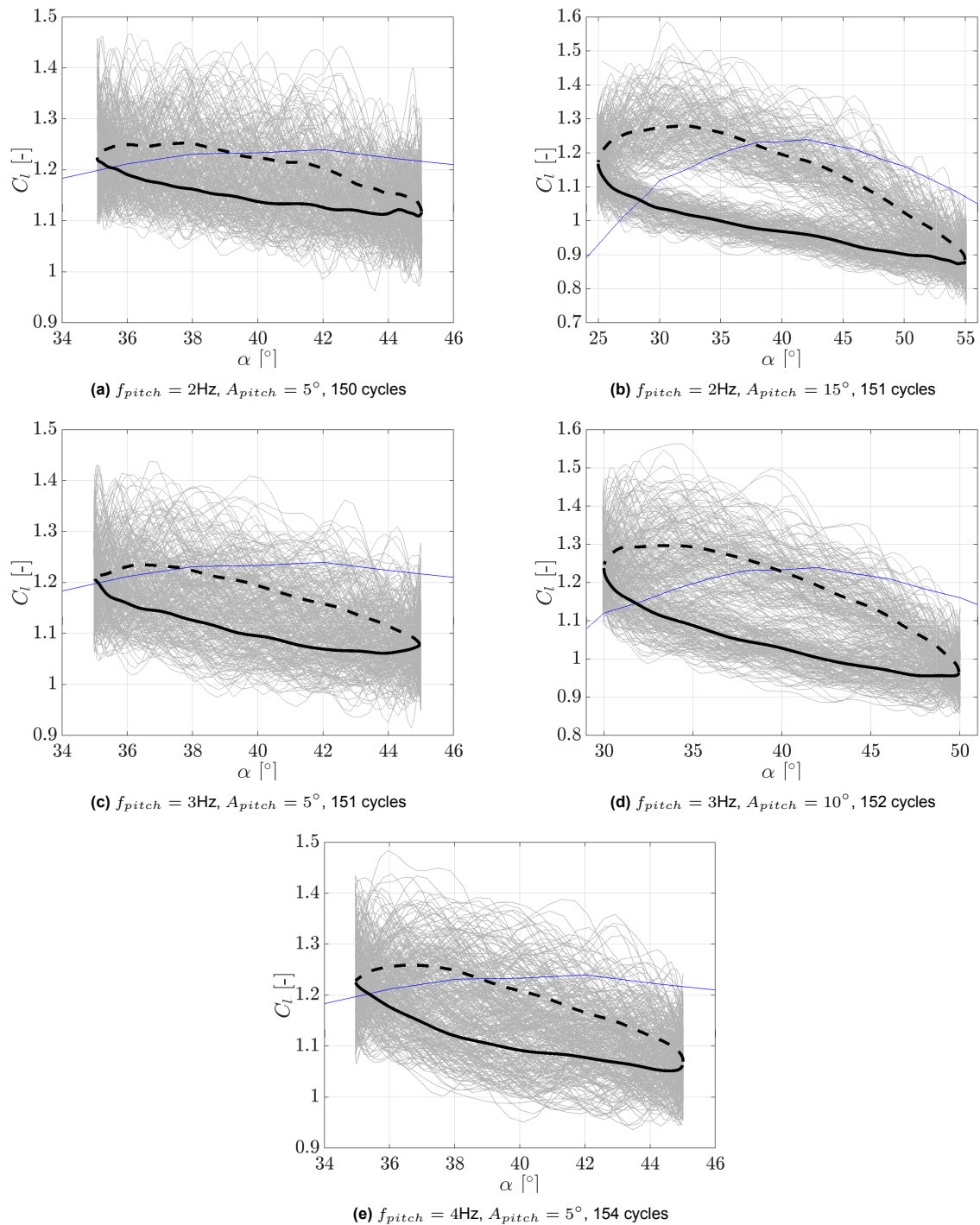


Figure 4.34: Comparison of C_l for unsteady cases at $\alpha_{mean} = 40^\circ$ and $Re = 250k$. The black line represents the mean value, with the solid line representing the upstroke motion, the dashed line representing the downstroke motion and the blue line the values of static measurements.

The analysis of C_l vs α hysteresis loops at the mean angle of 50° offers significant insights into the airfoil's dynamic aerodynamic behaviour, Figure 4.35, specifically emphasizing the role of individual cycles and the collective behaviour across all cycles. One prominent observation is that the hysteresis loops for the 50° cases appear less rounded and more flat disk-shaped compared to those of the 40° cases. This suggests that, in this regime, the influence of pitching on C_l is less significant. However, it is evident that the lower the energy of the pitching, for example Figure 4.34b and Figure 4.34c, the flatter the hysteresis curve appears, and the less deviant the C_l values are. This indicates a relationship

between pitching energy and the shape of the hysteresis curve, highlighting the importance of pitching dynamics in influencing lift generation.

Furthermore, the C_l values in these cases are notably lower compared to the static values, although the reason for this discrepancy remains unclear. However, the sloping of the hysteresis loops roughly matches the slope of the static values, suggesting a strong dependence on the overall mean angle in these cases. This consistency in slope indicates that the fundamental aerodynamic characteristics of the airfoil remain consistent between static and dynamic conditions, despite the differences in absolute C_l values.

Additionally, the individual hysteresis loops in this regime exhibit erratic behavior, with no clear signs of repetitiveness. Instead, they display erratic fluctuations, similar to those observed in previous cases. This erratic behaviour underscores the complex and unpredictable nature of unsteady aerodynamic phenomena, emphasizing the challenges in accurately predicting C_l values during dynamic motion.

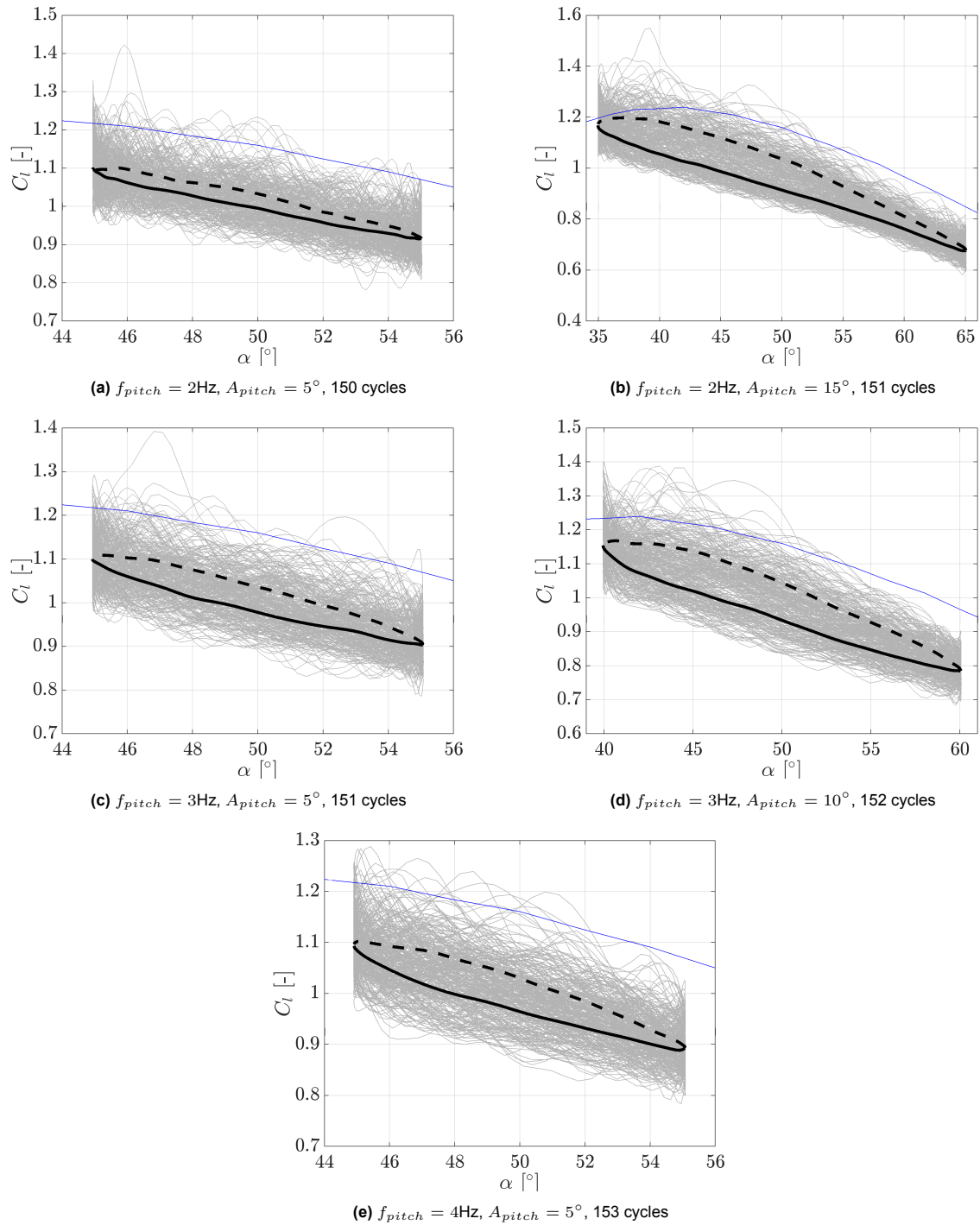


Figure 4.35: Comparison of C_l for unsteady cases at $\alpha_{mean} = 50^\circ$ and $Re = 250k$. The black line represents the mean value, with the solid line representing the upstroke motion, the dashed line representing the downstroke motion and the blue line the values of static measurements.

The analysis of the C_l versus α hysteresis loops for the mean angle of 90 cases, depicted in Figure 4.36, reveals the following insights into the airfoil's dynamic aerodynamic behaviour. This analysis considers both individual cycles and the average of all cycles. One notable observation is the close alignment of the hysteresis loops with the values obtained from static plots. This close correspondence indicates that C_l behaves quite linearly within this averaged regime, seemingly unaffected by the fluctuating nature of the flow. Although some individual lines show deviations from the linear trend, the overall trend closely resembles the static values. This suggests that, despite dynamic motion, the air-

foil's lift generation remains consistent and predictable, with the aerodynamic forces responding linearly to changes in angle of attack.

In addition, there is a noticeable trend where cases with lower amplitudes (such as Figure 4.36a, Figure 4.36c and Figure 4.36e) show more significant deviations from the static line compared to cases with higher amplitudes. This difference indicates that the behaviour of C_l becomes more consistent and aligned with each loop as the motion's amplitude increases. This phenomenon could suggest that C_l values are more affected by the motion's amplitude rather than the shedding frequency, with larger amplitudes playing a more dominant role in determining the flow behaviour.

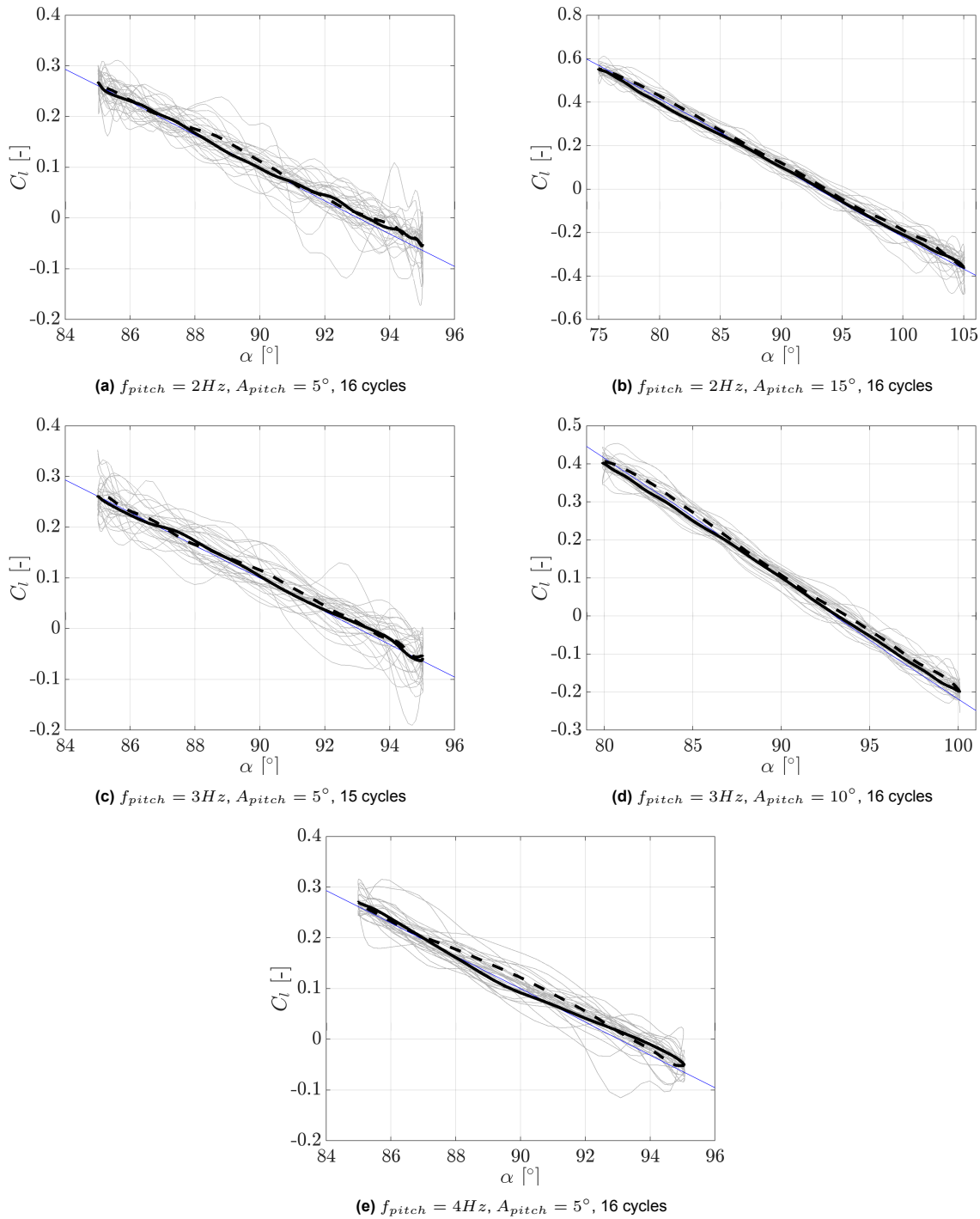


Figure 4.36: Comparison of C_l for unsteady cases at $\alpha_{mean} = 90^\circ$ and $Re = 250k$. The black line represents the mean value, with the solid line representing the upstroke motion, the dashed line representing the downstroke motion and the blue line the values of static measurements.

In a similar vein, Figure 4.37 shows the examination of the differences between the upstroke and downstroke C_l values yields insights into the dynamic aerodynamic behaviour of the airfoil. Analogous to the $C_{d_{pressure}}$ plots, we anticipate that increasing pitching frequency or amplitude will result in larger disparities between these C_l values. However, compared to the $C_{d_{pressure}}$ graphs, the C_l plots exhibit larger deviations, indicating a greater sensitivity of lift coefficients to changes in pitching dynamics. Notably, the curves become less rounded as the angle of attack exceeds 50° , suggesting a shift in aerodynamic behaviour at higher angles. Furthermore, consistent with the observations in the

$C_{d_{pressure}}$ plots, the 90° cases display minimal differences between upstroke and downstroke C_l values, indicative of a unique pattern where these values cluster closely together without a clear trend. This observation underscores the nuanced influence of $f_{pitching}$ and $A_{amplitude}$ on both drag and lift coefficients, emphasizing their critical role in shaping the aerodynamic characteristics of the airfoil across varying conditions.

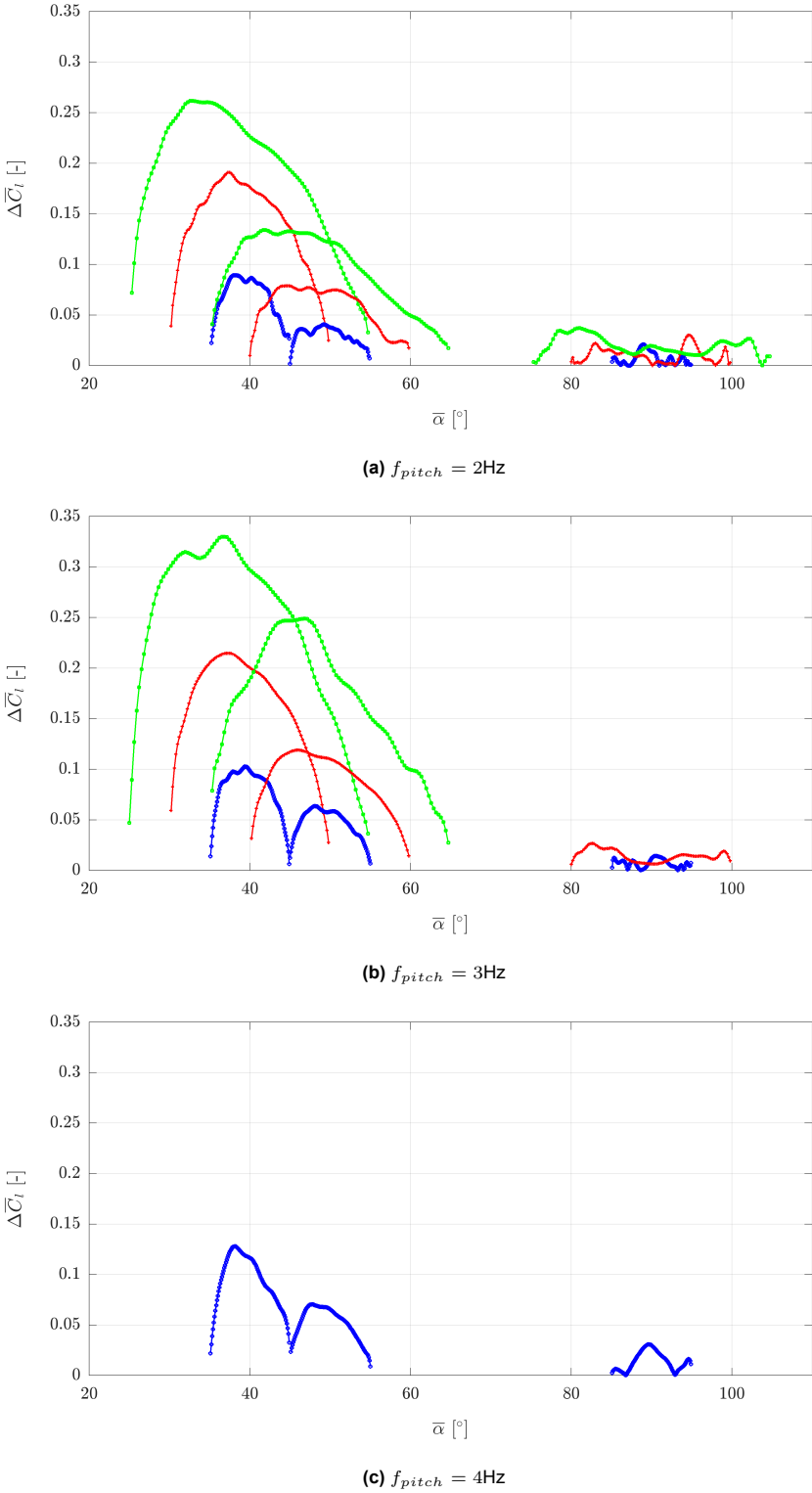


Figure 4.37: Comparison of ΔC_l at different pitching frequencies. Where the blue lines represent the $A_{amplitude} = 5^\circ$ cases, the red lines the $A_{amplitude} = 10^\circ$ and the green lines the $A_{amplitude} = 15^\circ$.

4.4.5. PIV

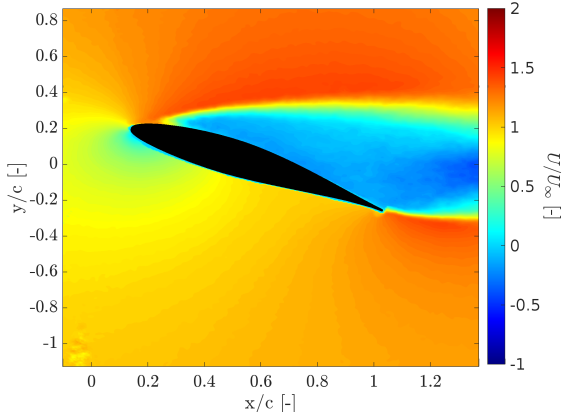
The PIV images for the highest amplitude pressure measurements have been analyzed using phase-locked PIV, and the images were averaged over 10 phases for each of the six cases. These six cases were chosen because the pressure measurement results indicated the greatest deviations in aerodynamic performance during the upstroke and downstroke. Understanding what happens in these scenarios is essential because they show significant differences compared to the results from static cases. This analysis helps to identify the underlying factors contributing to these deviations and provides insight into the dynamic behaviour of the system under these conditions. By investigating these extreme cases, we can better understand the aerodynamic characteristics and improve performance predictions for varying operational states.

The analysis of the phase-averaged PIV images for the case of $\alpha_{mean} = 40^\circ$, $f_{pitching} = 2\text{Hz}$, and $A_{pitching} = 15^\circ$ reveals several key observations. These are depicted in Figure 4.38. Generally, the dynamic averaged PIV images exhibit similarities to the static values, particularly in terms of the large wake region where the flow is either at zero or reversed. This indicates that despite the dynamic pitching, the overall wake characteristics maintain a consistent pattern with static conditions. However, notable differences emerge upon closer inspection of the upstroke and downstroke phases.

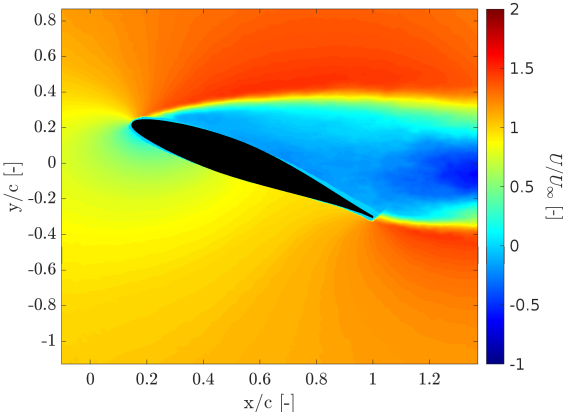
During the upstroke motion, there are relatively more pronounced darker blue spots in the PIV images. These can clearly be seen in Figure 4.38a and Figure 4.38d. These spots indicate areas of stronger reverse flow compared to the downstroke averages. This suggests that during the upstroke, the flow separation is more intense, leading to regions of higher reverse velocity within the wake. The increased reverse flow during the upstroke could be attributed to the increasing angle of attack, which enhances flow separation and intensifies the wake region's reverse flow characteristics.

Conversely, the downstroke phase exhibits a different pattern. The boundary between the deep wake and the outer flow appears larger and more stretched in the downstroke images compared to the upstroke. This can best be seen when comparing Figure 4.38c and Figure 4.38h. This indicates that while the upstroke experiences more intense reverse flow in localized areas, the downstroke phase has a more extended wake boundary. This could be due to the decreasing angle of attack during the downstroke, which might reduce the intensity of flow separation but spread the wake over a larger area.

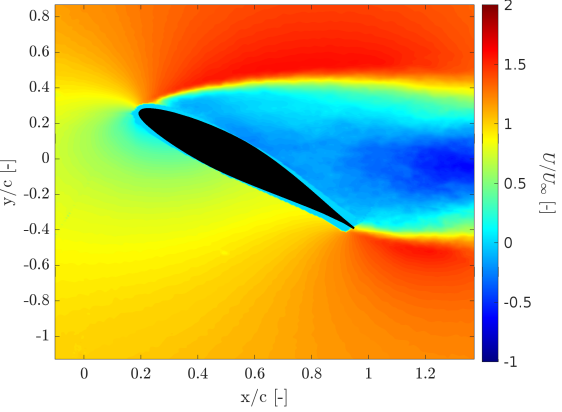
These observations highlight that the wake aerodynamics are not completely identical between the upstroke and downstroke motions. This could also be the reason why the up and downstroke are not experiencing the same drag and lift coefficient on average as shown in the previous pressure measurement results. The differences in reverse flow intensity and wake boundary extension suggest that the dynamic effects of pitching introduce asymmetries in the flow field that are not present in the static case. The phase-averaged PIV images thus provide a deeper understanding of how dynamic pitching influences the wake structure, revealing that the flow characteristics are modulated by the pitching motion's phase.



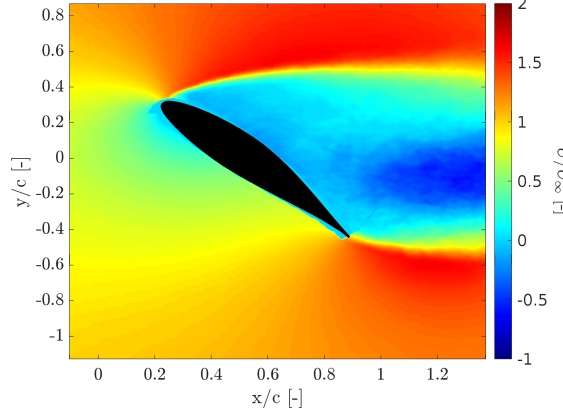
(a) $\alpha = 28^\circ$ (upstroke)



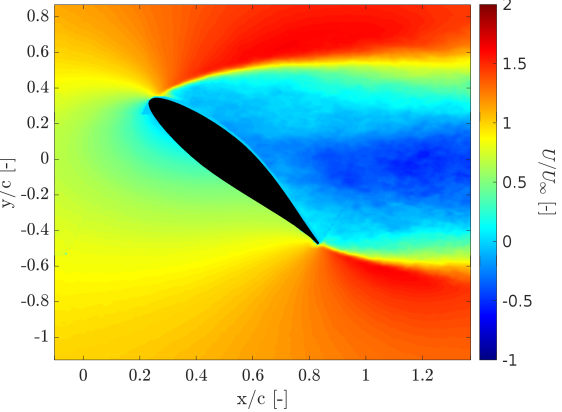
(b) $\alpha = 32^\circ$ (upstroke)



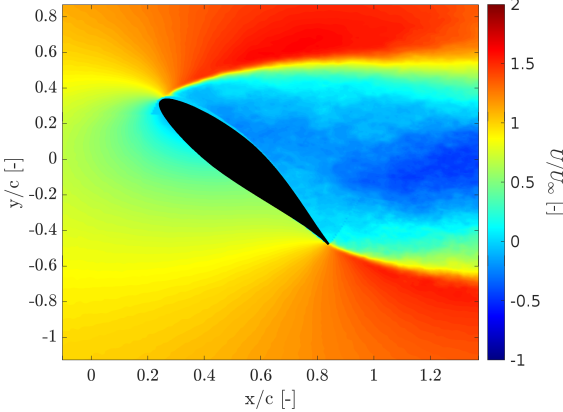
(c) $\alpha = 42^\circ$ (upstroke)



(d) $\alpha = 49^\circ$ (upstroke)



(e) $\alpha = 54^\circ$ (upstroke)



(f) $\alpha = 54^\circ$ (downstroke)

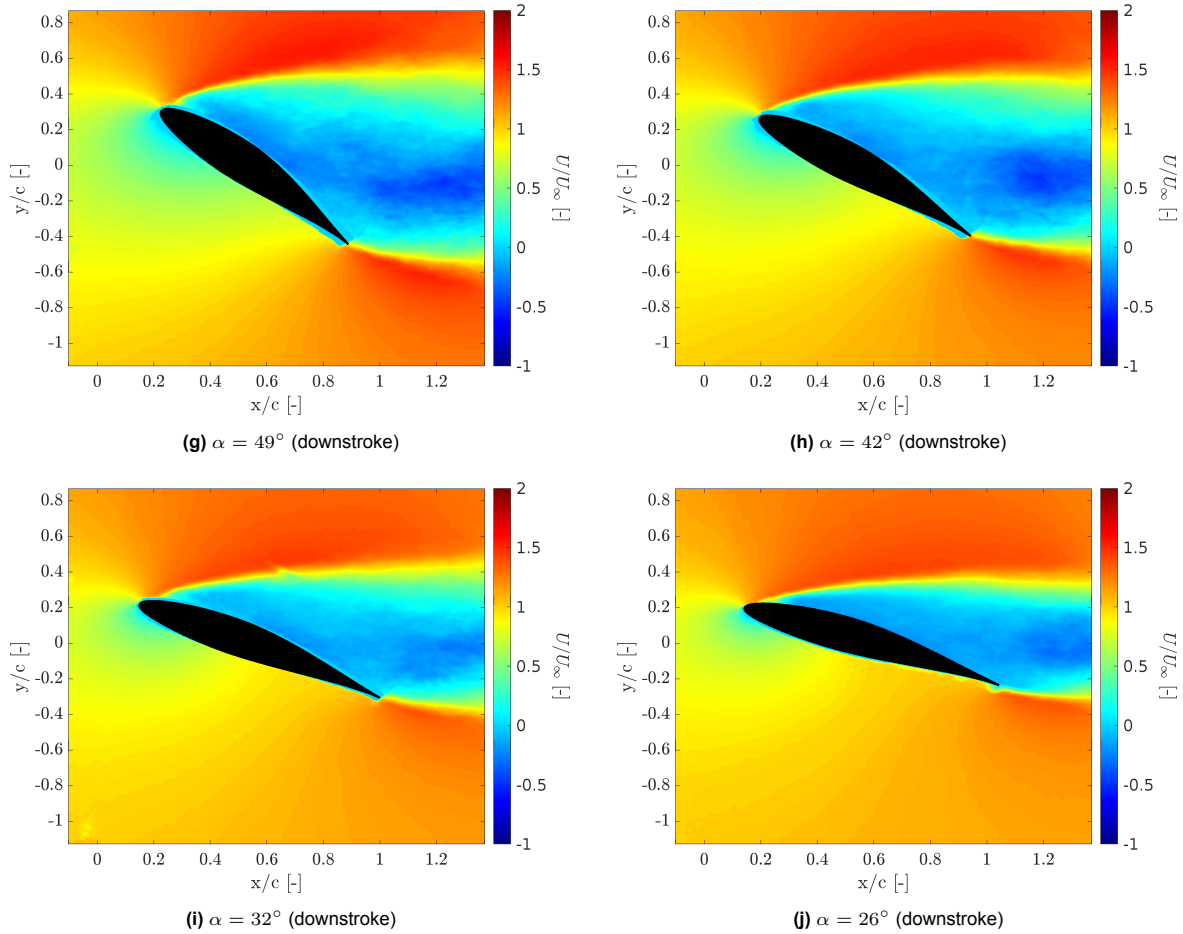


Figure 4.38: Phase locked averaged flow fields (U/U_∞) for dynamic condition with $\alpha_{mean} = 40^\circ$, $f_{pitching} = 2\text{Hz}$ and $A_{pitching} = 15^\circ$.

The analysis of the phase-averaged PIV images for the case of $\alpha_{mean} = 40^\circ$, $f_{pitching} = 3\text{Hz}$, and $A_{pitching} = 10^\circ$, Shown in Figure 4.39, yields results that are broadly consistent with the previous case ($\alpha_{mean} = 40^\circ$, $f_{pitching} = 2\text{Hz}$, and $A_{pitching} = 15^\circ$), while also exhibiting specific nuances due to the differences in pitching frequency and amplitude.

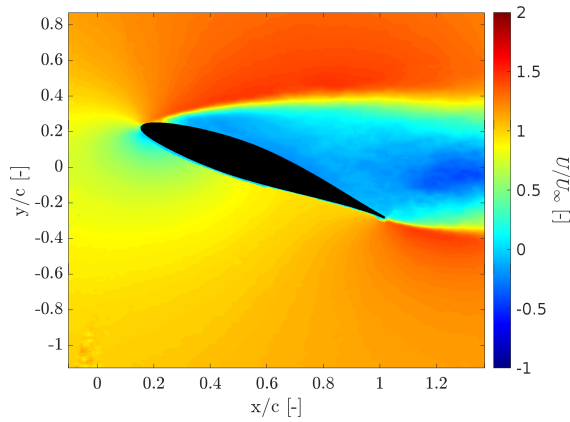
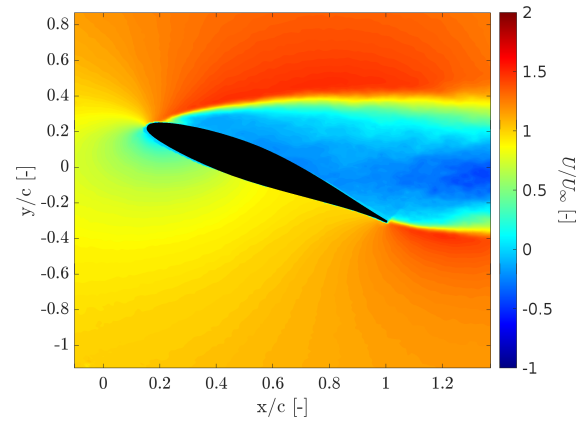
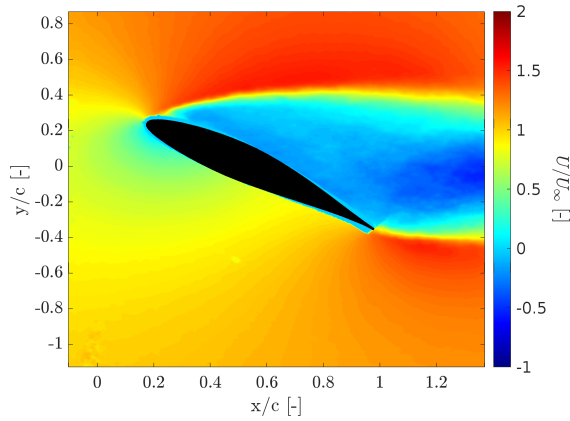
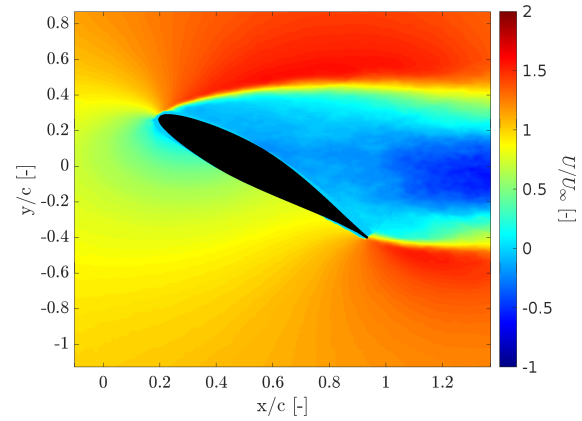
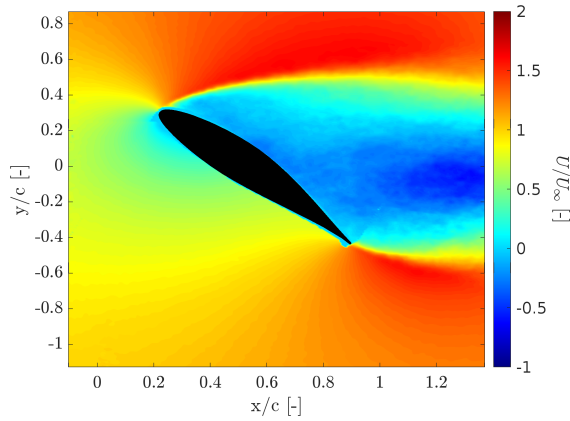
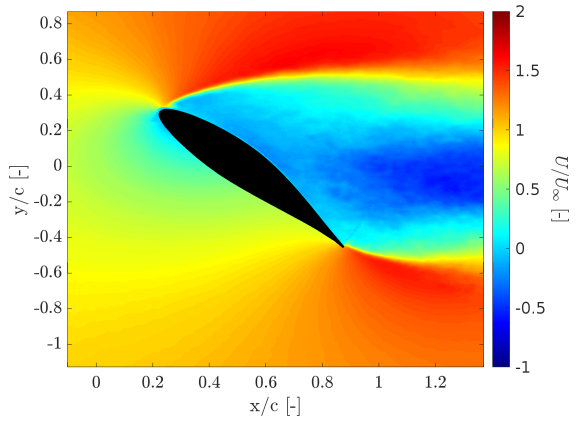
As observed in the previous analysis, the dynamic averaged PIV images for this case also display a large wake region where the flow is either zero or reversed, maintaining a visual similarity to static flow conditions. This consistency suggests that, despite variations in pitching parameters, the general wake structure remains dominated by significant flow separation and reverse flow in both dynamic and static conditions.

During the upstroke motion, the PIV images again reveal more pronounced darker blue spots, indicating areas of stronger reverse flow. This is consistent with the findings from the previous case and highlights that increasing the angle of attack during the upstroke continues to intensify flow separation, leading to regions of higher reverse velocity within the wake. This intensified reverse flow is a direct consequence of dynamic pitching, which exacerbates flow separation compared to static conditions.

Conversely, the downstroke phase for this case also shows a larger and more stretched wake boundary, similar to the previous case. This extended wake boundary during the downstroke suggests that, even with a higher pitching frequency of 3 Hz, the decreasing angle of attack reduces the intensity of flow separation but spreads the wake over a larger area. The stretched boundary indicates that the wake retains its coherence over a larger spatial extent, albeit with reduced intensity compared to the upstroke.

The higher pitching frequency and lower amplitude in this case introduce additional nuances. The increased frequency means the airfoil experiences changes in angle of attack more rapidly, which could lead to quicker transitions between upstroke and downstroke phases. This rapid transition might

smooth out some of the more extreme variations seen at lower frequencies, leading to a slightly more homogenized wake structure. However, the fundamental asymmetry between upstroke and downstroke observed in the previous case remains evident.

**(a)** $\alpha = 30^\circ$ **(b)** $\alpha = 33^\circ$ (upstroke)**(c)** $\alpha = 37^\circ$ (upstroke)**(d)** $\alpha = 43^\circ$ (upstroke)**(e)** $\alpha = 48^\circ$ (upstroke)**(f)** $\alpha = 50^\circ$

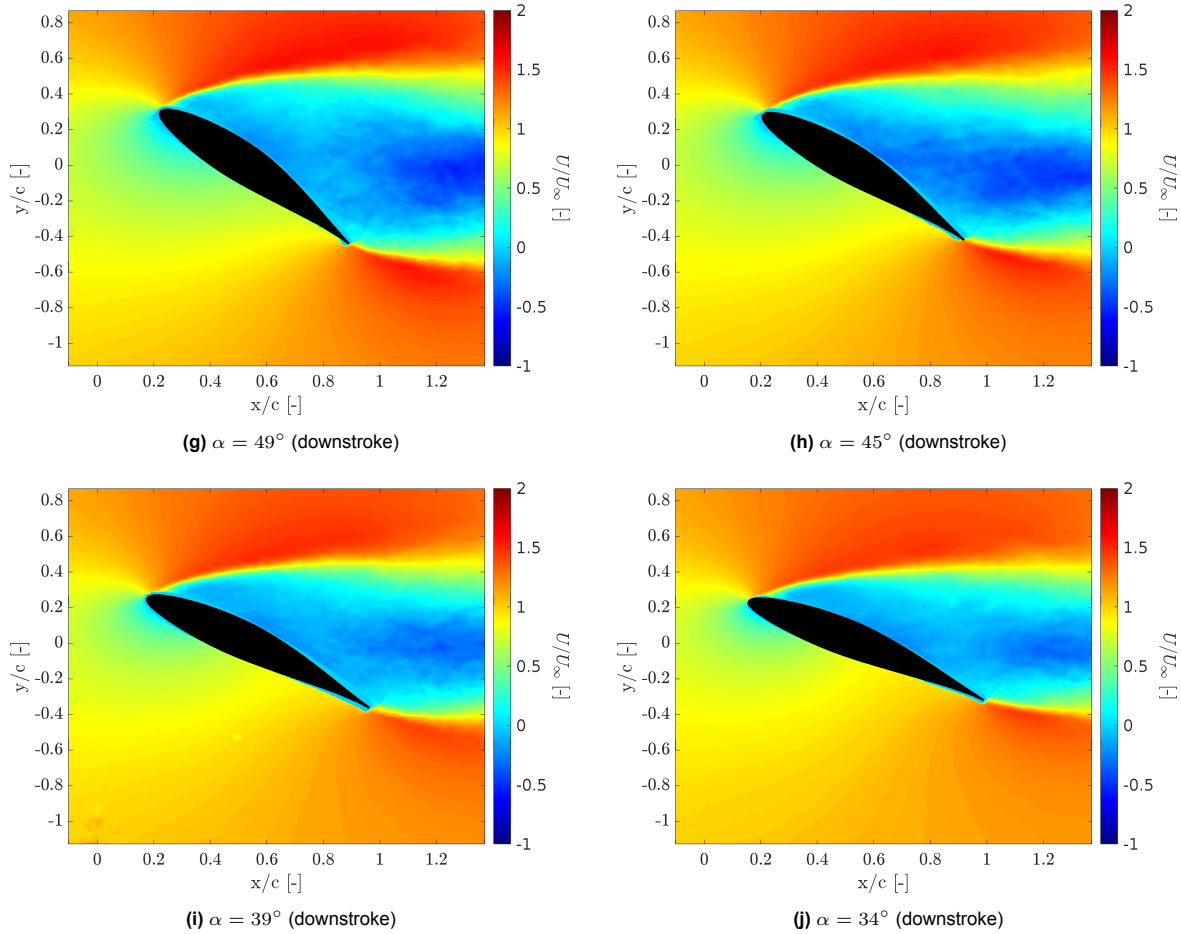
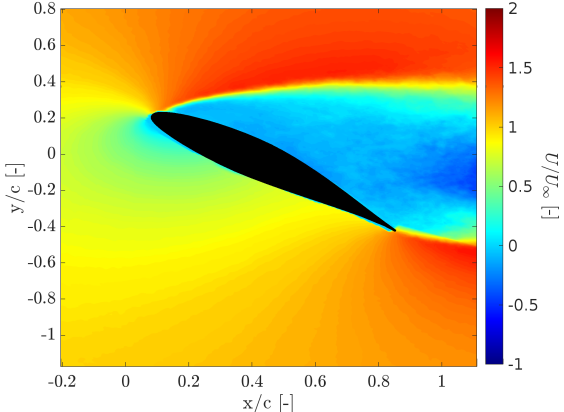


Figure 4.39: Phase locked averaged flow fields (U/U_∞) for dynamic condition with $\alpha_{mean} = 40^\circ$, $f_{pitching} = 3\text{Hz}$, and $A_{pitching} = 10^\circ$.

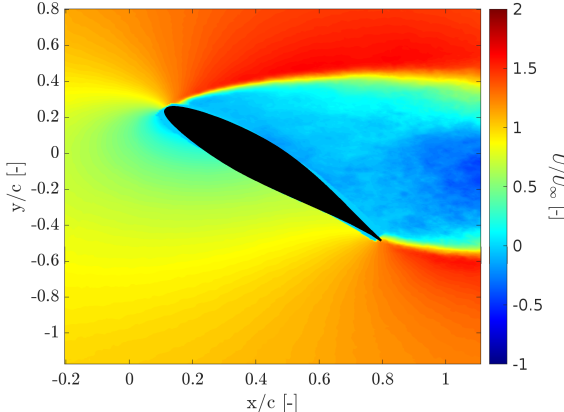
One prominent observation for the case of $\alpha_{mean} = 50^\circ$, $f_{pitching} = 2\text{Hz}$, is the difference in the wake characteristics between the upstroke and downstroke motions, depicted in Figure 4.40. As with previous cases, the upstroke phase exhibits darker blue regions in the wake, indicating stronger reverse flow compared to the downstroke phase. This suggests that during the upstroke, there is more intense flow separation and higher levels of reverse velocity within the wake. Conversely, the downstroke phase shows relatively lighter blue regions in the wake, implying less intense reverse flow compared to the upstroke. This difference in reverse flow intensity between upstroke and downstroke motions influences the aerodynamic performance, with the downstroke potentially generating less drag due to reduced flow separation.

Furthermore, the boundary of the wake appears more stretched in the upstroke-averaged plots compared to the downstroke-averaged plots. This suggests that during the upstroke, the wake boundary extends over a larger spatial area compared to the downstroke. The extended wake boundary during the upstroke phase indicates a broader region of disturbed flow behind the airfoil, potentially leading to increased drag and reduced aerodynamic efficiency. Conversely, the more compact wake boundary during the downstroke phase indicates a more confined region of disturbed flow, which may contribute to reduced drag and improved aerodynamic performance.

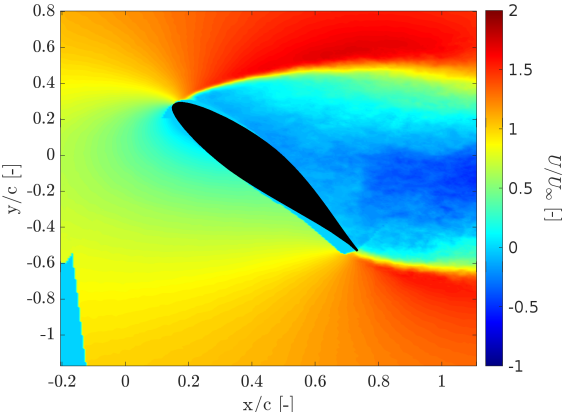
Overall, these findings highlight the complex interplay between dynamic pitching motions, angle of attack, and wake characteristics in shaping the airfoil's aerodynamic behaviour. The differences observed between upstroke and downstroke phases underscore the asymmetric nature of the flow field and its influence on lift and drag generation. Additionally, the stretching of the wake boundary during the upstroke phase suggests a broader wake structure that could contribute to increased drag.



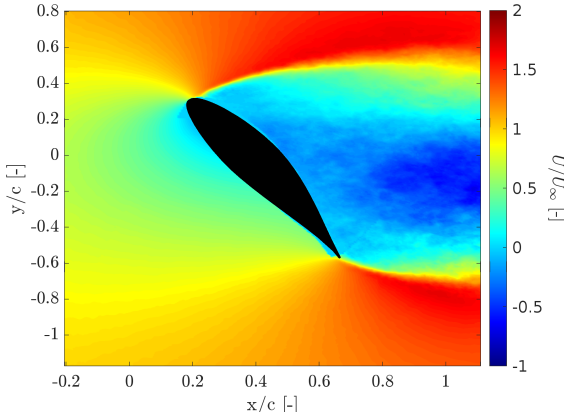
(a) $\alpha = 40^\circ$ (upstroke)



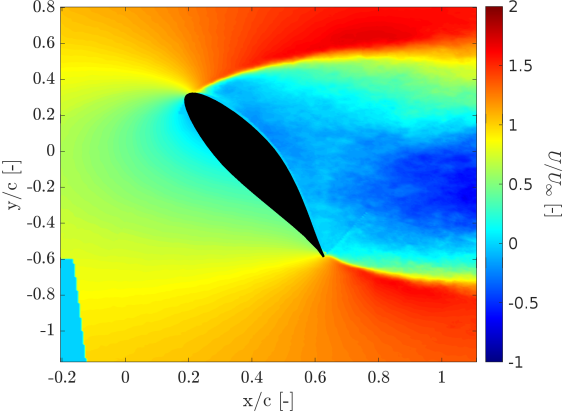
(b) $\alpha = 48^\circ$ (upstroke)



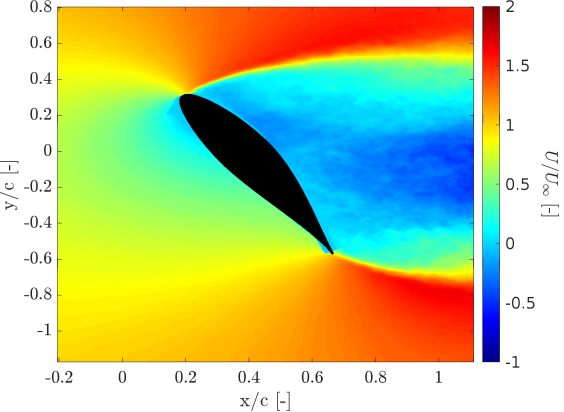
(c) $\alpha = 55^\circ$ (upstroke)



(d) $\alpha = 62^\circ$ (upstroke)



(e) $\alpha = 65^\circ$



(f) $\alpha = 62^\circ$ (downstroke)

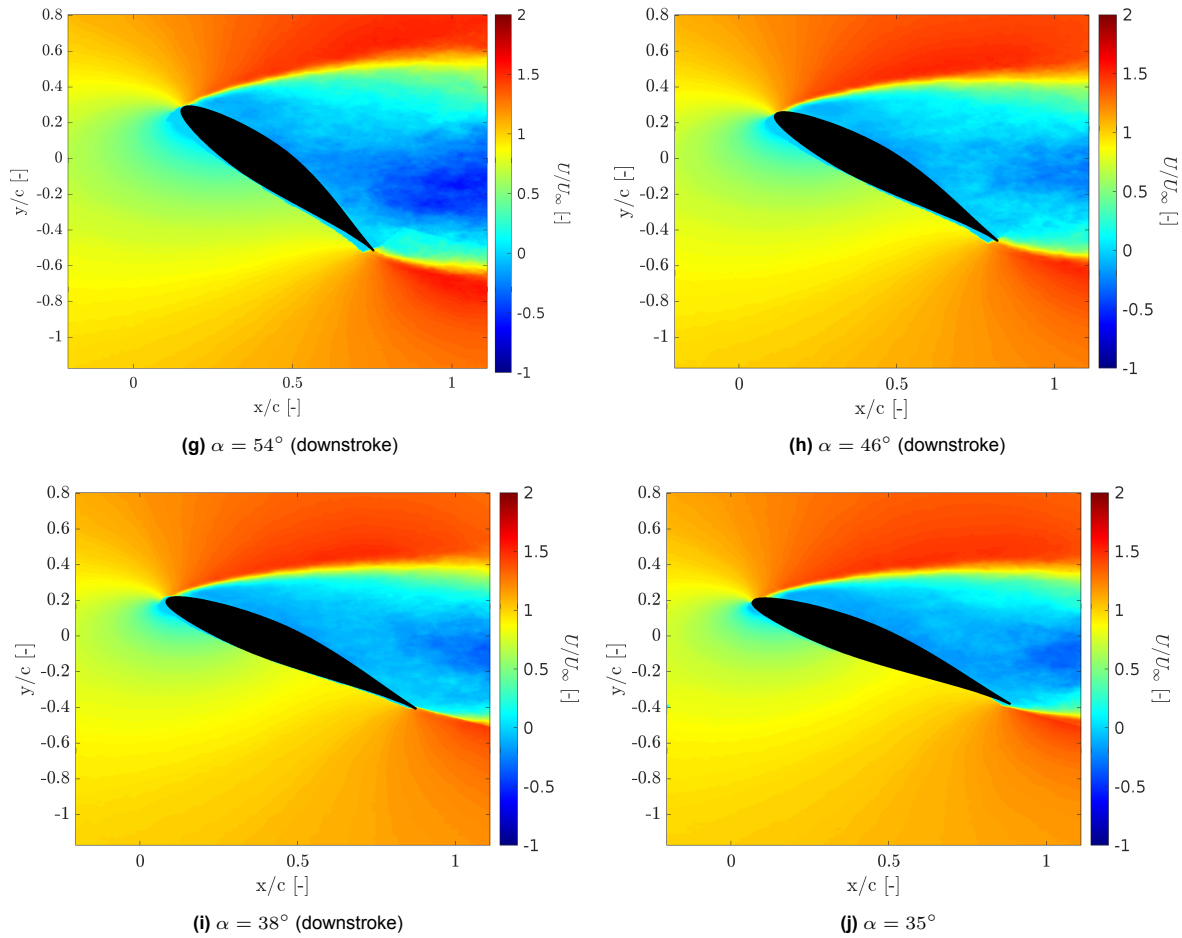
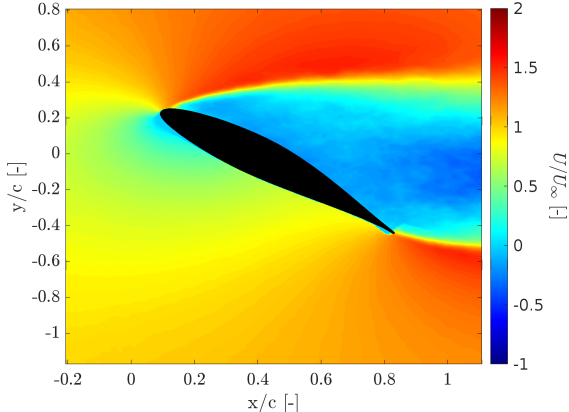


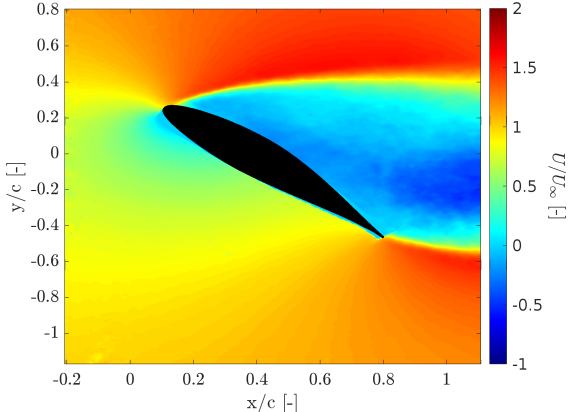
Figure 4.40: Phase locked averaged flow fields (U/U_∞) for dynamic condition with $\alpha_{mean} = 50^\circ$, $f_{pitching} = 2\text{Hz}$ and $A_{pitching} = 15^\circ$.

Similar to the previous case, the case of $\alpha_{mean} = 50^\circ$, $f_{pitching} = 3\text{Hz}$, and $A_{pitching} = 10^\circ$ distinct differences are observed between the upstroke and downstroke phases in the wake characteristics. This can be seen by the images depicted in Figure 4.41. Once again, the upstroke phase exhibits darker blue regions in the wake, indicating stronger reverse flow compared to the downstroke phase. This suggests that during the upstroke, there is more intense flow separation and higher levels of reverse velocity within the wake. Conversely, the downstroke phase shows relatively lighter blue regions in the wake, indicating less intense reverse flow compared to the upstroke. This discrepancy in reverse flow intensity between the two phases suggests a notable asymmetry in the wake dynamics, which likely influences the aerodynamic performance of the airfoil.

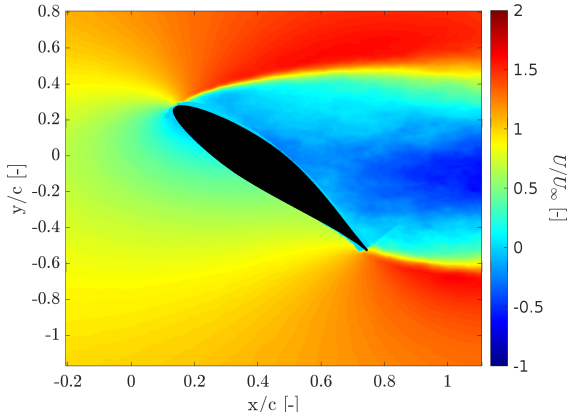
Furthermore, the boundary of the wake appears to be more stretched in the upstroke-averaged plots compared to the downstroke-averaged plots, consistent with the findings from the previous case. This suggests that during the upstroke, the wake boundary extends over a larger spatial area compared to the downstroke, indicating a broader region of disturbed flow behind the airfoil. Conversely, the more compact wake boundary during the downstroke phase suggests a more confined region of disturbed flow.



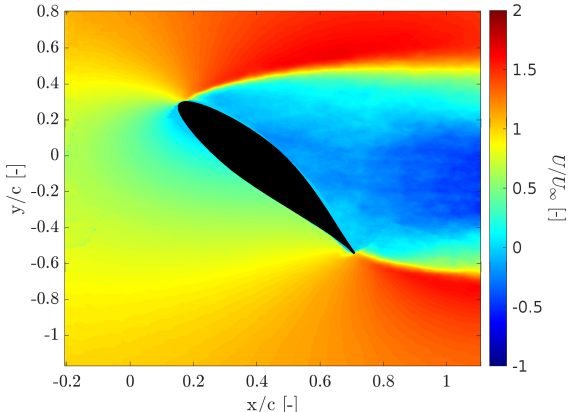
(a) $\alpha = 43^\circ$ (upstroke)



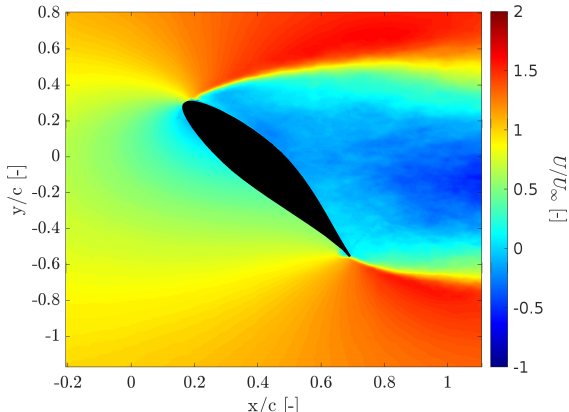
(b) $\alpha = 47^\circ$ (upstroke)



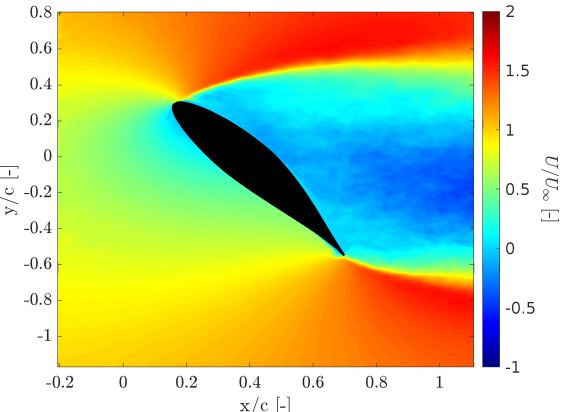
(c) $\alpha = 53^\circ$ (upstroke)



(d) $\alpha = 57^\circ$ (upstroke)



(e) $\alpha = 60^\circ$



(f) $\alpha = 58^\circ$ (downstroke)

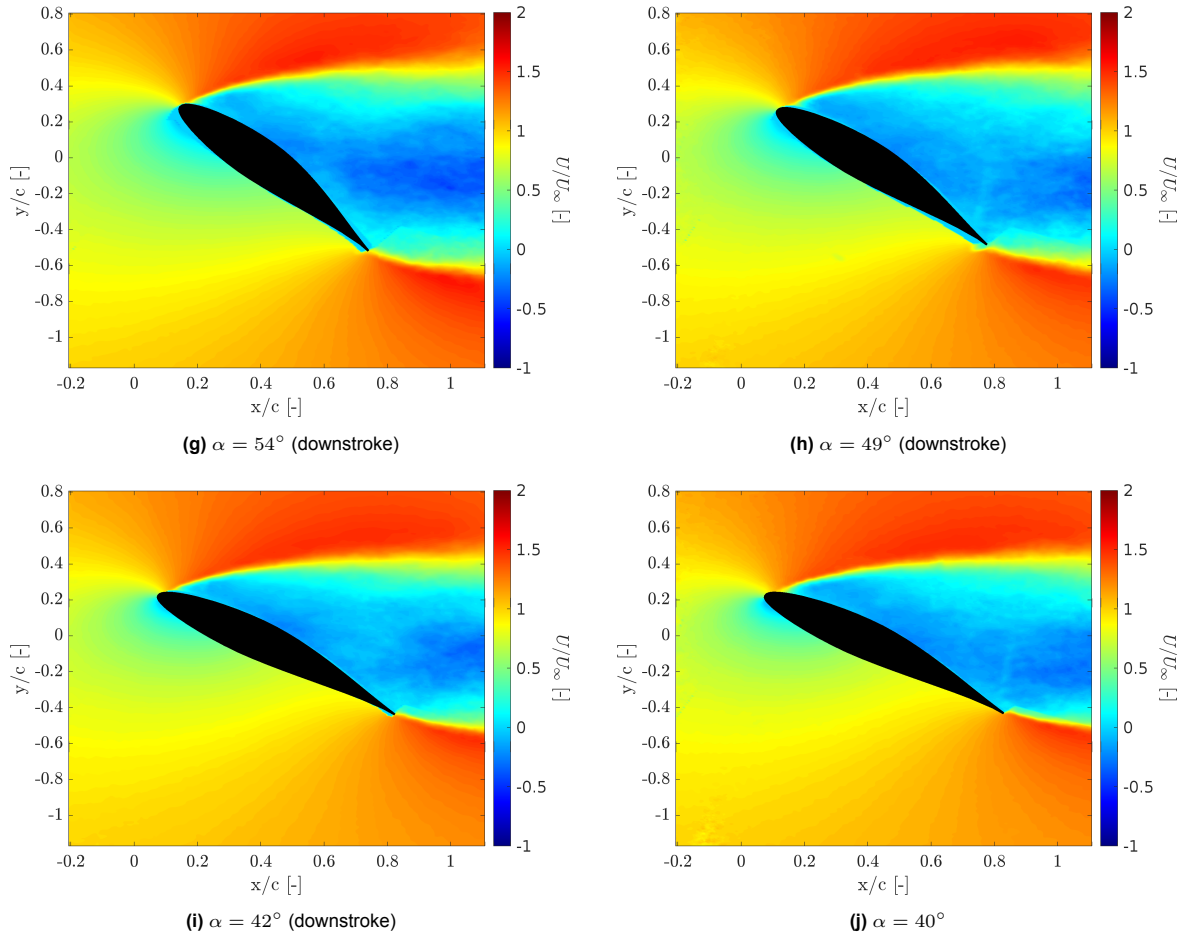
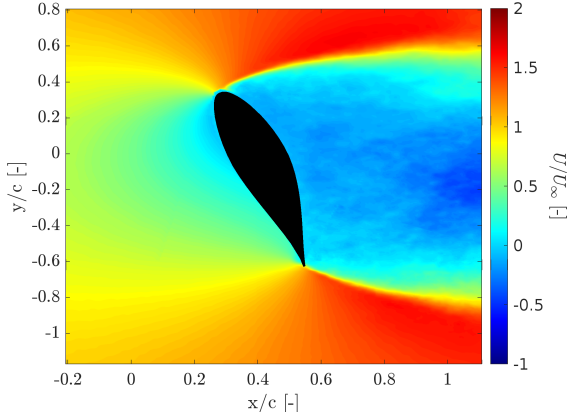


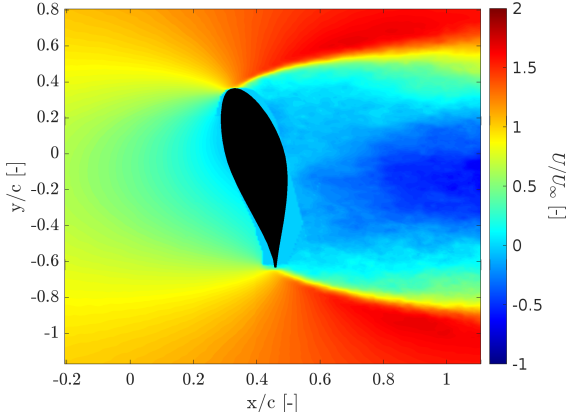
Figure 4.41: Phase locked averaged flow fields (U/U_∞) for dynamic condition with $\alpha_{mean} = 50^\circ$, $f_{pitching} = 3\text{Hz}$, and $A_{pitching} = 10^\circ$.

Contrary to the observations in the 40° and 50° cases, where the downstroke exhibited lower values of reverse flow compared to the upstroke, the images for the case of $\alpha_{mean} = 90^\circ$, $f_{pitching} = 2\text{Hz}$, and $A_{pitching} = 15^\circ$ present a different scenario. These are illustrated in Figure 4.43. The phase-averaged PIV images indicate that the differences in reverse flow intensity between the upstroke and downstroke phases are not as pronounced as observed in the lower angle cases. This observation is consistent with the findings from the pressure data analysis, which showed that the values for drag coefficient ($C_{d_{pressure}}$) and lift coefficient (C_l) are less affected by the upstroke or downstroke motions compared to the 40° or 50° cases. The images suggest that at this high angle of attack, the influence of pitching motion on altering the flow behaviour is relatively diminished, emphasizing the dominant role of the airfoil's high angle of attack in shaping the flow field.

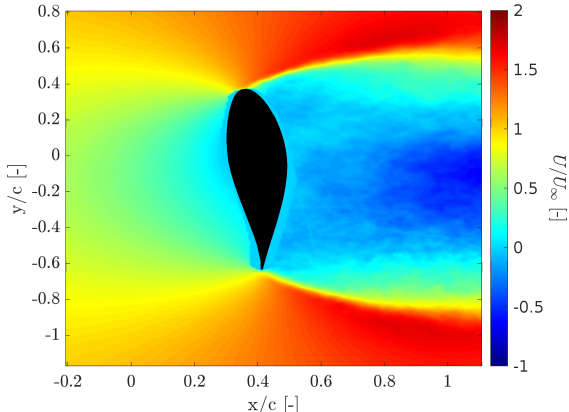
Moreover, at a pitching frequency of 2 Hz, the flow characteristics around the airfoil at 90° angle of attack appear similar to the static values. This suggests that the pitching motion has less influence on altering the flow behaviour in this high-angle 90° regime. The consistency between the dynamic phase-averaged PIV images and the static values further supports this conclusion, which is visualized by comparing Figure 4.42c and Figure 4.42c to Figure 4.13d. This indicates that the flow dynamics remain relatively similar even with the introduction of pitching motion at a moderate frequency.



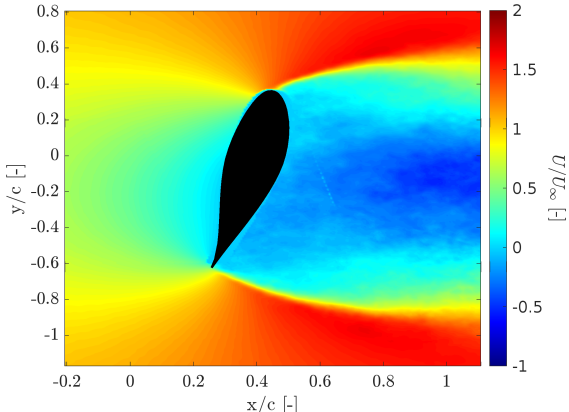
(a) $\alpha = 76^\circ$ (upstroke)



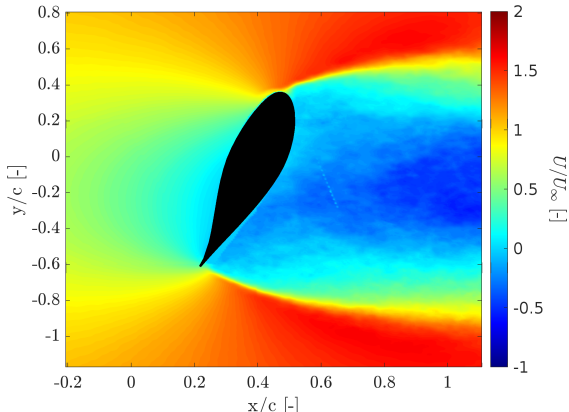
(b) $\alpha = 83^\circ$ (upstroke)



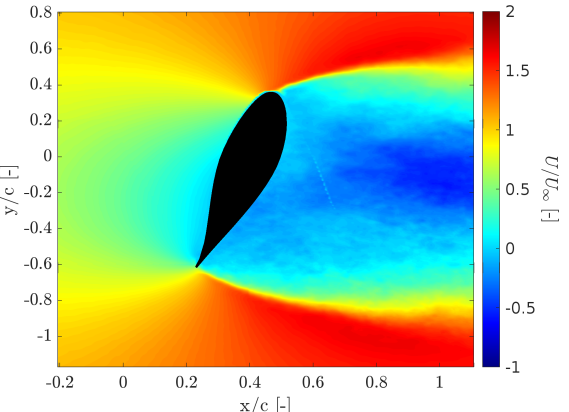
(c) $\alpha = 87^\circ$ (upstroke)



(d) $\alpha = 101^\circ$ (upstroke)



(e) $\alpha = 104^\circ$ (upstroke)



(f) $\alpha = 104^\circ$ (downstroke)

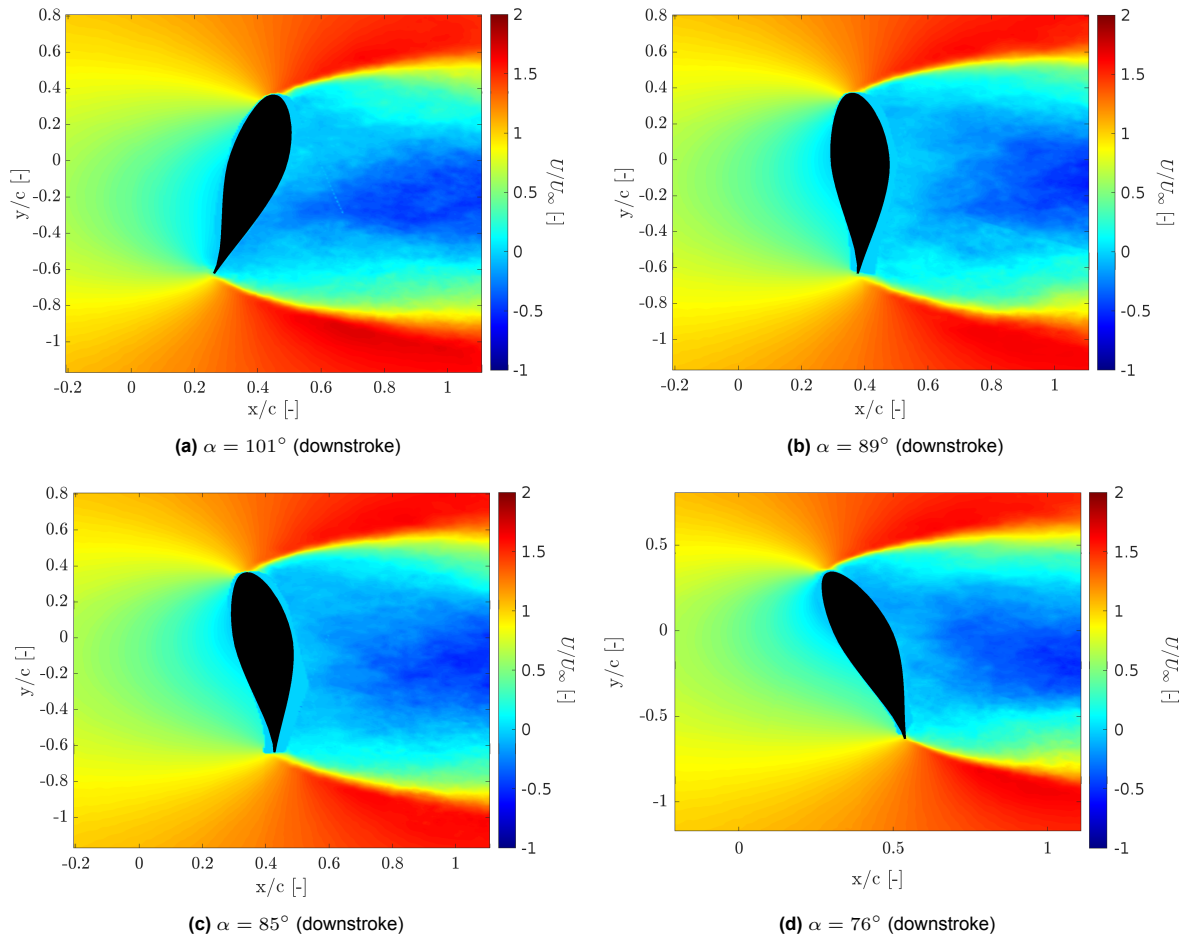
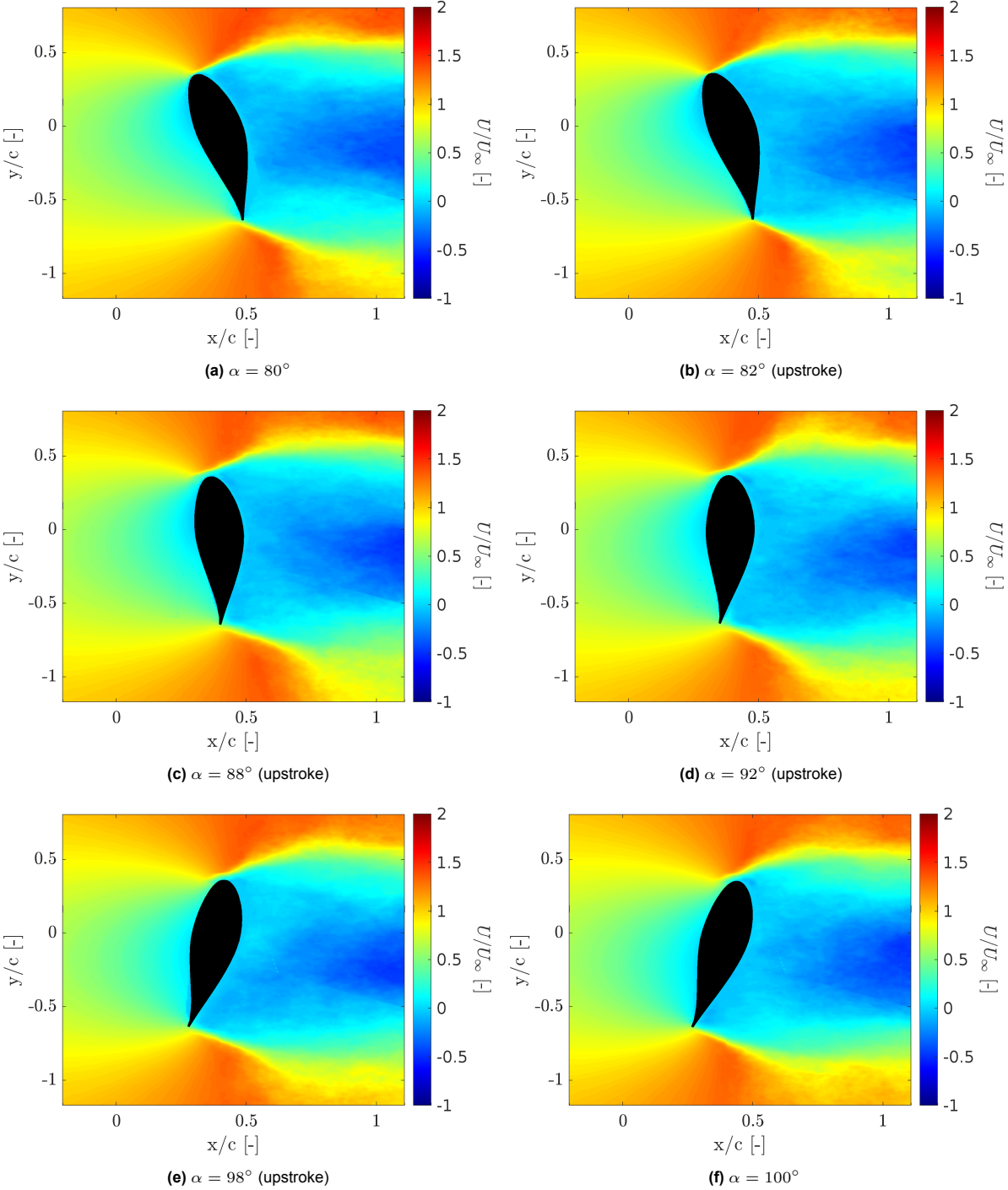


Figure 4.43: Phase locked averaged flow fields (U/U_∞) for dynamic condition with $\alpha_{mean} = 90^\circ$, $f_{pitching} = 2\text{Hz}$ and $A_{pitching} = 15^\circ$.

In contrast to the previous case, the averaged PIV plots for the case of $\alpha_{mean} = 90^\circ$, $f_{pitching} = 3\text{Hz}$, and $A_{pitching} = 10^\circ$ show significant alterations in the flow behaviour around the airfoil. These are exhibited in Figure 4.44. Particularly striking is the pronounced impact of the more frequent pitching motion on the area in front of the airfoil during each phase. The extensive yellow area observed in front indicates a higher disruption of the flow due to the more frequent pitching. Furthermore, the wake behind the airfoil exhibits notable changes, appearing wider and encompassing a larger area of yellow (indicative of velocities around $0.7-0.9 U/U_\infty$) along the trailing edge. These observations suggest that the higher pitching frequency is causing more significant disturbances in the flow, extending beyond the static boundaries of the wake.

Additionally, although not within the field of view, it is expected that velocities outside of the wake are higher due to the reduced space between the wake and the walls. While precise quantification of these velocities is challenging based on the images alone, the broader wake boundaries suggest a more substantial disruption of the flow caused by the higher frequency pitching.

Moreover, the boundaries of the wake in this case appear to be more spread out and less defined compared to the other cases. This indicates a higher degree of turbulence and mixing within the wake region, likely influenced by the increased pitching frequency. Overall, these findings underscore the significant impact of higher frequency pitching on altering the flow dynamics around the airfoil, leading to broader wake boundaries and more extensive disruptions in the flow field. Such insights are crucial for understanding the complex aerodynamic behaviour of airfoils under dynamic conditions and have implications for the design and optimization of airfoil configurations for various applications.



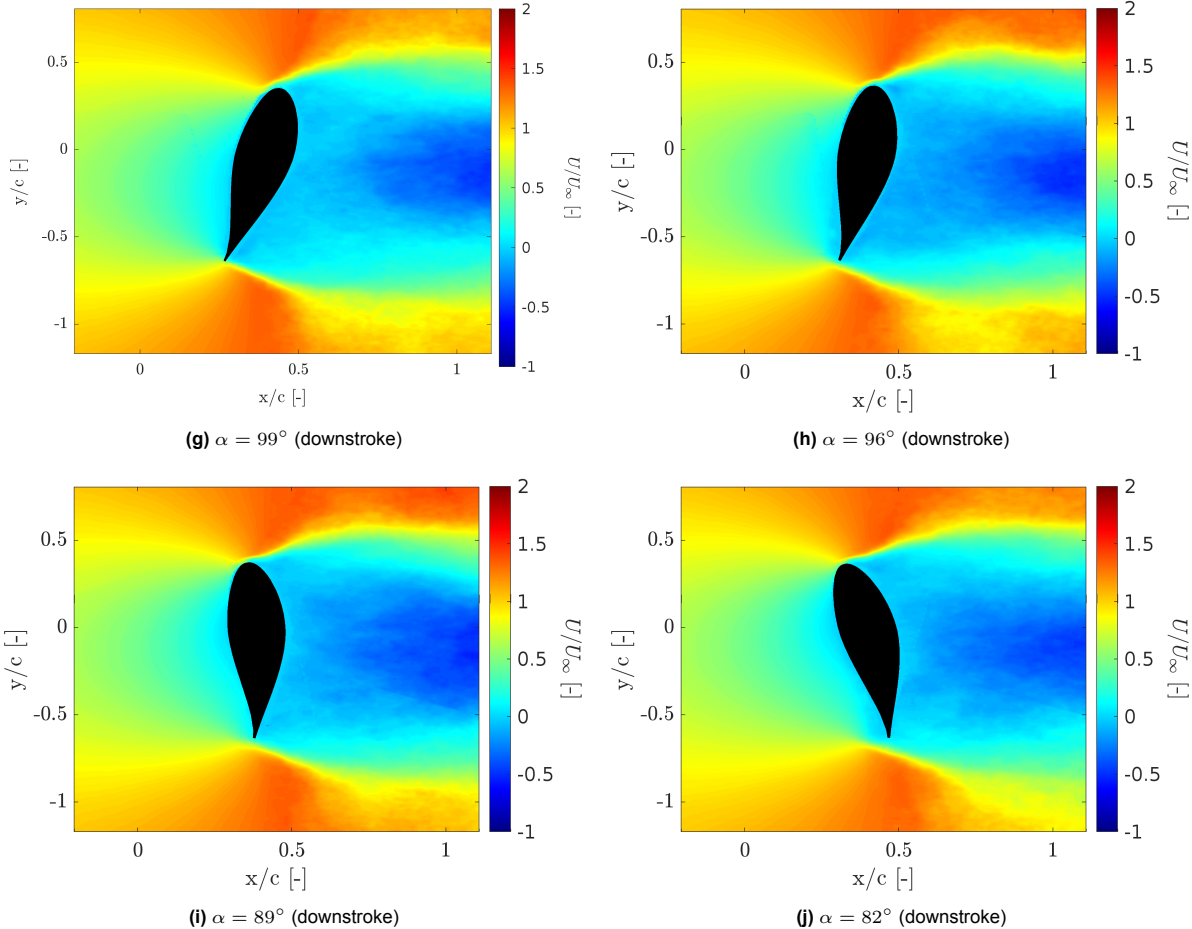


Figure 4.44: Phase locked averaged flow fields (U/U_∞) for dynamic condition with $\alpha_{mean} = 90^\circ$, $f_{pitching} = 3\text{Hz}$, and $A_{pitching} = 10^\circ$.

5

Conclusion And Recommendations

The research presented aimed to explore the behaviour of dynamic stalls on airfoils under dynamic in-flow conditions. This behaviour is typically observed in stationary airfoils experiencing unsteady deep stall conditions. The study compared several dynamic stall cases with static conditions and drew various conclusions, as well as identified steps for future work. This chapter will present both the conclusions and the proposed future steps.

5.1. Conclusion

In the conducted research, wind tunnel experiments were carried out on a NACA643418 airfoil in a low-speed, low-turbulence wind tunnel at TU Delft. The focus of these experiments was on deep stall and dynamic deep stall phenomena.

The initiation of the experiments involved the establishment of a test matrix based on existing literature to ensure the comparability of the obtained data. Mean angles of 40, 50, and 90 were further scrutinized in detail. The predetermined settings encompassed the measurement duration for both static and unsteady testing, as well as the configuration of the PIV cameras. Furthermore, an investigation into Reynolds numbers was conducted during the initial testing phases to ascertain the most appropriate Reynolds number for the majority of the experiments, ultimately establishing $Re = 250k$.

The next step involved measuring the accuracy of the actuator to assess the pitching performance. The results indicated a high level of precision, with the maximum time error for the studied cases not exceeding 0.20% and an average of 0.16% when compared to a perfect sine wave.

Subsequently, the raw data was corrected for wind tunnel effects using both the Allen Method, for low angles of attack to 20°, and the Maskell Method, for angles of attack above 20°. These corrections revealed that increased blockage led to a greater pitch angle of the airfoil, particularly in the 40° to 130° regime, compared to lower angles or angles of 180°. This, in turn, resulted in higher corrections to the coefficients of lift (C_l) and drag (C_d). The tunnel corrections also illustrated trends in the averaged plots of pressure coefficients (C_p) for different angles. Furthermore, an examination of the stall behaviour of the airfoil showed a laminar separation bubble in combination with trailing edge separation as the cause for the transition from linear to turbulent flow in the 10° to 20° angle of attack range.

Following the static pressure measurements, static PIV images were created to establish a strong foundation for comparing the results with the dynamic PIV images. These images unveiled a small separation at the trailing edge at an angle of attack (α) of 10°. Furthermore, the averaged images exhibited a clear anticipated trend, indicating that the wake would expand as the angle of attack increased. Additionally, it was noted that the airflow in front of the airfoil was more significantly influenced by the airfoil at higher angles of attack compared to lower angles. The instantaneous time series PIV images at 40, 50, and 90° displayed unpredictable behaviour in the wake of the airfoil during deep stall. Although the wake configurations were highly erratic and distinct across the images, they bore a clear resemblance to the averaged images. The instantaneous vorticity PIV images revealed the presence of large vortex-like structures at 40°, 50°, and 90°. The occurrence of positively and negatively oriented vortices varied depending on the angle of attack. At a 90° angle of attack, the presence of von Karman-like sheets was observed. However, due to the shedding frequency being equal to or larger

than the capturing frequency, individual structures could not be discerned as time progressed.

Subsequently, proceed to the dynamic pressure measurements. Initially, we determined the number of pitching cycles required to achieve a reasonably converged mean. Through testing, it was determined that 150 cycles were necessary. The dynamic response values for the suction and pressure sides were calculated and found to be significantly similar. These values were then used to modify the raw incoming pressure signal, reconstructing the signal as it should have been experienced by the airfoil in theory. The FFT plots of the raw incoming and corrected signals illustrated the presence of the pitching frequency and its harmonics, as well as the shedding frequency. As the frequency and amplitude were increased, it was observed that for the 40° and 50° cases, the shedding frequency became less dominant, displaying more side lobes, while the pitching frequency became more prominent. However, this effect of the side lobes and the reduction in the dominance of the shedding frequency peak was not as pronounced in the 90° cases, where the shedding frequency continued to play a larger role as the frequency and amplitude increased. It was noted during these measurements that the sin-corrected Strouhal numbers ranged from 0.16 to 0.19, consistent with the estimates from existing literature.

The hysteresis plots for $C_{d_{pressure}}$ and C_l revealed that during the downstroke of the airfoil, the values tended to be higher compared to the upstroke values. As the frequency and amplitude increased, the difference between the upstroke and downstroke values also increased, underscoring the significant influence of flow frequency and amplitude on the airfoil's aerodynamic performance at specific angles. Notably, at 90° angles of attack, the coefficients exhibited linear behaviour even under dynamic pitching conditions, hovering around their static values. This suggests that the airfoil experiences less variation in forces when pitching at this angle, indicating that the flow is less affected by pitching and is primarily influenced by shedding frequency rather than pitching motion.

Finally, the phase-averaged PIV images for the dynamic cases were presented, revealing conclusions consistent with the pressure data. On average, during the downstroke, there appeared to be less reverse flow compared to the upstroke for the 40° and 50° cases. This difference could be a contributing factor to the lower lift performance observed during the upstroke, as well as the presence of a larger wake boundary during most instances of the downstroke.

In summary, during deep stall conditions with an angle of attack exceeding 25°, the airflow around the aircraft is highly disrupted, leading to turbulent airflow over the airfoil surface and resulting in a significant loss of lift and increased drag. In deep stall conditions, the forces and moments acting on the airfoil surface exhibit a higher drag coefficient and a parabolic-shaped lift coefficient curve due to intense airflow separation. The pitching frequency and amplitude are crucial factors influencing the differences between upstroke and downstroke values of drag and lift coefficients at angles of attack up to 90°, where shedding frequency plays a crucial role. Higher pitching frequencies and amplitudes worsen these differences due to increased flow separation and unsteady aerodynamic effects. Vortex shedding patterns during dynamic pitching vary with different frequencies and amplitudes at the same mean angle of attack. At an angle of attack of around 90°, vortex shedding becomes the most pronounced phenomenon, even during dynamic pitching.

5.2. Recommendations and Future Work

Understanding aerodynamic phenomena is crucial for various industries, from aerospace engineering to wind energy production. However, in recent research endeavours, certain limitations have hindered the comprehensive analysis of critical aspects such as shedding frequencies, vortex structures, and small drift inaccuracies. This thesis proposes several future directions and recommendations aimed at addressing these limitations and advancing the understanding of aerodynamics.

Firstly, the static pressure measurements employed in the research lacked the necessary acquisition rate to capture shedding frequencies adequately. To rectify this, future work should involve utilizing a higher acquisition rate for static pressure measurements. By recording each measurement separately rather than relying solely on time-averaged values, researchers can fully capture shedding frequencies and delve deeper into their characteristics. This enhanced data collection approach will enable a more detailed study of shedding phenomena and its implications on aerodynamic performance.

Similarly, Particle Image Velocimetry (PIV) plays a crucial role in visualizing flow fields and understanding phenomena like shedding. However, the current research suffered from limitations in PIV image capture, particularly at higher wind speeds. Future studies should either decrease wind speeds during image acquisition or employ cameras with higher capturing rates to ensure the comprehensive

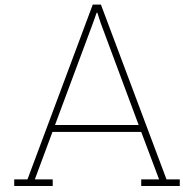
observation of shedding phenomena. This adjustment will enhance the accuracy and completeness of PIV data, facilitating a more thorough analysis of flow dynamics.

Moreover, the thesis highlighted the importance of improving phase-locking PIV setups to account for small drift inaccuracies in actuators. To address this issue, future research should focus on developing better phase-locking PIV setups that can accurately compensate for such drift. By ensuring precise synchronization between actuation and image capture, researchers can generate phase-locked PIV images that faithfully represent the flow field dynamics, thereby enhancing the reliability of aerodynamic analysis.

Expanding the scope of research beyond a single airfoil type is another crucial recommendation. Investigating a broader range of airfoil designs will enable researchers to identify universal trends and characteristics among different airfoils. This comparative analysis is essential for advancing our understanding of aerodynamic principles and developing more efficient and versatile designs across various applications.

Additionally, the thesis suggests extending the experimental setup to include a four-camera configuration for a larger instantaneous field of view. By capturing a wider area of the flow field, researchers can more clearly visualize and analyze longer vortex structures as they evolve over time. This expanded field of view will provide valuable insights into the dynamics and behaviour of vortex structures, contributing to a deeper understanding of aerodynamic phenomena.

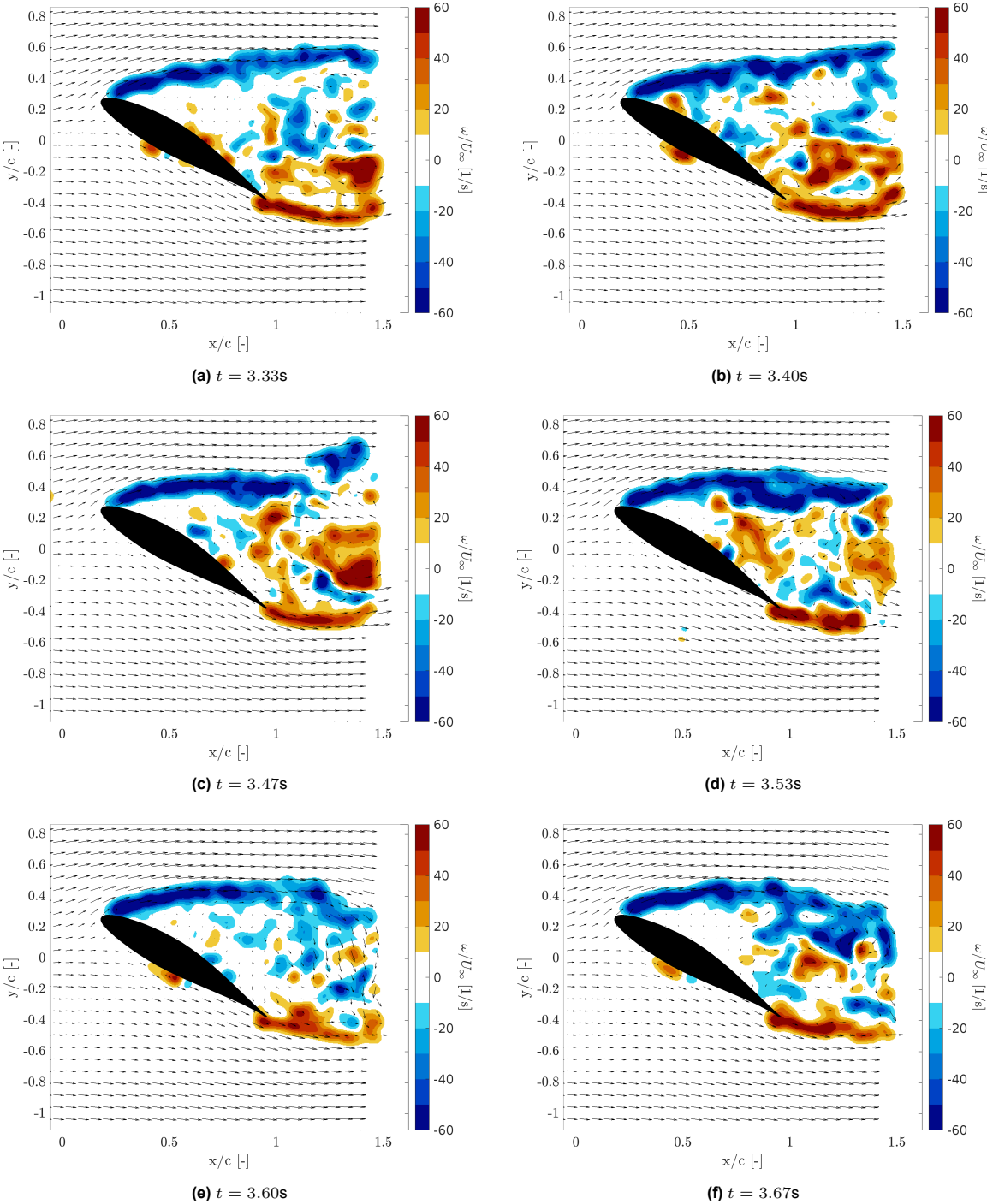
In conclusion, the future work and recommendations outlined in this thesis aim to address key limitations in current aerodynamic research and enhance our understanding of complex flow phenomena. By employing higher acquisition rates for static pressure measurements, optimizing PIV image capture, improving phase-locking PIV setups, diversifying airfoil studies, and expanding experimental setups, researchers can advance aerodynamic analysis and pave the way for innovative developments in various industries.

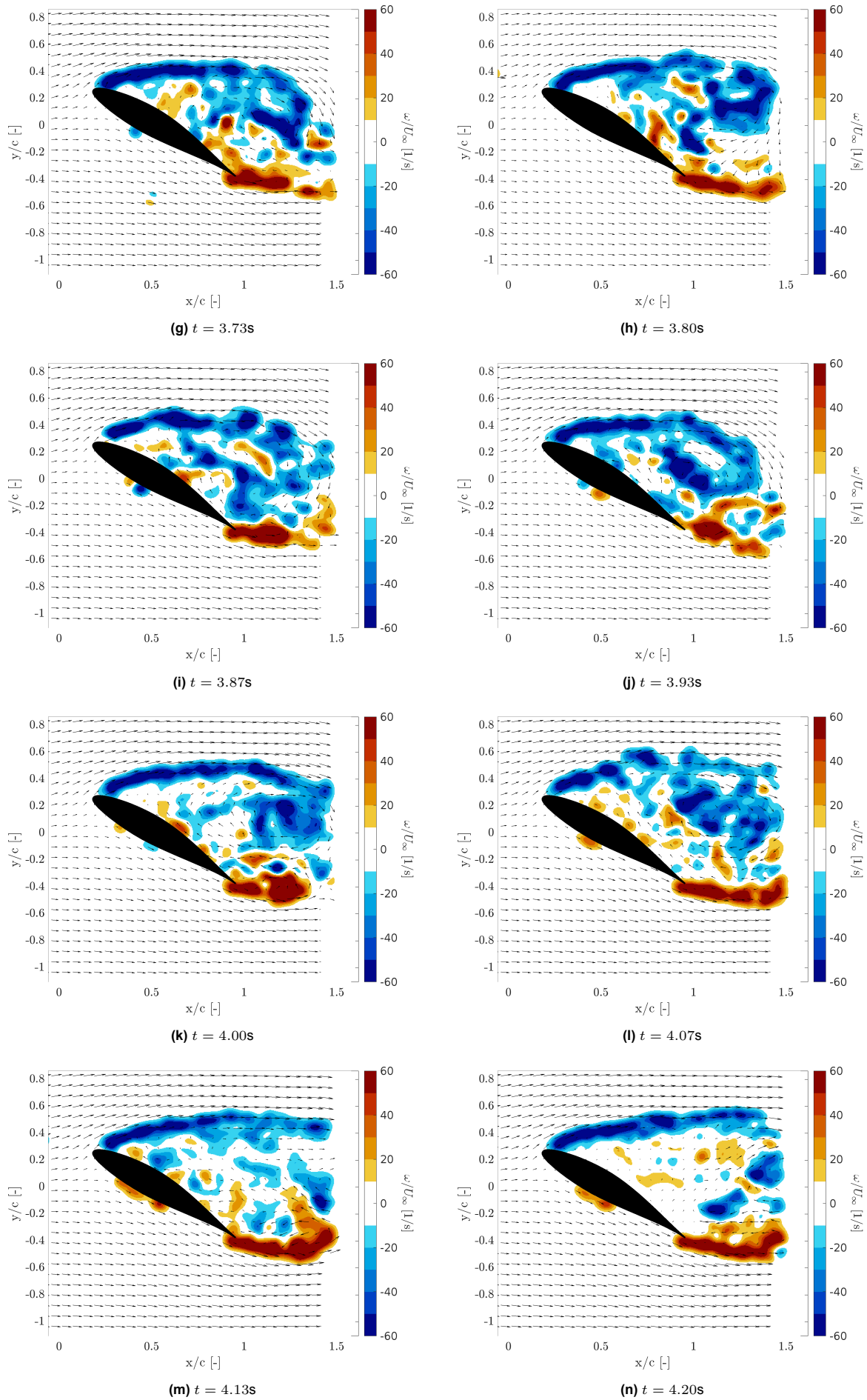


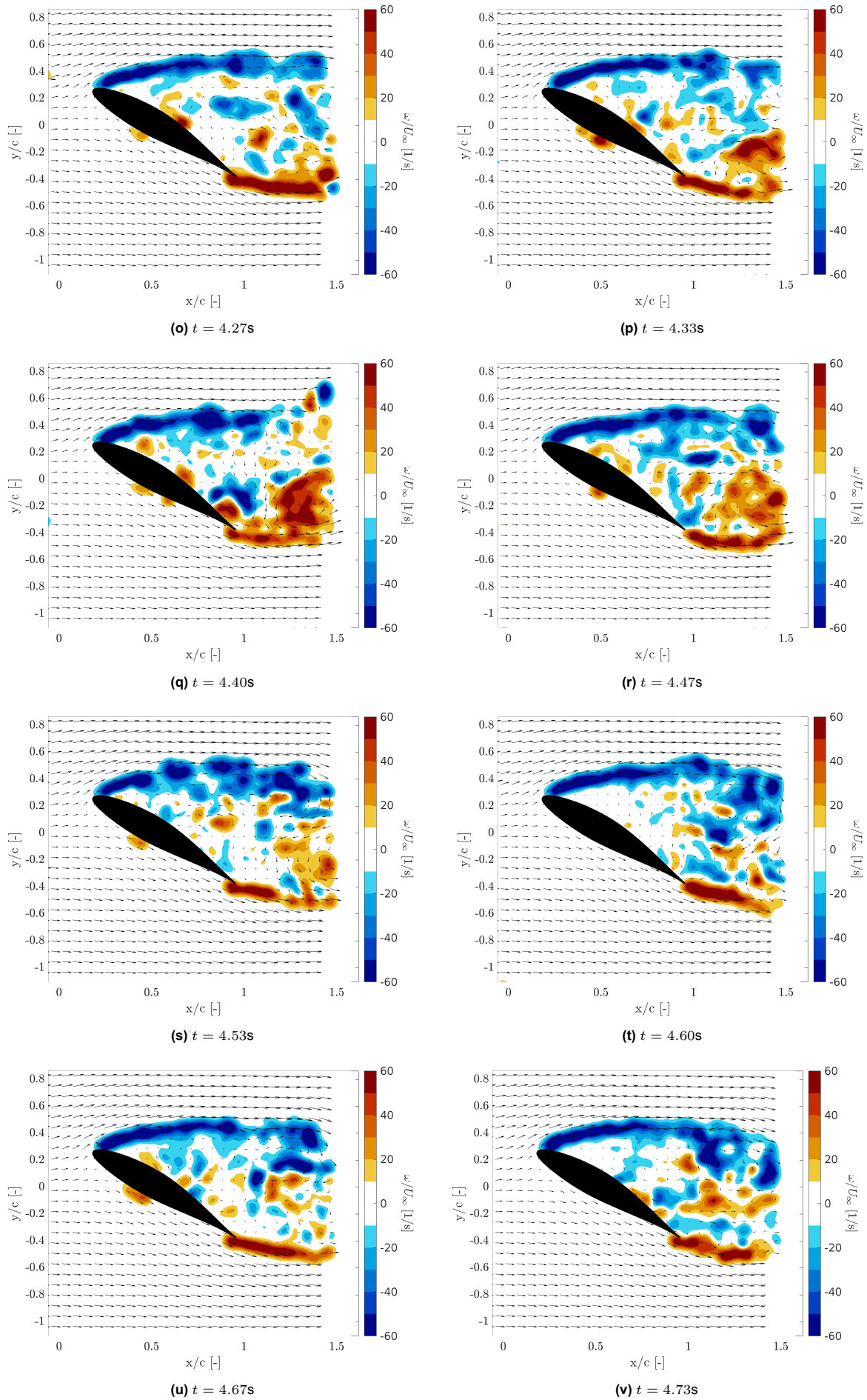
Additional Flow Field Images

This appendix includes two series of Particle Image Velocimetry (PIV) images that were not fully presented in the main sections of the report or have not been shown previously. These supplementary images provide additional insights and offer further details that enhance the understanding of the flow dynamics studied. Although they were not featured in the primary analysis, they contribute valuable supplementary information that can illuminate subtle aspects of the experimental results.

A.1. Instantaneous Vorticity Fields at $\alpha = 40^\circ$ and $Re = 250k$.







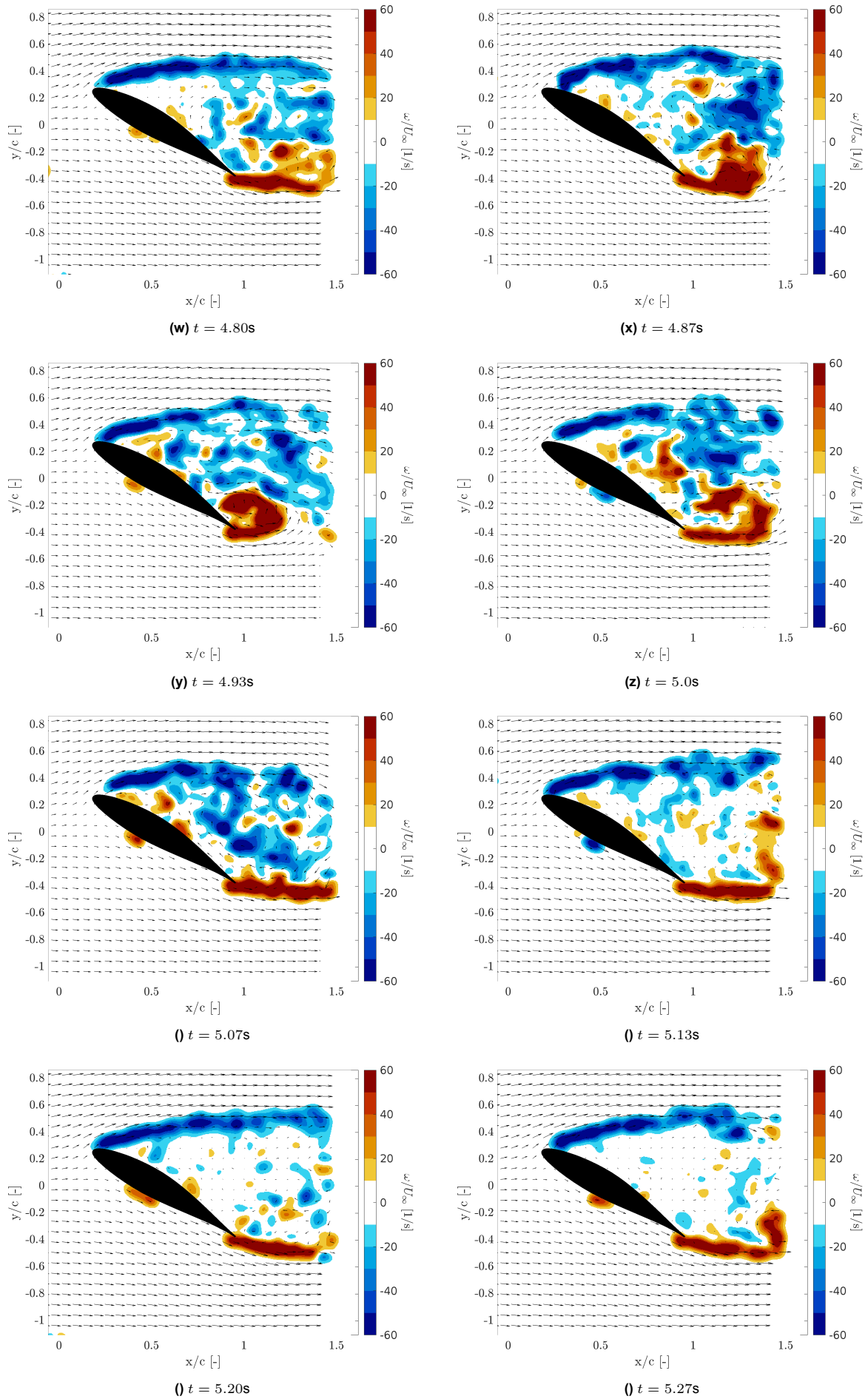
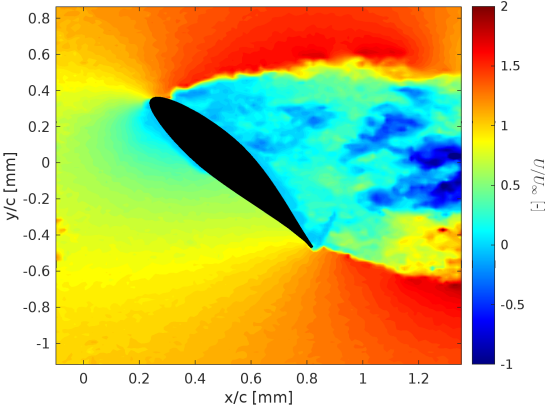


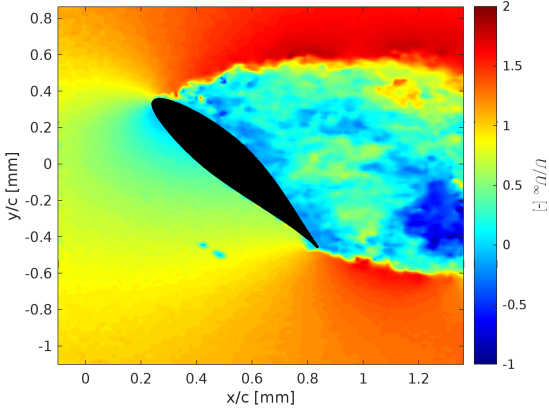
Figure A.1: Instantaneous vorticity field (ω/U_∞) with vector arrows that display the relative magnitude and direction of the flow in both x- and y-direction at $\alpha = 40^\circ$ and $Re = 250k$.

A.2. Dynamic Case One Cycle Instantaneous Flow Fields

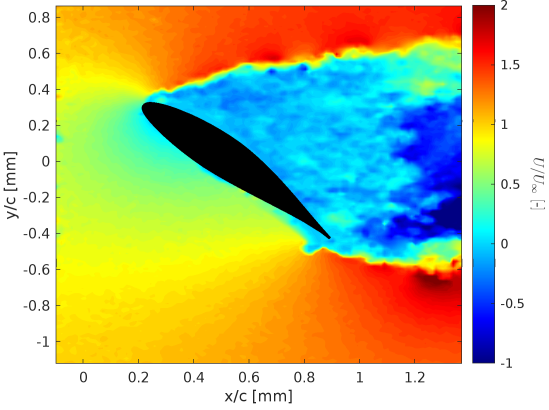
These images depict a dynamic case that is not used further in the thesis. They show a 1-cycle instantaneous flow field for a case with an $\alpha_{mean} = 40^\circ$, $f_{pitching} = 1\text{Hz}$ and $A_{pitching} = 15^\circ$.



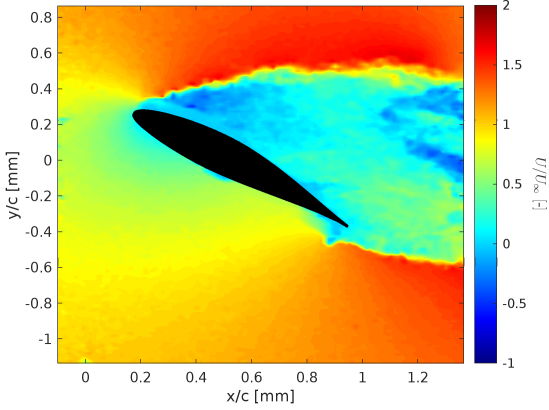
(a) 1/10



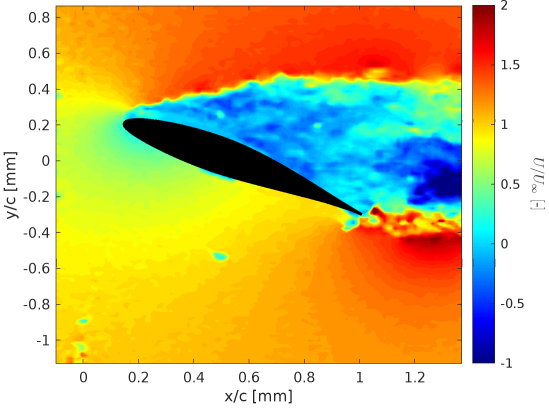
(b) 2/10



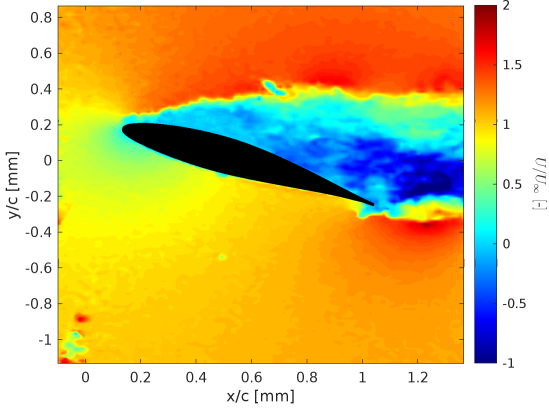
(c) 3/10



(d) 4/10



(e) 5/10



(f) 6/10

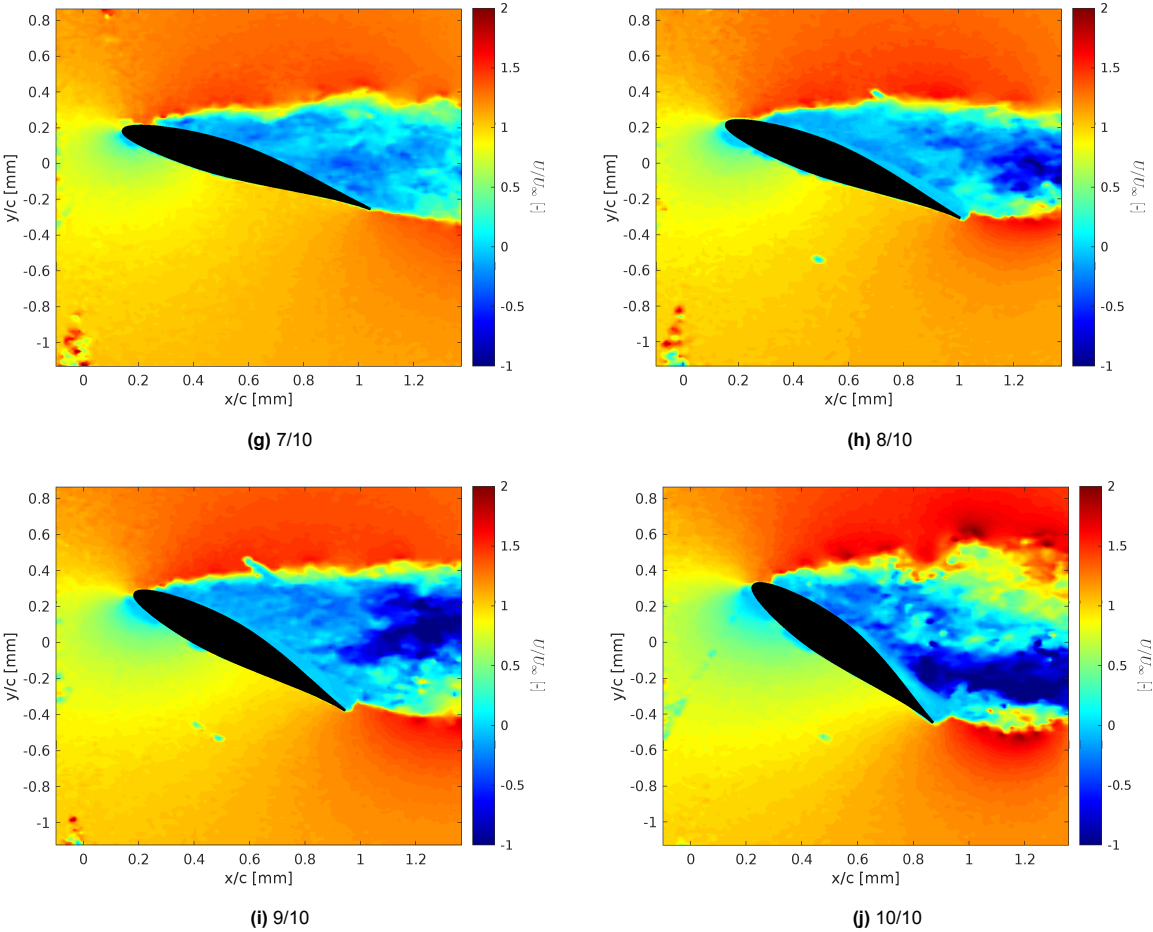


Figure A.2: Instantaneous flow field (U/U_∞) showing one full pitch cycle for the dynamic case at $\alpha_{mean} = 40^\circ$, $f_{pitching} = 1\text{Hz}$, $A_{pitching} = 15^\circ$ and $Re = 250k$.

B

Submitted Abstract Paper

This appendix includes the abstract submitted for the NAWEA Windtech Conference, which is scheduled to be held from October 30 (Wednesday) to November 1 (Friday) at the Hyatt Regency in New Brunswick, NJ. The conference is an event in the wind energy sector, bringing together experts, researchers, and industry professionals to discuss advancements and challenges in wind technology. The abstract presented aims to contribute to the ongoing dialogue and research in this field, highlighting key findings and developments relevant to the wind energy industry. The inclusion of this abstract in the appendix provides a detailed overview of the research topic, objectives, and anticipated impact, aligning with the conference's focus on innovation and practical applications in wind technology.

Experimental analysis of dynamic stall at large angles of attack

Guanqun Xu, Pepijn Slooter, Wei Yu, Andrea Sciacchitano, and Carlos Ferreira

Faculty of Aerospace Engineering, Delft University of Technology, Delft, Netherlands

corresponding email: G.Xu-1@tudelft.nl

Track 17: Rotor Aerodynamics and Aeroelasticity

Introductory Summary

The dynamic stall effect on airfoils has been extensively studied within a limited range of angles of attack (AoA). However, in wind turbine applications where the turbine may be at a standstill, larger mean AoAs ($\bar{\alpha}$) are expected, potentially leading to vortex-induced vibration (VIV). This research aims to study the dynamic stall effect of an airfoil above 25° as these angles hold significance related to turbines at standstill turbine conditions. Surface pressure measurements and Particle Image Velocimetry (PIV) measurements were performed on a NACA 643418 airfoil within a low-turbulence tunnel. Tests were conducted across a range of reduced frequencies (k) from 0.05 to 0.21, and pitch amplitudes ($\Delta\alpha$) varying from 5° to 15° , encompassing large $\bar{\alpha}$ up to 160° . Further analysis will be conducted to understand the influence of k and $\Delta\alpha$ on the hysteresis loop. By conducting the frequency analysis, the connection between the static shedding frequency and the motion frequency will be established. Furthermore, by comparing the results between pressure and PIV measurement, deeper insights will be gained into flow field characteristics, especially the influence of vortex separation on force outcomes.

Keywords: *Dynamic stall, large angles of attack, unsteady Aerodynamics, Particle Image Velocimetry, airfoil pitching*

Introduction

Stall typically occurs when the angle of attack (AoA) of the wind surpasses a specific threshold, causing the airflow not to adhere closely to the surface. In comparison to conditions of light stall, deep stall scenarios for an airfoil are found to be less sensitive to specific details of airfoil motion, airfoil geometry, Reynolds number (Re), and Mach number[1]. However, within this regime, vortex shedding plays a pivotal role in the aerodynamic processes due to substantial fluctuations in force and momentum caused by the passage of vortices along the suction side of the airfoil surface. Numerical simulations were conducted for the NACA 0012 airfoil, involving both pure-heaving and pure-pitching motions, with the maximum AoA extending up to 25° [2]. In another study[3], Particle Image Velocimetry (PIV) was employed to investigate the flow characteristics of a pitching airfoil, specifically the NACA 0012. This investigation maintained the mean AoA ($\bar{\alpha}$) at 15° and a pitching amplitude ($\Delta\alpha$) of 10° . While the study achieved high spatial resolution data on the suction side of the airfoil, some critical regions near the wake still lacked complete data. In a separate analysis[4], comparisons were made between cases with $\bar{\alpha}$ of 10° and 15° for a pitching airfoil, the NACA 23012, with a consistent $\Delta\alpha$ of 10° . Furthermore, in a study applying vortex method [5], a dynamic stall model was developed to investigate the effect of reduced frequency(k), $\bar{\alpha}$, etc. Although a slightly higher $\bar{\alpha}$ was involved here (20°), its results can still be verified with further experiments. In [6], airfoil DU-00-W-212 was examined, featuring a maximum $\bar{\alpha}$ of 18.4° with a $\Delta\alpha$ of 10.4° . These referenced studies are summarized in Table 1.

Table 1: Previous research on dynamic stall study

Reference	Airfoil	Method	$\bar{\alpha}[^\circ]$	$\Delta\alpha[^\circ]$	$k[-]$	Focus
[2]	NACA0012	Numerical	10	15	0.05, 0.1, 0.2	Comparison between pitching and heaving motions
[3]	NACA0012	Experiment	15	10	0.075	Flow field on the suction side of the airfoil
[4]	NACA 23012	Numerical	10,15	10	0.1	Assess numerical models with experiment data
[5]	NACA 0012	Numerical	15,20	10	0.15-0.5	Use vortex method to investigate the effects of k , $\bar{\alpha}$, etc.
[6]	DU-00-W-212	Both	14,18.4	10.5,10.4	0.0228, 0.0711	Verify with existing dynamic stall models

In all, few studies have given insight into very deep stall conditions ($\bar{\alpha}$ larger than 25°). Yet, this region holds significant importance for wind turbines, as they regularly encounter diverse kinematics that induce substantial fluctuations in AoA, which may lead to strong vortex-induced vibrations (VIV). Therefore, there is a pressing need of research in this critical domain to better understand the aerodynamics and loads experienced by wind turbine blades in such conditions.

Methods

In this study, the main objective is to investigate the effect of reduced frequency and pitching amplitude on the dynamic stall behaviour at very large angles of attack, with a focus on wake

vortex shedding and aerodynamic force. The experimental campaign was conducted in the Low-Speed Low Turbulence Tunnel at the Delft University of Technology. The octagonal test section is of 1.80 m wide, 1.25 m high, and 2.60 m long. This wind tunnel is closed-circuit and the nominal turbulence intensity varies from 0.015% at 20 m/s to 0.07% at 75 m/s. Airfoil NACA643418 was used in the campaign. The wing spans the entire vertical dimension of the test section (1.8 m) and has a chord of 250 mm. A total of 49 pressure sensors were used to measure the static pressure over the airfoil surface.

The setup of the PIV measurement is shown in Figure 1. The flow inside the tunnel was seeded with water-glycol droplets of $1 \mu\text{m}$ median diameter produced by a SAFEX smoke generator. The flow was illuminated by two Quantel Evergreen Nd:YAG lasers (200 mJ pulse energy, maximum 15 Hz repetition rate, 532 nm wavelength). They were shooting on the two sides of the test section for maximum illumination. Flow field imaging was conducted using two LaVision's Imager sCMOS cameras (2560×2160 pixel, 16 bit, $6.5 \times 6.5 \mu\text{m}$ pixel size) with 50 mm Nikon lenses (f-stop 8). The digital resolution of 4.94 pixels/mm. The cameras were controlled by a LaVision programmable timing unit PTU X, where precise pulses are triggered and synchronized for cameras and lasers.

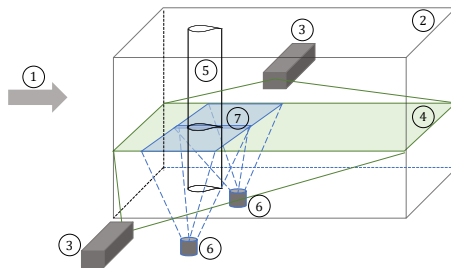


Table 2. Test matrix.

$\bar{\alpha}$ [°]	f [Hz]	k [-]	$\Delta\alpha$ [°]
	1	0.05	5
5, 10, 15, 40, 50,	2	0.10	5, 10, 15
90, 130, 160	3	0.15	5, 10, 15
	4	0.21	5

Figure 1. Schematic plot of the PIV setup. The components of the measurement are: ①: incoming wind ②: test section ③: lasers ④: illumination plane ⑤: airfoil model ⑥: cameras ⑦: field of view.

In order to minimize the Re effect, a Re swept test on the static airfoil was carried out in the first step. The Re was varied from $80k$ to $1000k$. The C_l polar from 0° to 180° for the tested Re s are shown in Figure 2. Note that the result is the raw data. It is distinct that the result at $80k$ deviates the most from the rest at all the measured AoAs. When $Re = 150k$, a visible difference can be seen from 40° to 60° and from 120° to 140° . As the primary AoAs of this investigation are above the normal stall region, the result at $250k$ is considered to be a good condition for the unsteady pressure measurement without having significant Re effects. With the acquired polar, the unsteady pressure and PIV measurement are shown in Table 2.

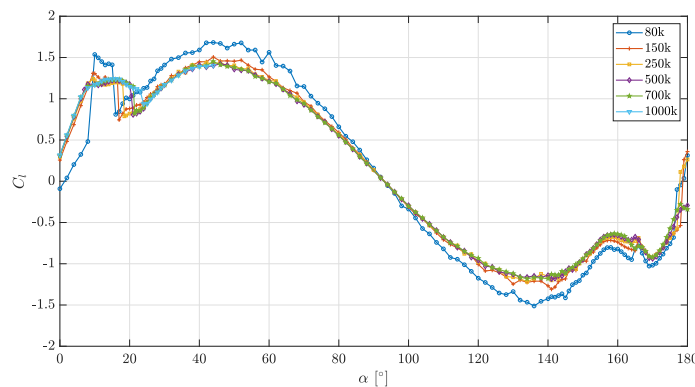


Figure 2. Steady polar at different Re s.

Results and Conclusions

The pressure measurements were subjected to two kinds of correction. Firstly, due to the existence of the tube distance from the airfoil surface to the pressure transducer, a certain time delay and amplitude attenuation can be expected. One way to correct the result is via a transfer function. Using the transfer function calculation tool [7], the data can be corrected in the frequency domain based on the tube lengths, tube diameters, etc. Secondly, due to the large AoA, the effect of

the presence of the test section wall cannot be neglected. A widely used blockage correction for large AoAs is the Maskell method [8], which has been applied in this campaign. The corrected lift coefficient C_l for $\bar{\alpha} = 40^\circ$ and 160° , $f = 3$ Hz, $\Delta\alpha = 10^\circ$ are shown in Figure 3. At $\bar{\alpha} = 40^\circ$, a larger standard deviation is shown compared to $\bar{\alpha} = 160^\circ$. This is mainly due to the higher angle relative to the wind direction, which creates a larger flow separation. At $\bar{\alpha} = 160^\circ$, larger standard deviations can be seen in the upstroke motion compared to the downstroke motion. This indicates that the positive pitch rate induces a more unsteady flow separation process, which will also be validated with PIV results.

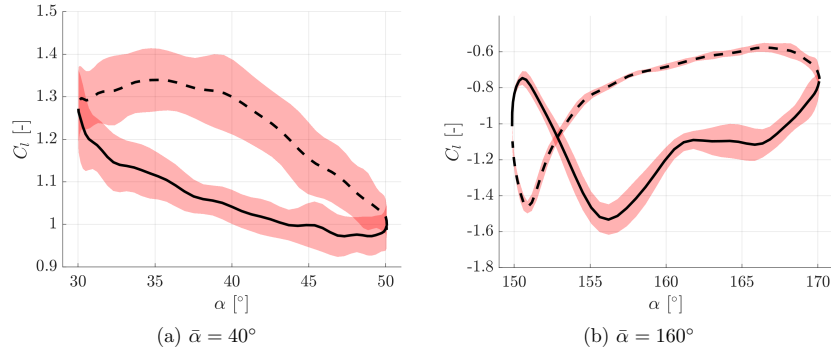


Figure 3. Lift hysteresis with corrected pressure data for $\bar{\alpha} = 40^\circ$ and 160° , both have $f = 3$ Hz and $\Delta\alpha = 10^\circ$. The black line represents the mean value, with the solid line representing the upstroke motion and the dashed line representing the downstroke motion. The red-shaded area represents the standard deviation.

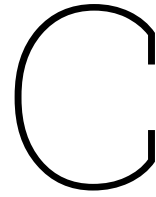
The variation in lift hysteresis between these two cases presents the complexity of the flow. Detailed research outputs on the following will be presented at the conference:

1. the influence of $\bar{\alpha}$, $\Delta\alpha$, and k on the hysteresis loop
2. frequency analysis on the unsteady pressure data, and investigate the relation of the dominant frequency concerning the static shedding frequency and the motion frequency
3. phase-averaged results from PIV, comparing vortex structures and flow unsteadiness

In conclusion, by solving the above-mentioned points, a deeper insight can be gained into the relation between unsteady flow dynamics and structural motion in the context of airfoils at high angles of attack, which will also lay the groundwork for fundamental insights into VIV phenomena relevant to wind turbine applications.

References

- [1] W J McCroskey. The Phenomenon of Dynamic Stall. *National Aeronautics and Space Administration*.
- [2] Hamid Reza Karbasian, Javad Abolfazli Esfahani, Aliyu Musa Aliyu, and Kyung Chun Kim. Numerical analysis of wind turbines blade in deep dynamic stall. *Renewable Energy*, 197:1094–1105, 9 2022.
- [3] M Raffel, J Kompenhans, and P Wernert. Investigation of the unsteady flow velocity field above an airfoil pitching deep dynamic stall conditions. Technical report, 1995.
- [4] A Zanotti, R Nilifard, G Gibertini, A Guardone, and G Quaranta. Assessment of 2D/3D numerical modeling for deep dynamic stall experiments. *Journal of Fluids and Structures*, 2014.
- [5] M H Akbari and S J Price. Simulation of dynamic stall for a NACA 0012 airfoil using a vortex method. *Journal of Fluids and Structures*, 17:855–874, 2003.
- [6] Martijn Steven Jorissen. Dynamic stall models applied to airfoils in deep stall. Technical report, TU Delft, 2023.
- [7] Sébastien Paris Jorge Caetano Alves, Sandy Tirtrey. A software tool to characterize the dynamic response of a pressure measurement system. *von Karman Institute for Fluid Dynamics*, 2005.
- [8] EC Maskell. A theory of the blockage effects on bluff bodies and stalled wings in a closed wind tunnel. Technical report, Aeronautical Research Council London (United Kingdom), 1963.



AI Assisted Literature Study Journal

The landscape of scientific inquiry has undergone a transformative evolution with the integration of artificial intelligence (AI) tools, particularly within the dynamic field of aerodynamics. Futurepedia, a repository boasting a diverse array of AI tools, stands out as a catalyst, ushering in a new era of efficiency and depth in literature studies.

AI-Fueled Exploration

Within Futurepedia's comprehensive toolset, ChatGPT assumes a pivotal role as a versatile language model. Beyond its capabilities in text generation, ChatGPT serves as a proficient Paper Categorization expert, enhancing the organization of literature papers. This freemium tool adeptly dissects textual inputs, identifies key themes, and generates relevant questions, thereby facilitating a streamlined and nuanced understanding of academic content.

Another noteworthy inclusion is Consensus, an invaluable paper finder within the Futurepedia ecosystem. Functioning as a research question generator, Consensus aids in curating a well-defined list of literature by aligning with supervisor recommendations and pulling papers from diverse sources, including those recommended by TU Delft courses.

Exclusive Access and Paper Management

Lean Library, an exclusive resource for TU Delft students, adds substantial value by addressing access limitations imposed by conventional search engines. Its utility is particularly pronounced in the academic realm, where staying abreast of the latest research is imperative.

Efficient paper management is facilitated through the deployment of Cite Petal and Lumina, both freemium tools. Cite Petal excels in extracting analogous information from uploaded papers, promoting a rapid succession of insights. Lumina, on the other hand, proves to be a potent assistant in engaging with PDFs, offering a convenient platform for information extraction and expeditious literature reviews.

AI in the Graphical Domain

Bing Image Creator and Fotor extend the influence of AI into the graphical domain, introducing innovative solutions to enhance visual representation in aerodynamic literature studies. The former, a freemium tool, simplifies graphic design by generating unique, customizable images through advanced algorithms. This could be images to explain certain phenomena, create non copy right specific front covers and remove unnecessary details in real life pictures.

Enhanced Comparative Analysis:

Research Rabbit, a freemium AI tool, introduces a layer of sophistication to the comparative analysis of relevant papers. By creating a spiderweb of cross-references between selected papers, Research Rabbit unveils clusters of references, shedding light on the interconnectedness and influence of specific works within the chosen literature.

Conclusion

In the confluence of academic research and artificial intelligence, Futurepedia's comprehensive AI toolset serves as an indispensable guiding compass through the intricacies of aerodynamic literature studies. The collaborative synergy between human intellect and AI promises a future where the boundaries of knowledge are continually expanded. Nevertheless, amidst the excitement of AI-driven research, a note of caution resonates—the need for a meticulous review of AI-generated answers. Even though these responses may seem correct, the inherent nature of AI can inadvertently produce errors, underscoring the importance of ensuring accuracy and reliability in scientific investigations, all without incurring unnecessary costs.

Personal Opinions

In my view, there are a couple of significant challenges in applying AI to literature studies. Firstly, to consistently obtain accurate answers from AI tools, users need some experience and understanding of how these tools operate. Small omissions in the input prompt can lead to seemingly correct but ultimately incomplete results, with users unaware of the underlying gaps.

The second challenge builds on the first. Due to uncertainty about whether AI tools capture the full context, users must always verify the generated answers. Even with simple rephrase prompts, important nuances to the user may not be equally crucial to the algorithm. In the domains of mathematics and physics, AI tools often struggle, lacking the ability to comprehend mathematical intricacies and interpret physics in theoretical contexts.

Lastly, relying on AI could potentially diminish the creative process of connecting theory, literature, and real-life physics. As AI takes on more tasks, there's a risk of people becoming complacent in problem-solving, potentially hindering their ability to actively engage in the creative synthesis of ideas.

Proposed Workflow AI Assisted Literature Study

On the next page a proposed workflow is given that I have created based on my own doings and findings.

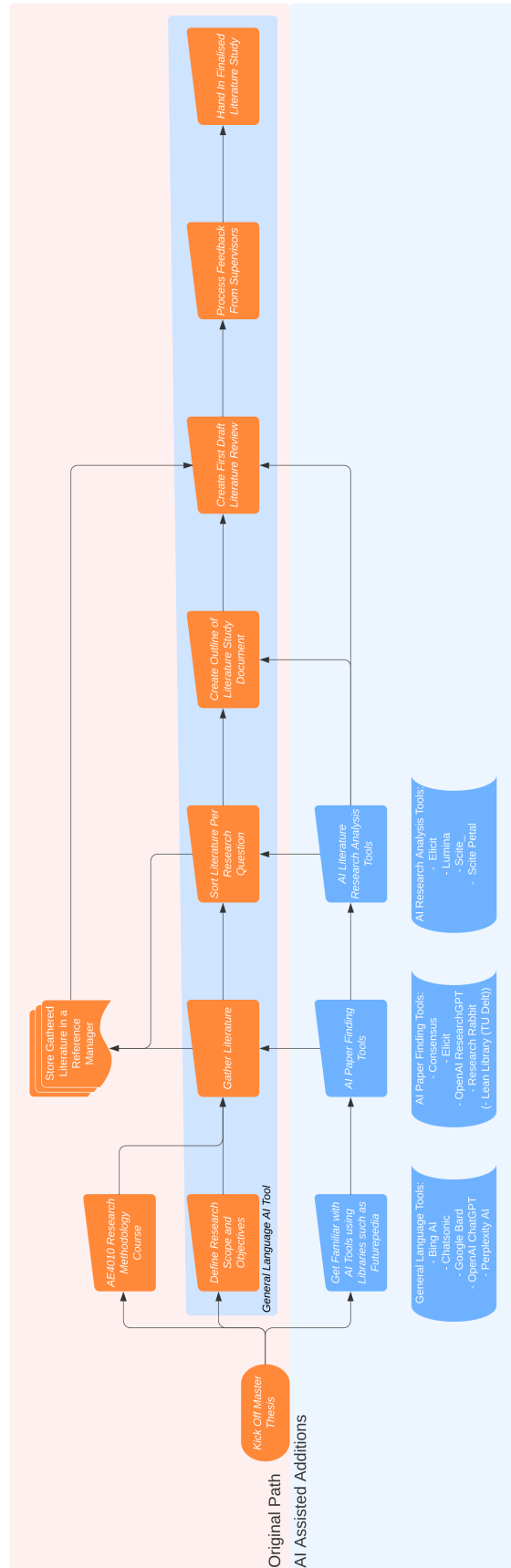


Figure C.1: Proposed AI assisted workflow for literature studies.

Bibliography

- Adema, Niels, Menno Kloosterman, and Gerard Schepers (May 2020). "Development of a second-order dynamic stall model". English. In: *Wind Energy Science* 5.2. Publisher: Copernicus GmbH, pp. 577–590. ISSN: 2366-7443. DOI: 10.5194/wes-5-577-2020. URL: <https://wes.copernicus.org/articles/5/577/2020/> (visited on 10/30/2023).
- Adrian, Ronald (June 1984). "Scattering particle characteristics and their effect on pulsed laser measurements of fluid flow: Speckle velocimetry vs. particle image velocimetry". In: *Applied optics* 23.11, pp. 1690–1. DOI: 10.1364/AO.23.001690.
- Anderson, J.D. (2017). *Fundamentals of Aerodynamics*. McGraw-Hill series in aeronautical and aerospace engineering. McGraw-Hill Education. ISBN: 978-1-259-25134-4. URL: https://books.google.nl/books?id=_7VLjwEACAAJ.
- Arunvinthan, S. and S. Nadaraja pillai (Nov. 2019). "Aerodynamic characteristics of unsymmetrical aerofoil at various turbulence intensities". In: *Chinese Journal of Aeronautics* 32.11, pp. 2395–2407. ISSN: 1000-9361. DOI: 10.1016/j.cja.2019.05.014. URL: <https://www.sciencedirect.com/science/article/pii/S1000936119302481> (visited on 10/30/2023).
- Barlow, Jewel B., William H. Rae, and Alan Pope (1999). *Low-speed wind tunnel testing*. eng. 3rd ed. OCLC: 39335023. New York: Wiley. ISBN: 978-0-471-55774-6.
- Bather, Jagdeep and Seongkyu Lee (Dec. 2022). "Numerical investigation of a pitching airfoil undergoing dynamic stall using Delayed Detached Eddy Simulations". In: *Computers & Fluids* 249, p. 105691. ISSN: 0045-7930. DOI: 10.1016/j.compfluid.2022.105691. URL: <https://www.sciencedirect.com/science/article/pii/S0045793022002845> (visited on 10/30/2023).
- Carr, L. W., K. W. Mcalister, and W. J. McCroskey (Jan. 1977). *Analysis of the development of dynamic stall based on oscillating airfoil experiments*. Tech. rep. A-6674. NTRS Author Affiliations: NASA Ames Research Center NTRS Document ID: 19770010056 NTRS Research Center: Legacy CDMS (CDMS). URL: <https://ntrs.nasa.gov/citations/19770010056> (visited on 12/13/2023).
- Corke, Thomas C. and Flint O. Thomas (Jan. 2015). "Dynamic Stall in Pitching Airfoils: Aerodynamic Damping and Compressibility Effects". In: *Annual Review of Fluid Mechanics* 47.1. Publisher: Annual Reviews, pp. 479–505. ISSN: 0066-4189. DOI: 10.1146/annurev-fluid-010814-013632. URL: <https://doi.org/10.1146/annurev-fluid-010814-013632> (visited on 10/30/2023).
- Drela, Mark and Michael B. Giles (Oct. 1987). "Viscous-inviscid analysis of transonic and low Reynolds number airfoils". In: *AIAA Journal* 25.10. Publisher: American Institute of Aeronautics and Astronautics, pp. 1347–1355. ISSN: 0001-1452. DOI: 10.2514/3.9789. URL: <https://arc.aiaa.org/doi/10.2514/3.9789> (visited on 12/20/2023).
- Elgammi, Moutaz and Tonio Sant (June 2016). "Combining Unsteady Blade Pressure Measurements and a Free-Wake Vortex Model to Investigate the Cycle-to-Cycle Variations in Wind Turbine Aerodynamic Blade Loads in Yaw". en. In: *Energies* 9.6. Publisher: MDPI AG, p. 460. ISSN: 1996-1073. DOI: 10.3390/en9060460. URL: <http://www.mdpi.com/1996-1073/9/6/460> (visited on 10/30/2023).
- EverGreen² (70-200 mJ @ 532 nm) - Quantel (2023). URL: <https://www.quantel-laser.com/en/products/item/evergreen-70-200-mj-.html> (visited on 12/05/2023).
- Ewald, B. F. R (Oct. 1998). *Wind Tunnel Wall Corrections (la Correction des effets de paroi en soufflerie)*. en. Section: Technical Reports. AGARDograph 336. URL: <https://apps.dtic.mil/sti/citations/ADA356695> (visited on 11/02/2023).
- Fage, A. and F. C. Johansen (1927). *On the flow of air behind an inclined flat plate of infinite span*. en. Technical Report. Accepted: 2014-10-21T12:03:21Z. H. M. Stationery Office. URL: <https://reports.aerade.cranfield.ac.uk/handle/1826.2/1423> (visited on 12/22/2023).
- Garner, H. C. et al. (Oct. 1966). "SUBSONIC WIND TUNNEL WALL CORRECTIONS". In: AGARDograph 109. URL: <https://www.semanticscholar.org/paper/SUBSONIC-WIND-TUNNEL-WALL-CORRECTIONS-Garner-Rogers/7022aed533fec45b632422327a40410449cc8f56> (visited on 12/22/2023).

- Geissler, W. and H. Haselmeyer (Oct. 2006). "Investigation of dynamic stall onset". In: *Aerospace Science and Technology* 10.7, pp. 590–600. ISSN: 1270-9638. DOI: 10.1016/j.ast.2006.05.001. URL: <https://www.sciencedirect.com/science/article/pii/S1270963806000642>.
- GmbH, LaVision (2023). *Cameras for PIV*. en. URL: <https://www.lavision.de/en/products/cameras/cameras-for-piv/> (visited on 12/05/2023).
- Gupta, Rohit and Phillip Ansell (Oct. 2018). "Unsteady Flow Physics of Airfoil Dynamic Stall". In: *AIAA Journal* 57, pp. 1–11. DOI: 10.2514/1.J057257.
- Gupta, Sandeep and J. Gordon Leishman (2006). "Dynamic stall modelling of the S809 aerofoil and comparison with experiments". en. In: *Wind Energy* 9.6. ISSN: 1099-1824. DOI: 10.1002/we.200. URL: <https://onlinelibrary.wiley.com/doi/abs/10.1002/we.200> (visited on 12/22/2023).
- Hackett, J. E. (Dec. 1996). "Tunnel-induced gradients and their effect on drag". In: *AIAA Journal* 34.12. Publisher: American Institute of Aeronautics and Astronautics, pp. 2575–2581. ISSN: 0001-1452. DOI: 10.2514/3.13441. URL: <https://arc.aiaa.org/doi/10.2514/3.13441> (visited on 12/22/2023).
- Holierhoek, J.G. et al. (Jan. 2013). "Comparing different dynamic stall models". In: *Wind Energy* 16.1. Publisher: John Wiley & Sons, Ltd, pp. 139–158. ISSN: 1095-4244. DOI: 10.1002/we.548. URL: <https://doi.org/10.1002/we.548> (visited on 10/30/2023).
- Huang, Bin et al. (Dec. 2021). "A combined method of CFD simulation and modified Beddoes-Leishman model to predict the dynamic stall characterizations of S809 airfoil". In: *Renewable Energy* 179, pp. 1636–1649. ISSN: 0960-1481. DOI: 10.1016/j.renene.2021.07.131. URL: <https://www.sciencedirect.com/science/article/pii/S0960148121011411> (visited on 11/01/2023).
- Jorge Caetano Alves Sandy Tirtey, Sébastien Paris (2005). "A software tool to characterize the dynamic response of a pressure measurement system". In: *von Karman Institute for Fluid Dynamics*.
- Leishman, J. Gordon (2006). *Principles of helicopter aerodynamics*. eng. 2nd ed. Section: xxxvii, 826 pages : illustrations ; 27 cm. Cambridge: Cambridge University Press Cambridge. ISBN: 0-521-85860-7 978-0-521-85860-1 1-107-01335-6 978-1-107-01335-3.
- Leishman, John Gordon and T. S. Beddoes (1989). "A Semi-Empirical Model for Dynamic Stall". In: *Journal of The American Helicopter Society* 34, pp. 3–17. URL: <https://api.semanticscholar.org/CorpusID:114868039>.
- Mallik, Wrik and Daniella E. Raveh (Oct. 2020). "Aerodynamic damping investigations of light dynamic stall on a pitching airfoil via modal analysis". In: *Journal of Fluids and Structures* 98, p. 103111. ISSN: 0889-9746. DOI: 10.1016/j.jfluidstructs.2020.103111. URL: <https://www.sciencedirect.com/science/article/pii/S088997461930667X> (visited on 10/30/2023).
- Maskell, E. C. (Nov. 1963). "A Theory of the Blockage Effects on Bluff Bodies and Stalled Wings in a Closed Wind Tunnel". In: URL: <https://www.semanticscholar.org/paper/A-Theory-of-the-Blockage-Effects-on-Bluff-Bodies-in-AgRONAUTIAREERHCJNU-Maskell/cc95afb3fdebb41096a57432842a909e0519fd9e> (visited on 12/22/2023).
- McCroskey, W.J. (1981). *The Phenomenon of Dynamic Stall*. Defense Technical Information Center. URL: <https://books.google.nl/books?id=I-JCAQAAIAAJ>.
- Peters, David A (1985). "Toward a Unified Lift Model for Use in Rotor Blade Stability Analyses". en. In: *Journal of the American Helicopter Society* 30.3, pp. 32–42. ISSN: 00028711. DOI: 10.4050/JAHS.30.32.
- Raffel, M., J. Kompenhans, and P. Wernert (June 1995). "Investigation of the unsteady flow velocity field above an airfoil pitching under deep dynamic stall conditions". en. In: *Experiments in Fluids* 19.2, pp. 103–111. ISSN: 1432-1114. DOI: 10.1007/BF00193856. URL: <https://doi.org/10.1007/BF00193856> (visited on 10/30/2023).
- Raffel, Markus et al. (2007). *Particle Image Velocimetry: A Practical Guide*. en. Berlin, Heidelberg: Springer. ISBN: 978-3-540-72307-3 978-3-540-72308-0. DOI: 10.1007/978-3-540-72308-0. URL: <http://link.springer.com/10.1007/978-3-540-72308-0> (visited on 12/22/2023).
- Simão Ferreira, Carlos et al. (Jan. 2009). "Visualization by PIV of dynamic stall on a vertical axis wind turbine". en. In: *Experiments in Fluids* 46.1, pp. 97–108. ISSN: 1432-1114. DOI: 10.1007/s00348-008-0543-z. URL: <https://doi.org/10.1007/s00348-008-0543-z> (visited on 12/05/2023).
- Srinivasan, G.R., J.A. Ekaterinaris, and W.J. McCroskey (Sept. 1995). "Evaluation of turbulence models for unsteady flows of an oscillating airfoil". In: *Computers & Fluids* 24.7, pp. 833–861. ISSN: 0045-7930. DOI: 10.1016/0045-7930(95)00016-6. URL: <https://www.sciencedirect.com/science/article/pii/0045793095000166>.

- Theodorsen, Theodore (June 1935). "General theory of aerodynamic instability and the mechanism of flutter". In: *Journal of the Franklin Institute* 219.6, pp. 766–767. ISSN: 0016-0032. DOI: 10.1016/S0016-0032(35)92022-1. URL: <https://www.sciencedirect.com/science/article/pii/S0016003235920221> (visited on 12/22/2023).
- Timmer, W. and R.P.J.O.M. Rooij (Jan. 2001). "Some aspects of high angle-of-attack flow on airfoils for wind turbine application". In:
- Timmer, W. A. (2021). "Wind Tunnel Wall Corrections for Two-Dimensional Testing up to Large Angles of Attack". en. In: *Handbook of Wind Energy Aerodynamics*. Ed. by Bernhard Stoevesandt et al. Cham: Springer International Publishing, pp. 1–29. ISBN: 978-3-030-05455-7. DOI: 10.1007/978-3-030-05455-7_27-1. URL: https://link.springer.com/10.1007/978-3-030-05455-7_27-1 (visited on 11/02/2023).
- Tran, C and D Petot (1980). "Semi-empirical model for the dynamic stall of airfoils in view of the application to the calculation of responses of a helicopter blade in forward flight." nl. In: *6th European Rotorcraft & Powered Lift Aircraft Forum, 1980, Part 2*, pp. 1–48. URL: https://jglobal.jst.go.jp/en/detail?JGLOBAL_ID=200902073684871152 (visited on 12/20/2023).
- Tropea, Cameron, Alexander L. Yarin, and John F. Foss, eds. (2007). *Springer Handbook of Experimental Fluid Mechanics*. en. Berlin, Heidelberg: Springer. ISBN: 978-3-540-25141-5 978-3-540-30299-5. DOI: 10.1007/978-3-540-30299-5. URL: <http://link.springer.com/10.1007/978-3-540-30299-5> (visited on 12/21/2023).
- Truong, Khiem (Sept. 1993). *Conference proceedings: A 2-D Dynamic Stall model based on a Hopf Bifurcation*.
- Yang, DanDan et al. (Mar. 2019). "Unstable flow characteristics in a pump-turbine simulated by a modified Partially-Averaged Navier-Stokes method". en. In: *Science China Technological Sciences* 62.3, pp. 406–416. ISSN: 1869-1900. DOI: 10.1007/s11431-017-9259-3. URL: <https://doi.org/10.1007/s11431-017-9259-3> (visited on 10/30/2023).
- YU, Wei et al. (Apr. 2023). *Modelling dynamic stall of an airfoil with vortex generators using a double-wake panel model with viscous-inviscid interaction*. DOI: 10.22541/au.168218042.24584653/v1.
- Zanon, Alessandro, Pietro Giannattasio, and Carlos J. Simão Ferreira (2013). "A vortex panel model for the simulation of the wake flow past a vertical axis wind turbine in dynamic stall". en. In: *Wind Energy* 16.5. _eprint: <https://onlinelibrary.wiley.com/doi/pdf/10.1002/we.1515>, pp. 661–680. ISSN: 1099-1824. DOI: 10.1002/we.1515. URL: <https://onlinelibrary.wiley.com/doi/abs/10.1002/we.1515> (visited on 12/20/2023).
- Zanotti, A. et al. (Nov. 2014). "Assessment of 2D/3D numerical modeling for deep dynamic stall experiments". In: *Journal of Fluids and Structures* 51, pp. 97–115. ISSN: 0889-9746. DOI: 10.1016/j.jfluidstructs.2014.08.004. URL: <https://www.sciencedirect.com/science/article/pii/S0889974614001819>.
- Zanotti, Alex and Giuseppe Gibertini (Sept. 2013). "Experimental investigation of the dynamic stall phenomenon on a NACA 23012 oscillating airfoil". en. In: *Proceedings of the Institution of Mechanical Engineers, Part G: Journal of Aerospace Engineering* 227.9. Publisher: IMECHE, pp. 1375–1388. ISSN: 0954-4100. DOI: 10.1177/0954410012454100. URL: <https://doi.org/10.1177/0954410012454100> (visited on 11/08/2023).
- Zhou, Tong, Earl Dowell, and Shun-shan Feng (Dec. 2019). "Computational investigation of wind tunnel wall effects on buffeting flow and lock-in for an airfoil at high angle of attack". In: *Aerospace Science and Technology* 95, p. 105492. ISSN: 1270-9638. DOI: 10.1016/j.ast.2019.105492. URL: <https://www.sciencedirect.com/science/article/pii/S1270963819313902> (visited on 11/02/2023).
- Zhu, Chengyong, Yingning Qiu, and Tongguang Wang (May 2021). "Dynamic stall of the wind turbine airfoil and blade undergoing pitch oscillations: A comparative study". In: *Energy* 222, p. 120004. ISSN: 0360-5442. DOI: 10.1016/j.energy.2021.120004. URL: <https://www.sciencedirect.com/science/article/pii/S036054422100253X> (visited on 10/30/2023).
- Zhu, Chengyong, Tongguang Wang, et al. (Jan. 2020). "Effect of Single-Row and Double-Row Passive Vortex Generators on the Deep Dynamic Stall of a Wind Turbine Airfoil". en. In: *Energies* 13.10. Number: 10 Publisher: Multidisciplinary Digital Publishing Institute, p. 2535. ISSN: 1996-1073. DOI: 10.3390/en13102535. URL: <https://www.mdpi.com/1996-1073/13/10/2535> (visited on 10/30/2023).